



Laboratoire de Physique des Interactions
Ioniques et Moléculaires (PIIM)
Université de Provence



Institut de Recherche sur la Fusion par
confinement Magnétique (IRFM)
CEA Cadarache

Thèse de doctorat de l'Université de Provence

Simulation Magnéto-Hydro-Dynamiques des Edge-Localised-Modes dans un tokamak

Présentée par

Stanislas PAMELA

Soutenue le 27 Septembre 2010 devant le jury composé de :

Pr. Howard WILSON	Professeur au Department of Physics University of York, United-Kingdom	Rapporteur
Dr. Hinrich LUTJENS	Docteur d'état, Chargé de Recherche au CNRS CPHT, Ecole Polytechnique, Palaiseau	Rapporteur
Dr. Xavier LITAUDON	Chef-Adjoint du Service de Chauffage et Confinement du Plasma, IRFM, CEA Cadarache	Président du Jury
Pr. Sadruddin BENKADDA	Professeur au Laboratoire PIIM, Directeur de Recherche CNRS, Université de Provence, Aix-Marseille I	Directeur de thèse
Dr. Guido HUYSMANS	Chercheur au Service de Chauffage et Confinement du Plasma, IRFM, CEA Cadarache	Responsable CEA
Pr. Peter BEYER	Professeur au Laboratoire PIIM Université de Provence, Aix-Marseille I	Invité
Dr. Pierre RAMET	Maître de Conférences, LABRI, INRIA Université de Bordeaux I	Invité

TABLE OF CONTENTS

1. Introduction	1
1.1 Nuclear Fusion	1
1.1.1 Fusion Energy	1
1.1.2 Energy Confinement	2
1.1.3 Inertial and Magnetic Confinement	3
1.1.4 Brief History of Tokamaks	4
1.1.5 ITER and the Future of Fusion Energy	5
1.2 Tokamak Configuration	6
1.2.1 Magnetic Configuration	6
1.2.2 X-point Geometry	8
1.2.3 Plasma-Facing Components	9
1.2.4 Heating Systems, Particle Injection	11
1.3 Magneto-Hydro-Dynamics	13
1.3.1 Ideal MHD Equations	13
1.3.2 Validity of MHD	15
1.3.3 Boundary Conditions	17
1.3.4 Conservation Laws	18
1.3.5 Non-Ideal MHD Models	19
1.4 Ideal MHD Equilibrium in Tokamaks	21
1.4.1 The Grad-Shafranov Equation	21
1.4.2 Tokamak Equilibrium	23
1.5 Turbulent Transport and MHD Instabilities	26
1.5.1 Parallel and Perpendicular Transport	26
1.5.2 Classical and Neoclassical Predictions	27
1.5.3 Turbulence	28
1.5.4 MHD Instabilities	29
1.6 Edge-Localised-Modes	32
1.6.1 The H-mode	32
1.6.2 Edge-Localised-Modes	33
1.6.3 Characterization of ELMs	34
1.6.4 Advantages and Disadvantages of ELMs	36
1.6.5 Avoiding and Controlling ELMs	36
1.7 Understanding ELM Physics	37
1.7.1 Experimental Observation	37
1.7.2 Theoretical Interpretation	38
1.7.3 Numerical Approach	41
1.7.4 Combining the Three Methods	41
1.8 Thesis Plan	42
2. The Numerical Tool: JOREK	45
2.1 Résumé du chapitre	45
2.2 Discretization	47
2.2.1 Poloidal and Toroidal Discretization	47
2.2.2 Finite Elements	49
2.2.3 The X-point Grid	54
2.2.4 Continuity at X-point	56
2.3 Time Stepping	57
2.3.1 Implicit Scheme	57
2.3.2 PastiX Solver	59

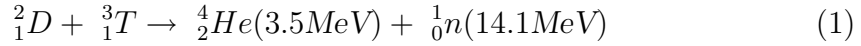
2.3.3	GMRES Convergence and Numerical Limits	59
2.4	The Physical Model	60
2.4.1	Reduced Resistive MHD	60
2.4.2	The Weak Form of Equations	62
2.4.3	Boundary Conditions	63
2.4.4	Normalization	64
2.4.5	Extensions of the Model	65
2.5	ELMs Simulations	70
2.5.1	Running Jorek	70
2.5.2	The Choice of Equilibrium and Harmonics	73
2.5.3	The Main Plasma Parameters	74
2.6	Summary	76
3.	The Influence of the Equilibrium Poloidal Flow on ELMs	78
3.1	Résumé du chapitre	78
3.2	Introduction and Motivation	79
3.2.1	Starting From an Unstable Equilibrium	79
3.2.2	Poloidal Flows at Equilibrium and During ELMs	84
3.3	Equilibrium Poloidal Flows without Parallel Velocity	86
3.3.1	Poloidal Flows in Circular Plasmas	86
3.3.2	Flows in X-point Plasmas	89
3.4	Circular Poloidal Rotation of the Pedestal Plasma	93
3.4.1	Transitions Between Equilibrium Flow States	93
3.4.2	Flows in Simulations with Parallel Velocity	95
3.5	Influence of the Flow on ELMs	101
3.5.1	Effect of the Flow on the Linear Stability of Ballooning Modes	101
3.5.2	Effect of the Flow on The Nonlinear Stability of ELMs	102
3.5.3	Summary and Conclusion	104
4.	Simulation of ELMs in the JET and MAST Tokamaks	108
4.1	Résumé du chapitre	108
4.2	Introduction and Motivations	109
4.2.1	Comparing Simulations and Experiments to Improve the Understanding of ELMs Physics	109
4.2.2	Obtain Some General Qualitative Agreement	111
4.2.3	Towards a Quantitative Validation of Simulations	112
4.3	JET Simulations	113
4.3.1	Reconstruction of the Equilibrium with JOREK	113
4.3.2	Filamentation of the Pedestal	118
4.3.3	Divertor Heat Fluxes	123
4.3.4	The ELM Size	132
4.4	MAST Simulations	137
4.4.1	Reconstruction of the MAST Equilibrium	137
4.4.2	Simulations of ELMs in MAST	137
4.4.3	Improving MAST Simulations	140
4.5	Conclusion	141
	Aknowlegements	145
	References	147
	Appendix A	150

1 Introduction

1.1 Nuclear Fusion

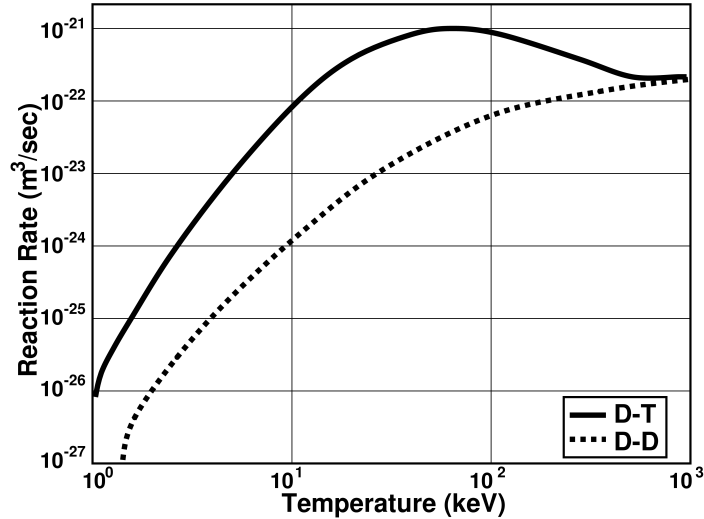
1.1.1 Fusion Energy

The goal of present research on controlled nuclear fusion is to produce energy from the fusion reaction between Deuterium (D) and Tritium (T) nuclei. These two hydrogen isotopes may combine to form a helium He atom (or alpha particle) and a neutron n . In this process, the mass outcome is smaller than the income, so that energy is produced, following Einstein's relation $E = mc^2$. The $D-T$ reaction may be expressed in the form



The resulting kinetic energy of the alpha particle and the neutron ($\sim 17.59MeV$) is much higher than the energy needed to overcome the repulsion barrier due to the electrostatic Coulomb forces ($\sim 0.01MeV$). Thus, the energy released by the fusion reaction may be used to produce new reactions. A similar process powers the stars, although different fusion reactions may be involved, including neutron fusion ($n-n$).

Figure 1: Reaction rates for $D-T$ and $D-D$ fusions.



On earth, the temperature needed to reach fusion reactions is higher than the temperature of our sun, where the strong gravitational confinement results in high density, and thus higher fusion reaction rates. At such temperatures, matter is entirely ionized - this fourth state of matter is called a

plasma. Reaching this temperature (over 100 million degrees Celcius) is not trivial, which explains why the $D-T$ reaction has been chosen : at equal temperature, its reaction rate is higher than the $D-D$ reaction rate, which can be seen from Fig.1. However, the $D-D$ reaction is of great interest considering both the large amount of Deuterium on earth, and the fact that Tritium is radioactive and expensive to produce. On longer terms, the $D-D$ reaction should be reconsidered, but for now, the main challenge is to reach the steady state fusion cycle. In other words, the immediate (short term) goal of fusion research is to create a profitable reactor that may sustain its activity on long time scales by recycling the power it produces from fusion reactions.

1.1.2 Energy Confinement

The *amplification factor* Q of a fusion reactor is defined as

$$Q = \frac{P_{fus}}{P_{inj}}, \quad (2)$$

where P_{inj} is the power injected into the reactor, and P_{fus} is the power that results from fusion reactions. If Q is equal to 1, the fusion reactions produce as much power as was needed to start the reactor, so if Q is higher than 1, the reactor is beneficial, and thus exploitable. Furthermore, as soon as $Q > 1$, the reaction starts to feed itself with enough power to partially sustain itself , so that P_{inj} may progressively be diminished. A good example of an equilibrium between P_{inj} and P_{fus} is a star like our sun, where P_{inj} is the force that results from gravity. In order for a reactor to be economically exploitable, a Q of around 50 is desirable. A Q of almost 1 has already been achieved in the Joint European Torus (JET), although for a rather short period ($\sim 1s$). The future tokamak ITER aims at $Q = 10$.

Reaching $Q \approx 1$ was a first achievement and, so to speak, a first success, but another challenge arises : to keep the reactor running for a long time with a high Q . The *confinement time* τ_E measures the rate at which energy is lost. It is written as

$$\tau_E = \frac{W}{P_{loss}}, \quad (3)$$

where W is the energy content of the plasma and P_{loss} is power lost in the process. The *Lawson Criterion* defines the conditions needed for a reactor to reach *ignition*. That is, the stage at which the fusion reactions can provide enough energy to maintain the temperature of the plasma against all power losses. This condition concerns $n\tau_E$, the product of the confinement time and the plasma density n , and it requires that $n\tau_E > 1.5 \times 10^{20} \text{m}^{-3}\text{s}$. However,

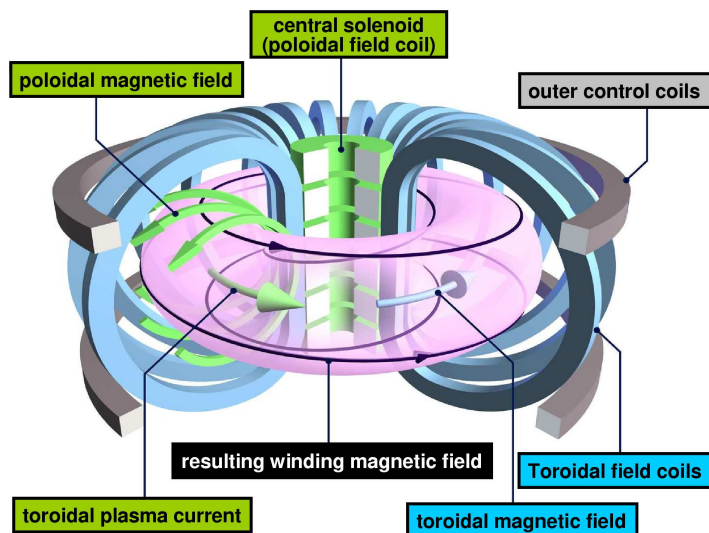
this requirement is calculated for the optimal temperature of 30keV, at which the function $n\tau_E$ finds its minimum. A more adequate requirement would also concern temperature, so that the condition $n\tau_E T > 3 \times 10^{21} \text{m}^{-3} \text{keVs}$ should be considered.

1.1.3 Inertial and Magnetic Confinement

Most ideally, the sun has a huge amount of matter to burn, and a very long confinement time, so that the Lawson Criterion is well satisfied. On human scales, there are two ways of reaching high $n\tau_E$ values. The first one consists in firing a solid $D-T$ target with a laser beam. This process, called *Inertial Confinement*, involves a high quantity of $D-T$ (high n) but a small confinement time (the target explodes in a few pico-seconds). Inertial confinement works relatively well, except that the laser repetition rate is still very low. In order for inertial confinement to be profitable, the beams should be shot between 1 to 10 times per second. At present, the most efficient laser systems have troubles operating as much as 1 time per day. Hence, the resulting efficiency of inertial confinement is poor on long time scales.

The other way of satisfying the Lawson Criterion is to focus efforts on the confinement time rather than density. This requires the $D-T$ to be brought at high temperatures, and the energy losses to be diminished. No material can survive a constant interaction with so warm plasmas. However, since all particles of a plasma are ionized, they may be confined using a magnetic field. This is called *Magnetic Confinement*. For a comparison, what confines the sun's energy is simply gravity - with magnetic confinement, the magnetic field holds the role that gravity has for the sun. The simplest way to confine a plasma using a magnetic field is by discharging a strong current in a solenoidal coil around a cylindrical vacuum vessel (the Z-Pinch) but this soon revealed not to be the best configuration, due to high losses at both ends of the open cylinder. A remedy to this problem was to close the cylinder into a torus, but the confinement remained limited due to violent plasma instabilities. The most efficient device consists of a magnetic field that winds around a toroidal vacuum chamber: a *Tokamak*. Fig.2 shows a typical Tokamak configuration, where a winding toroidal magnetic field is produced using electrical coils. The toroidal magnetic field is produced by the coils around the plasma (*toroidal field coils*), and the poloidal magnetic field is produced by the *plasma current*, which is induced by the *central solenoid*.

Figure 2: *Typical Tokamak Configuration.*



1.1.4 Brief History of Tokamaks

Research for thermonuclear fusion using tokamaks really started after the Second World War. The word *tokamak* comes from the Russian acronym of **toroidal'naya kamera s magnitnymi katushkami** (toroidal chamber with magnetic coils). This concept was developed in the 1950s by *Igor Yevgenyevich Tamm* and *Andrei Sakharov*. Some of the main features of today's tokamaks were developed then. In particular, the machines already had a vacuum chamber in the shape of a torus, and current generation by radio-frequency waves. Although the main characteristics needed for a tokamak to produce fusion reactions were quickly discovered, it took half a century and a few tens of machines to reach $Q = 1$. The principal (most active) tokamaks at present are JET (UK), Asdex-Upgrade (Germany), Tore-Supra (France) and DIII-D (USA).

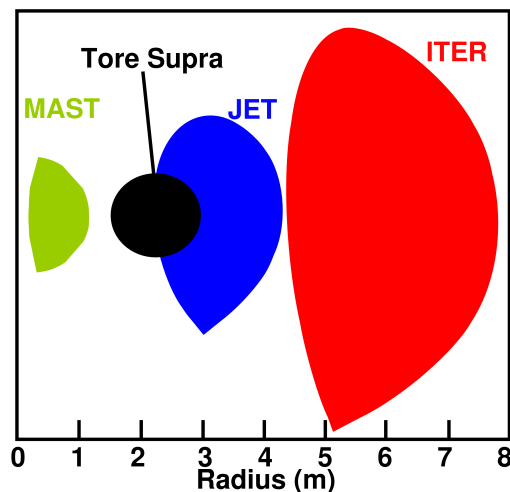
So far, there has been no competition to the tokamak except from the *stellarator*. The advantage of this device is that it does not need to generate a strong plasma current (ie. poloidal magnetic field) since all confining magnetic fields are produced by external coils. However, the design and construction of such a machine is delicate and tedious, and the development of this concept is still at least one generation behind that of tokamaks. It is still simpler and more efficient to operate with a tokamak, even if the plasma current generation remains an issue.

1.1.5 ITER and the Future of Fusion Energy

The next large-scale tokamak to be built is the ITER device (International Thermonuclear Experimental Reactor). This future machine was agreed internationally and it could significantly enhance fusion research. In particular, it should prove that exploitation of fusion energy as a resource of electrical power is conceivable and that fusion power plants could be achievable before the end of the 21st century. If it succeeds then present economical, ecological and climatic issues may take a different aspect.

The main parameter that changes with ITER is the *major radius* R and consequently the total volume of the plasma (note: the major radius is that of the torus, see Fig.4). The biggest machine today is JET, with a major radius of 3m, and ITER has been designed with a major radius of 6m. Fig.3 shows a sketch of present machines and ITER. The next step is DEMO, which should have a major radius of about 9m. If ITER reaches its goals and demonstrates that fusion may be used to produce economically exploitable energy, then DEMO will be the first prototype of what could later be a fusion reactor. The principal reason for building bigger and bigger machines is that the quantity of interest $n\tau_e$, introduced above, is strongly related to the major radius R . In fact, an empirical scaling law [1], based on experimental observations, has demonstrated that the confinement time τ_e is proportional to $R^{1.97}$.

Figure 3: *ITER Compared to Actual Tokamaks.*



1.2 Tokamak Configuration

1.2.1 Magnetic Configuration

In a magnetic field, all charged particles gyrate around a magnetic field line with a gyration radius called the *Larmor Radius* and equal to

$$\rho_L = \frac{m v_{\perp}}{qB}, \quad (4)$$

where m is the mass of the particle, q its charge and B the intensity of the magnetic field. The smaller the Larmor Radius, the better confinement of the particle. The gyration speed v_{\perp} of a particle (its speed perpendicular to the magnetic field) depends on its temperature as $v_{\perp} = \sqrt{2T/m}$. Say an ion of a Deuterium plasma with a temperature of 10keV will be well-confined if the Larmor radius is smaller than half a centimeter, then the magnetic field should be at least $4T$.

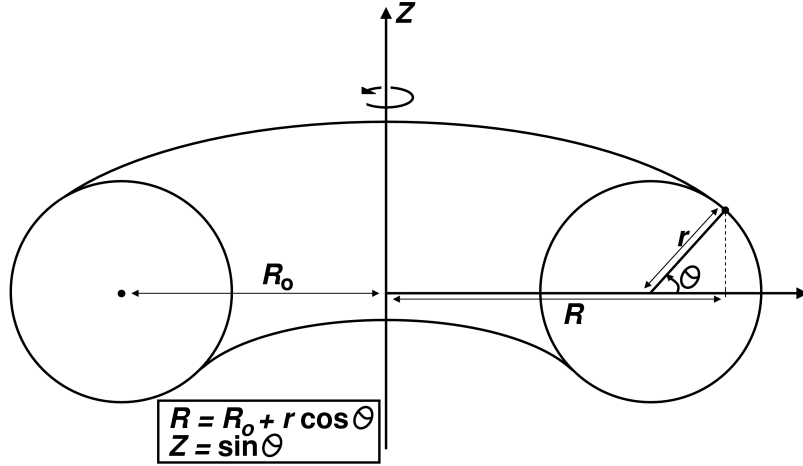
In a tokamak configuration such as shown in Fig.2, the amplitude of the toroidal magnetic field is given by Ampere's theorem, $B_T = \mu_0 I_p / 2\pi R$, where I_p is the total current running in the toroidal field coils, and R is the distance from the central axis of symmetry of the torus (see Fig.4). In a strictly toroidal magnetic field, the particles progressively drift vertically due to the $1/R$ variation of the magnetic field strength. The direction of the drift being opposite for ions and electrons, a vertical current is created and its interaction with the magnetic field provokes an horizontal drift of the particles toward the outer side of the torus.

The concept of tokamaks relies on an additional magnetic field in the poloidal direction of the torus. This poloidal magnetic field comes from an electrical plasma current I_T flowing in the toroidal direction. Typically, this plasma current is generated by a *central solenoid* (transformer core) in the middle of the torus (see Fig.2). Thus, the magnetic field lines are no longer strictly toroidal. They wind up around the torus in a fashion similar to geodesics on a toroidal manifold, as shown on Fig.2. Therefore, since particles follow the field lines, they travel between the upper half and the lower half of the torus, so that the vertical drift is compensated and confinement is improved.

The notion of *poloidal magnetic flux* ψ_p is commonly used in tokamak physics. It is defined at each point $P(a, \alpha, \beta)$ in the (r, θ, ϕ) -space, where r is the minor radius of the torus, θ the poloidal angle and ϕ the toroidal angle (see Fig.4). Namely,

$$\psi_p = \int_0^a \int_0^{2\pi} (\mathbf{B} \cdot \nabla \theta) R dr d\phi. \quad (5)$$

Figure 4: *Toroidal Coordinates.*



A simple analogy is the fluid flux through a surface. Here, the poloidal flux ψ_p is defined as the magnetic flux in the poloidal direction, averaged over the toroidal angle. In the case of toroidal axisymmetry, the poloidal flux simplifies to

$$\psi_p = 2\pi \int_0^a (\mathbf{B} \cdot \nabla \theta) R dr. \quad (6)$$

It can be shown (see Section 1.5.1) that the poloidal flux ψ_p is constant on each toroidal surface formed by the nested magnetic field lines. These surfaces are thus called *flux surfaces*, and ψ_p may be used as a radial coordinate.

It is of interest to determine whether, on a given flux surface, a magnetic field line will be closed or not. In other words, if it needs n toroidal turns to make exactly m poloidal turns. The correct way to quantify this characteristic of the flux surfaces is by defining the so-called *safety factor* q ,

$$q(\psi_p) = \frac{1}{2\pi} \oint_{\Gamma} \frac{r}{R} \frac{B_T}{B_p} dl, \quad (7)$$

where the contour Γ is given by the intersection of the flux surface with the poloidal plane (the plane with normal $\nabla \phi$). Here the *poloidal field* is simply $B_p = \mathbf{B} \cdot \nabla \theta = \frac{1}{R} \partial_r \psi_p$. In other words, the safety factor q determines the number of toroidal turns done by a field line for one poloidal turn. Of particular importance are the so-called *rational flux surfaces* (those with a

rational q), so that field lines are closed. Indeed, the safety factor owes its name to the close relationship it has with MHD instabilities, as will be shown later in this chapter.

Since the safety factor changes radially, the next parameter of interest is the variation of q as a function of r , called the *magnetic shear* s , which also has a strong effect on MHD stability,

$$s(r) = \frac{r}{q} \frac{dq}{dr}. \quad (8)$$

At last, a key plasma parameter for tokamaks is the *plasma Beta*, β . It gives the ratio of pressure forces against magnetic forces, and is defined as

$$\beta = \frac{2\mu_0 \langle p \rangle}{\langle B_T^2 + B_p^2 \rangle}, \quad (9)$$

where the averaged quantities are defined by

$$\langle p \rangle = \frac{1}{V_0} \int_{V_0} p \, dV. \quad (10)$$

Here, V_0 is the total plasma volume. Alternatively, the *toroidal* and *poloidal plasma Betas* are defined respectively as

$$\beta_t = \frac{2\mu_0 \langle p \rangle}{B_0^2}, \quad (11)$$

$$\beta_p = \frac{2\mu_0 \langle p \rangle}{\bar{B}_p^2}, \quad \bar{B}_p = \frac{\mu_0 I_0}{2\pi a} \quad (12)$$

where B_0 is the toroidal magnetic field amplitude evaluated at the *magnetic axis* (the plasma centre), ie. B_0 is the maximum amplitude of B_T in the poloidal cross section. I_0 is the total toroidal plasma current, and a is the minor radius. These parameters give an evaluation of the confinement efficiency relative to the toroidal component and the poloidal component of the magnetic field. Together with the q -profile and the magnetic shear s , the plasma beta plays a key role in MHD stability.

1.2.2 X-point Geometry

All these concepts are presented in cylindrical geometry, but other poloidal flux configurations may be used. Of course the near-circular configuration is the simplest one and it has been used experimentally for a long time. In a tokamak, the plasma is well confined as long as flux surfaces are closed,

but interaction with a solid material cannot be avoided. Thus, two regions are formed : the *plasma core*, with closed flux surfaces, and the *Scrape-Off-Layer* (SOL), where flux surfaces are open onto so-called *Plasma-Facing Components* (PFC's). These two regions are separated by the last closed flux surface called the *separatrix*, or *plasma boundary*. Another region of interest is the *plasma edge*, just inside the separatrix, where strong pressure gradients build up when the plasma is heated up. Two magnetic configurations are commonly used.

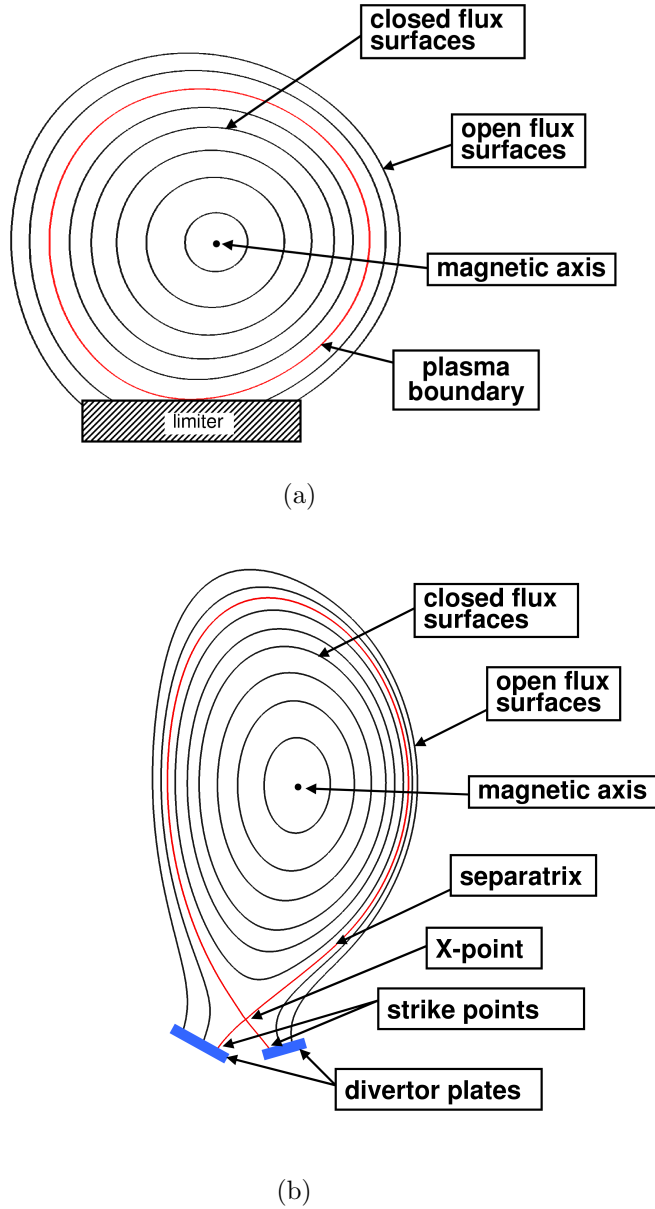
The first configuration is called the *limiter configuration*. Here, the plasma boundary is formed simply by introducing a material structure into the plasma (the *limiter*). Limiter plasmas are still actively used today, which is the case of Tore Supra, in Cadarache (France). The second configuration is called the *divertor* or *X-point configuration*. In order to improve plasma-wall interactions and plasma confinement, an additional axisymmetric coil is introduced near the plasma so that the poloidal magnetic field vanishes at a chosen radial position. This forms an X-point in the poloidal flux, as shown in Figure 1.5. The separatrix is the flux surface that forms the X-point. This configuration enables better confinement since there is no more direct interaction between the plasma core and PFC's. The so-called *divertor*, that replaces the limiter, is placed on the open part of the separatrix, as shown in Fig.5. Thus, since particles follow field lines, as soon as plasma escapes from the core through the separatrix, it is quickly transported to the divertor by open field lines. The points where the separatrix hits the divertor are called the *strike points*, since it is there that most of the energy, lost through the separatrix, arrives. It is important to note that since the poloidal magnetic field B_p vanishes at the separatrix, the safety factor q diverges to infinity. Thus, in order to quantify q at the edge of the plasma, the q_{95} is defined as the safety factor at $\psi_N = 0.95$, where the normalized flux is defined as $\psi_N = \frac{\psi}{\psi_{sep}}$, ψ_{sep} being the value of ψ at the separatrix. Note that the poloidal flux has been defined in (6) so that its value at the *magnetic axis* is zero - the magnetic axis is the centre of the plasma, see Fig.5.

Most machines that are built since the 1980's are X-point tokamaks. Other configurations were also tried, in particular double X-point tokamaks, by adding a second X-point opposite to the first one, which is the case of the tokamak DIII-D (USA). The future tokamak ITER is designed to operate with a single X-point.

1.2.3 Plasma-Facing Components

The Plasma-Facing Components, both in limiter and divertor configurations, have to survive extremely high temperatures. In sight of building a com-

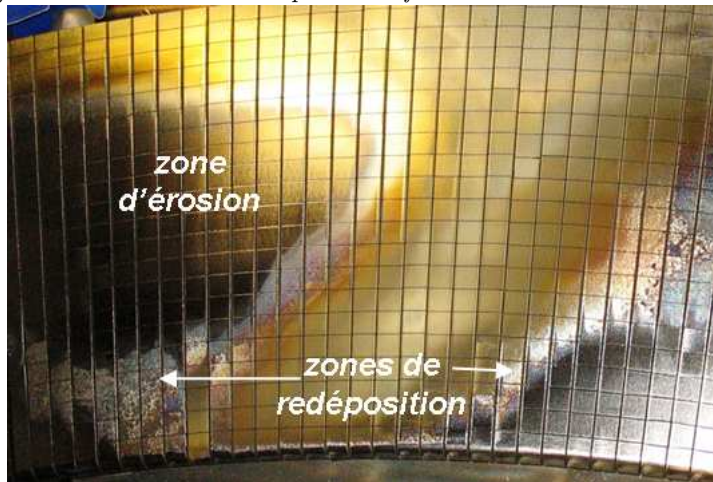
Figure 5: *Limiter and X-point Configurations.*



mercial fusion reactor, with a routine temperature of at least 10keV , material studies represent a crucial part of fusion research. So far the most commonly used materials are *Carbon Fiber Composites* (CFCs) or *carbon graphite*. At high temperatures, this material is eroded and impurities penetrate the plasma. The advantage of CFCs is that their erosion rate is rela-

tively small, giving the PFCs a rather long life-time. Besides, the impurities resulting from erosion do not deteriorate plasma stability so much, at least not directly. In fact, these impurities are progressively redeposited randomly in various places of the vacuum vessel. Eventually, this redeposited graphite reduces the performances of the tokamak. In addition, Tritium co-deposits with impurities into the CFCs, which is most inconvenient due to its radioactivity.

Figure 6: *Erosion and redeposition of the CFC limiter in Tore Supra*



An alternative to CFCs is Tungsten ${}_{74}\text{W}$ and Beryllium ${}_{4}\text{Be}$. These metals have the advantage of having a much lower erosion rate than carbon graphite, and the penetration of Tritium into these materials is much weaker, which is important when planning on a commercial reactor. On the other hand, tungsten impurities are worse than graphite in terms of plasma stability, and the melting of a metallic PFC in a tokamak may considerably affect plasma performances. Therefore, the restrictions concerning heat loads on PFCs are more severe with tungsten and beryllium. Tungsten PFCs have already been tested on X-point tokamaks such as ASDEX-Upgrade (Germany), and JET (UK) was initially conceived with beryllium for some of its PFCs. A tungsten divertor is currently under construction for JET, and the future device ITER has been designed with tungsten and beryllium PFCs. Fig.6 shows the erosion and redeposition of carbon graphite on the limiter of Tore Supra.

1.2.4 Heating Systems, Particle Injection

One of the most important aspects of a tokamak configuration is the plasma heating. Strong heating systems have to be used before fusion reactions

produce enough energy to maintain the plasma temperature at the optimal value. In order to reach the temperatures required for fusion, different kinds of plasma heating may be used. The first system is called *Ohmic* (or resistive) *heating*, which consists in using the current drive needed to produce the poloidal flux. In a way, this heating system is similar to a light bulb: it makes use of the *electrical resistivity* of the plasma to increase temperature by running a current through the plasma. However, the plasma resistivity decreases with increasing temperature, so that the efficiency of the ohmic heating system is limited. Another heating system, called *Neutral-Beam Injection* (NBI), consists in injecting neutral particles with high speed into the plasma. Once ionized, these particles are trapped in the magnetic field and heat the plasma by colliding with other particles. This system is used as an additional heating to the Ohmic heating. It has a particularity which has a strong influence on plasma behavior and stability: if the injector is oriented perpendicular to the ϕ -direction, the NBI simply heats up the plasma, but if the injection is done with a direction tangential to the torus, it induces a strong toroidal rotation of the plasma. This phenomena has long been observed on NBI-heated tokamaks [ref.], and its consequence on plasma stability is extensively studied [ref.]. Tokamaks may have a set of multiple NBIs, but other additional heating systems may be used, such as *Ion* and *Electron Cyclotron Resonance Heatings* (ICRH and ECRH). These high frequency oscillators produce waves whose energy transfers to the charged particles via resonance, just like in a micro-wave oven. ITER is designed to include all these heating systems. Fig.7 shows an ICRH antenna on TORE-SUPRA.

Figure 7: *ICRH Antenna on TORE-SUPRA.*



Just as important as heating, the plasma fueling is one of the main challenges of tokamak operation. Although, in a commercial reactor, the heating systems could be turned down once ignition starts, some burning fuel needs to be injected at a regular rate. There are two common methods. The first one, called *gas puffing*, consists in simply injecting some particles into the vacuum chamber. Eventually, it will penetrate the plasma and be ionized. A more efficient fueling, called *pellet injection*, fires small cubes (few mm) of frozen matter into the plasma, at high speeds (several hundreds of $\text{m}\cdot\text{s}^{-1}$). This way, the pellet (ice cube) penetrates far into the plasma before diffusing. This fueling system is particularly advantageous, not only because it provides a core fueling of the plasma, but also because it may be used for *ELM-pacing*, as will be presented later in this chapter.

1.3 Magneto-Hydro-Dynamics

1.3.1 Ideal MHD equations

Tokamak plasmas are relatively dense, in comparison to cosmic plasmas. Given this high density, a small increment of plasma contains enough particles to give a good representation of the physical properties of the plasma as a whole. This approach is the same as that of a fluid, which entitles it as *Magneto-Hydro-Dynamics*. Thus, the *only* difference with a fluid here is that a plasma carries electrical currents and magnetic fields. With this generalized fluid description of the plasma, it is arguable that a wide amount of plasma physics is ignored (like kinetic effects). The counter argument to this is that such an approach enables the derivation and understanding of some of the most basic properties of tokamak plasmas. Also, the simplicity of the model is balanced by the fact that it gives the possibility to consider the complex geometry of tokamaks. In particular, ideal MHD may be used to describe how the magnetic configuration of a tokamak holds the plasma in equilibrium, as will be seen in the next section. First, the MHD equations should be introduced.

The *ideal MHD* model is given by the *continuity*, *momentum* and *energy equations* for the density ρ , the fluid velocity \mathbf{v} and the pressure p respectively,

$$\frac{\partial \rho}{\partial t} + \nabla \cdot (\rho \mathbf{v}) = 0, \quad (13)$$

$$\rho \frac{d\mathbf{v}}{dt} = \mathbf{J} \times \mathbf{B} - \nabla p, \quad (14)$$

$$\frac{d}{dt} \left(\frac{p}{\rho^\gamma} \right) = 0, \quad (15)$$

together with the *low-frequency pre-Maxwell's equations* for the electric field \mathbf{E} , the magnetic field \mathbf{B} and the current density \mathbf{J} ,

$$\mathbf{E} + \mathbf{v} \times \mathbf{B} = 0, \quad (16)$$

$$\nabla \times \mathbf{E} = -\frac{\partial \mathbf{B}}{\partial t}, \quad (17)$$

$$\nabla \times \mathbf{B} = \mu_0 \mathbf{J}, \quad (18)$$

$$\nabla \cdot \mathbf{B} = 0. \quad (19)$$

Note that the *convective derivative* $d/dt = \partial/\partial t + \mathbf{v} \cdot \nabla$ has been used, and that the *ratio of specific heats* is $\gamma = 5/3$. Also, the three fluid equations imply that only the total number of particles is considered, so that particle charge does not play a role here. The momentum equation states that the plasma velocity is governed by three forces : the pressure gradient, the magnetic force and the inertial force. The equation that gives the name 'ideal' to the model is Ohm's law (16), which states that the plasma is a perfect conductor (ie. no electrical resistivity, $\eta = 0$).

To give an idea of the underlying physics of the ideal MHD model, a quick description of the derivation of the model is shown. Starting with the full set of Maxwell's equations, so that equations (16) and (18) are replaced by

$$\nabla \cdot \mathbf{E} = \frac{\sigma}{\epsilon_0}, \quad (20)$$

$$\nabla \times \mathbf{B} = \mu_0 \mathbf{J} + \frac{1}{c^2} \frac{\partial \mathbf{E}}{\partial t}, \quad (21)$$

respectively, one calculates the fluid moments of the *Boltzmann equation* for each species,

$$\frac{\partial f_\alpha}{\partial t} + \mathbf{u} \cdot \nabla f_\alpha + \frac{q_\alpha}{m_\alpha} (\mathbf{E} + \mathbf{u} \times \mathbf{B}) \cdot \nabla_{\mathbf{u}} f_\alpha = \left(\frac{\partial f_\alpha}{\partial t} \right)_c. \quad (22)$$

Here, $f_\alpha(\mathbf{r}, \mathbf{u}, t)$ is the distribution function of each species as a function of space, velocity and time. The term on the right-hand side of the equation stands for the change in f_α due to collisions. It is generally assumed that the plasma is fully ionized and that the two species considered are only ions and electrons (ie., $\alpha = i, e$). The light speed may be written as $c = \sqrt{\mu_0 \epsilon_0}$. The current and charge densities are defined respectively by

$$\mathbf{J} = \sum_{\alpha} q_{\alpha} \int \mathbf{u} f_{\alpha} d\mathbf{u}, \quad (23)$$

$$\sigma = \sum_{\alpha} q_{\alpha} \int f_{\alpha} d\mathbf{u}. \quad (24)$$

Then, to obtain the ideal MHD model, it is assumed that the plasma is collision-dominated, which enables the higher-order moments to be approximated, and thus the closure of the system is obtained. This is where the model separates from kinetic theory, although a consistent interaction may be established, if the diffusion coefficients of the MHD model are calculated from transport theory. In addition, the high-frequency, short-wavelength information of the system is eliminated, which thus determines a range of validity of the equations in terms of time- and length-scales. A more detailed derivation of the MHD equations can be found in [2].

1.3.2 Validity of MHD

The assumption concerning collision-dominated plasma is the key that leads from kinetic theory to MHD. This is the basic requirement for a fluid model, so that if particles remain relatively close to their neighbours, a division of the plasma into small increments gives a good description of the physics. For collision-dominated fluids, the distribution functions are rapidly randomized, leading to a single scalar, isotropic pressure p . If the distribution functions of the ions and electrons are nearly locally Maxwellian, well-established theories [3] provide expressions for the higher-order moments in terms of transport coefficients. In particular, the *momentum viscosity* μ , the *electrical resistivity* η and the *parallel thermal conductivity* κ_{\parallel} are defined. The *perpendicular diffusivity* D_{\perp} and *perpendicular conductivity* κ_{\perp} have to be separately determined by transport and turbulence theory (see further down). This gives an intermediate model, often called *resistive MHD*, which is then further reduced in order to obtain the ideal MHD model. This next step assumes all viscous, resistive and conductive terms to be negligible when compared to other terms of the corresponding equations. The requirement needed for this derivation may be summarized by stating that collisions happen at a much faster rate than the thermal propagation of the plasma. In other words,

$$V_{T_i} \frac{\tau_i}{a} \sim V_{T_e} \frac{\tau_e}{a} \ll 1, \quad (25)$$

where τ_e and τ_i are the *electron* and *ion collision times*, respectively.

The second approximation used to obtain the ideal MHD model is that high-frequency, short-wavelength information may be ignored. This is done by assuming that all electromagnetic waves considered have much lower phase velocity than the speed of light, so that $\omega/k \ll c$, where ω is the frequency of the wave and k its wave vector. Likewise, the characteristic thermal velocities should be non-relativistic, so that $V_{T_i}, V_{T_e} \ll c$, where $V_{\alpha} = \sqrt{2T_{\alpha}/m_{\alpha}}$. These assumptions reduce equation (21) to (18), but its consequence is that

all plasma phenomena must have a typical frequency ω smaller than the *electron plasma frequency*, $\omega \ll \omega_{pe} \sim 0.8 \times 10^{12}\text{Hz}$, and a characteristic length bigger than the *Debye length*, $k \gg \lambda_d = V_{Te} \sim 2.4 \times 10^{-5}\text{m}$. These limiting values are given by $\omega_{pe} = \sqrt{ne^2/m_e\epsilon_0}$ and $\lambda_d = V_{Te}/\omega_{pe}$. Since the typical MHD length $a \sim 1$ is that of the overall plasma dimension (\sim plasma radius), and the typical speed of MHD phenomena is the thermal velocity of ions, the typical MHD time is $\tau_M = a/V_{Ti}$. For a Deuterium plasma of 10keV, this typical MHD time is $\tau_M \sim 0.7 \times 10^{-6}\text{s}$, so that MHD phenomena are well inside the required values. The basic time- and length-scales of tokamak plasmas are summarized in Fig.8.

The third assumption that reduces equation (20) to (16) is called the *quasi-neutrality* approximation. It means that the ion and electron densities are locally equal, which is consistent with the above assumption, since on the relatively long MHD time, the electrons have more than enough time to react and create an electric field which maintains the plasma in local quasi-neutrality.

The last approximation needed to obtain the momentum equation (14) is that electron inertia is neglected in the momentum equation, which is equivalent to say that the electron mass is negligible compared to the ion mass, or that the electrons have an infinitely quick response to plasma waves. Again, this is consistent with the above time and length scales. However, some low-frequency, long-wavelength modes such as *drift waves* [4] may be affected by electron dynamics, so one should bear in mind that ideal MHD may fail to describe certain phenomena that only rigorous kinetic description can embrace.

Electron gyro period	τ_{ce}	$7.1 \times 10^{-12}\text{s}$
Ion gyro period	τ_{ci}	$2.6 \times 10^{-8}\text{s}$
MHD time	τ_M	$2.3 \times 10^{-6}\text{s}$
Electron collision time	τ_e	$1.0 \times 10^{-5}\text{s}$
Ion collision time	τ_i	$8.9 \times 10^{-4}\text{s}$
Electron gyro radius	r_{ie}	$2.1 \times 10^{-5}\text{m}$
Debye length	λ_d	$2.4 \times 10^{-5}\text{m}$
Ion gyro radius	r_{ii}	$1.3 \times 10^{-3}\text{m}$
MHD length	a	1.0 m
Ion mean-free-path	λ_i	$2.8 \times 10^2\text{m}$
Electron mean-free-path	λ_e	$2.8 \times 10^2\text{m}$

Figure 8: *The typical time- and length- scales in plasma physics.*

Although the general validity of ideal MHD is rather severe, the most important aspect to have in mind is that even if the model is not adapted to fusion plasmas (mainly because of the assumptions on dominant collisions and null resistivity), it gives a very good description of some of its basic behaviours. This is the main argument associated to the validity of ideal MHD: it is restricted, but nevertheless very powerful.

1.3.3 Boundary Conditions

In order to solve the ideal MHD equations, an adequate set of boundary conditions is necessary. There are three types of boundary conditions concerning tokamak plasmas. The first is to assume that the plasma is confined inside a perfectly conducting wall, in which case the tangential electric field and the normal magnetic field have to vanish at the wall. This then implies, using Ohm's law (16), that the normal component of the velocity also has to vanish at the wall, so that the corresponding set of boundary conditions is

$$\nabla \times \mathbf{E}|_{wall} = 0, \quad (26)$$

$$\nabla \cdot \mathbf{B}|_{wall} = 0, \quad (27)$$

$$\nabla \cdot \mathbf{v}|_{wall} = 0. \quad (28)$$

The second type of boundary conditions is if the plasma is separated from the wall by a vacuum region. Since the plasma equations do not apply there, the equations governing the vacuum are

$$\nabla \times \hat{\mathbf{B}} = 0, \quad (29)$$

$$\nabla \cdot \hat{\mathbf{B}} = 0, \quad (30)$$

with boundary condition $\hat{\mathbf{n}} \cdot \hat{\mathbf{B}}|_{wall} = 0$. Here the hat denotes a vacuum variable. Then, assuming that there is no surface current at the plasma-vacuum boundary (pvb) and that pressure tends to zero at the plasma edge, the conditions of plasma-vacuum interactions are restricted to the magnetic field:

$$\mathbf{n} \cdot \mathbf{B}|_{pvb} = \mathbf{n} \cdot \hat{\mathbf{B}}|_{pvb}, \quad (31)$$

$$\mathbf{n} \times \mathbf{B}|_{pvb} = \mathbf{n} \times \hat{\mathbf{B}}|_{pvb}, \quad (32)$$

$$B^2|_{pvb} = \hat{B}_{pvb}^2. \quad (33)$$

This gives four conditions for three components of the magnetic field. The last degree of freedom comes from the plasma boundary $r(\theta, \phi, t)$, which has to be determined. This is called a *free boundary* problem. A simpler

solution is to choose the plasma shape and calculate the corresponding outer wall, which is called the *fixed boundary* problem.

The third and most appropriate (hence most difficult) type of boundary conditions is if the plasma is surrounded by external coils. Here the plasma-vacuum boundary conditions remain the same, but the vacuum field becomes $\hat{\mathbf{B}} = \mathbf{B}_a + \tilde{\mathbf{B}}$, where \mathbf{B}_a is the field induced by the coils and $\tilde{\mathbf{B}}$ is the field induced by the plasma. This set of boundary conditions provides the most realistic description of an experimental plasma, but its complexity generally requires the use of numerical computations, in particular because the external coils are separated by vacuum regions.

1.3.4 Conservation Laws

The ideal MHD equations may be expressed in conservation form $\frac{\partial}{\partial t}(\cdot) + \nabla \cdot (\cdot)$, and their integration on the boundary conditions then give global conservation laws. Of particular interest for plasma physics is the conservation of flux, that leads to the notion of *frozen field lines*. Consider a random surface S moving in the plasma at velocity \mathbf{u} . The rate of change of the magnetic flux through this surface is given by

$$\frac{\partial \psi}{\partial t} = \int \left(\frac{\partial \mathbf{B}}{\partial t} \cdot \mathbf{n} \right) dS - \oint (\mathbf{u} \times \mathbf{B}) \cdot d\mathbf{l}, \quad (34)$$

where $\psi = \int (\mathbf{B} \cdot \mathbf{n}) dS$ is the magnetic flux. Using Faraday's law (17) for $\partial_t \mathbf{B}$ and applying Stokes' theorem to obtain a contour integral gives

$$\frac{\partial \psi}{\partial t} = - \oint (\mathbf{E} + \mathbf{u} \times \mathbf{B}) \cdot d\mathbf{l}. \quad (35)$$

Hence, if the surface velocity corresponds to the plasma velocity, Ohm's law (16) implies that $\partial_t \psi = 0$. The common picture to represent the consequence of this conservation law is to take the surface S to be a very thin tube of plasma around a field line. This conservation law implies that the plasma moves together with the field lines.

This is what characterizes ideal MHD : the magnetic topology is restricted and no *reconnection* of field lines is allowed, which is due to the fact that fluid (plasma) elements are not allowed to tear into separate pieces. In practice, it may be energetically favorable for field lines to reconnect into new configurations with lower potential energy, and it follows that the introduction of a resistivity in Ohm's law may have important consequences on plasma stability.

1.3.5 Non-Ideal MHD models

As seen above, in order to derive the ideal MHD equations, there are multiple intermediate steps following the first closure of the Boltzmann equations into the fluid model. In fact, this is a particularity of MHD that may be used as a powerful tool: although a lot of physics has been ignored to execute the derivation of ideal MHD, selected physics may be kept. It gives the possibility to study some particular kinetic or fluid effects on MHD stability, which is particularly relevant when one awaits a specific effect, based on experimental observation or theoretical predictions. A good example of such a mixture is the introduction of effects due to fast particles for the study of Alfvén Eigen Modes (TAE's, BAE's) [5]. This theory is not relevant for the study of ELMs, but it demonstrates that it is possible to consider kinetic effects in a fluid model. There are more common non-ideal MHD models that may prove useful when considering ELMs, in particular three of them: resistive MHD, the two-fluid model and reduced MHD.

For ideal MHD, all resistive, viscous, conductive and diffusive terms have been ignored. Keeping these terms will make the model far more complex to analyze, but nonetheless more accurate. In particular, reconnection of magnetic field lines is allowed due to resistivity. This phenomenon is known to occur in many MHD instabilities such as the tearing modes [6], so in a way, the resistive model may be necessary for the study of some MHD instabilities. The resistive MHD equations are obtained by introducing resistivity in Ohm's law (16),

$$\mathbf{E} + \mathbf{v} \times \mathbf{B} = \eta \mathbf{J}, \quad (36)$$

with the *Spitzer resistivity* $\eta = \frac{m_e}{n_e^2 \tau_e}$. In a similar way, the diffusivity D , the viscosity μ and the conductivity κ may also be introduced in the mass, momentum and energy equations respectively,

$$\frac{\partial \rho}{\partial t} + \nabla \cdot (\rho \mathbf{v}) = \nabla \cdot (D \nabla \rho) + S_\rho, \quad (37)$$

$$\rho \frac{d\mathbf{v}}{dt} = \mathbf{J} \times \mathbf{B} - \nabla p + \mu \nabla^2 \mathbf{v}, \quad (38)$$

$$\frac{d}{dt} \left(\frac{p}{\rho^\gamma} \right) = \nabla \cdot (\kappa \nabla p) + S_H, \quad (39)$$

where S_ρ and S_H are the particle and heating sources respectively. In tokamak physics, it is common to separate the gradient into two parts; namely, the *parallel component* of the magnetic field, ∇_{\parallel} , and the *perpendicular compo-*

nent ∇_{\perp} , with

$$\nabla_{\parallel} = \frac{1}{B^2} \mathbf{B} (\mathbf{B} \cdot \nabla) \quad (40)$$

$$\nabla_{\perp} = \nabla - \nabla_{\parallel} \quad (41)$$

Hence, the diffusivity and conductivity terms are usually separated into perpendicular and parallel components as well: $\nabla \cdot (D_{\perp} \nabla_{\perp} \rho + D_{\parallel} \nabla_{\parallel} \rho)$ and $\nabla \cdot (\kappa_{\perp} \nabla_{\perp} p + \kappa_{\parallel} \nabla_{\parallel} p)$.

Another set of equations that may lead to interesting physics is the *two-fluid model*, where the ion and electron pressures are kept distinct,

$$\frac{d}{dt} \left(\frac{p_i}{\rho^\gamma} \right) = \nabla \cdot (\kappa_i \nabla p_i) + S_{H_i}, \quad (42)$$

$$\frac{d}{dt} \left(\frac{p_e}{\rho^\gamma} \right) = \nabla \cdot (\kappa_e \nabla p_e) + S_{H_e}. \quad (43)$$

This model may prove useful for studying the different behaviours of ion and electron temperatures. In particular, the parallel conductivity is different due to the heavier mass of ions, so that electron temperature is conducted much faster along field lines. The correct expressions for the parallel conductivities are given by [7],

$$\kappa_{i,\parallel} = 3.9 \frac{\rho T_i \tau_i}{m_i}, \quad (44)$$

$$\kappa_{e,\parallel} = 3.16 \frac{\rho T_e \tau_e}{m_e}, \quad (45)$$

where the collision times are

$$\tau_i = 0.75 \pi^{3/2} \frac{m_i^{3/2} \epsilon_0^2}{\rho e^4} T_i^{3/2}, \quad (46)$$

$$\tau_e = 0.75 \pi^{3/2} \left(\frac{m_e}{2m_i} \right)^{1/2} \frac{m_i^{3/2} \epsilon_0^2}{\rho e^4} T_e^{3/2}. \quad (47)$$

Hence, if we assume that $T_i \approx T_e$, we have that

$$\frac{\kappa_{e,\parallel}}{\kappa_{i,\parallel}} = \frac{3.16}{3.9} \left(\frac{m_i}{2m_e} \right) \sim 35. \quad (48)$$

It should also be noted that these parallel conductivities depend on temperature as $\kappa_{\alpha,\parallel} \sim T_{\alpha}^{5/2}$, which is important, in particular when considering the plasma edge. For example, if a small blob of warm plasma crosses the separatrix, its temperature falls quickly due to fast parallel conductivity.

The third model is called *reduced MHD*. This is an approximation of MHD often used in tokamak plasma theory and was first derived by Strauss [8,9]. The toroidal component of the magnetic field being much larger than the poloidal one, it is common to define the perpendicular direction as $\times \nabla \phi$ instead of $\times \mathbf{B}$. The main reason for doing this is that it simplifies the non-linearity of the momentum equation, since the perpendicular plasma velocity is not related to the magnetic field anymore. We have $\mathbf{v}_\perp = R^2 \nabla \phi \times \nabla u$ instead of $\mathbf{v}_\perp = R^2 \mathbf{B} \times \nabla u$ - here, u is the electric potential. For more details on the derivation of the relation $\mathbf{v}_\perp = R^2 \mathbf{B} \times \nabla u$, see Appendix A.

1.4 Ideal MHD Equilibrium in Tokamaks

1.4.1 The Grad-Shafranov Equation

In order to obtain a clear description of a tokamak equilibrium, recall the concept of magnetic flux surfaces introduced above. A logical way of defining flux surfaces is the following. First, the definition of equilibrium needs to be clarified. In fact, *ideal MHD equilibrium* usually refers to *static equilibrium*, so that in addition to having no temporal evolution ($\partial/\partial t = 0$), the plasma velocity is assumed zero ($\mathbf{v} = 0$). Now, applying these two conditions to the ideal MHD equations (13-19) gives

$$\mathbf{J} \times \mathbf{B} = \nabla p, \quad (49)$$

$$\nabla \times \mathbf{B} = \mu_0 \mathbf{J}, \quad (50)$$

$$\nabla \cdot \mathbf{B} = 0. \quad (51)$$

Equation (49) implies that $\mathbf{B} \cdot \nabla p = \mathbf{J} \cdot \nabla p = 0$, which means that magnetic field lines and current lines lie on surfaces of constant pressure. In general, the angle between magnetic and current lines is arbitrary. These $p = \text{const}$ surfaces are called magnetic flux surfaces. The centre of the plasma, where pressure has a maximum, is called the *magnetic axis*. It follows from equation (5) that the poloidal flux is constant on flux surfaces, since $\psi = \psi(p)$, hence the name.

The *Grad-Shafranov equation* is a two-dimensional, nonlinear elliptic partial differential equation obtained by adding a third condition to the static equilibrium equations (49-51): toroidal axisymmetry (Grad and Rubin, 1958 [10]; Shafranov, 1960 [11]). In the (R, Z, ϕ) coordinate system, it is equivalent to setting $\partial/\partial \phi = 0$.

Applying this new condition to equation (51) gives, in toroidal geometry,

$$\frac{1}{R} \frac{\partial (RB_R)}{\partial R} + \frac{\partial B_Z}{\partial Z} = 0. \quad (52)$$

This gives the connection between the poloidal flux and the magnetic field, by introducing ψ as a stream function for the poloidal magnetic field:

$$B_R = -\frac{1}{R} \frac{\partial \psi}{\partial Z}, \quad (53)$$

$$B_Z = \frac{1}{R} \frac{\partial \psi}{\partial R}. \quad (54)$$

This can also be integrated to give the poloidal magnetic field \mathbf{B}_p

$$\mathbf{B} = B_\phi \mathbf{e}_\phi + \mathbf{B}_p, \quad (55)$$

$$\mathbf{B}_p = \frac{1}{R} \nabla \psi \times \mathbf{e}_\phi. \quad (56)$$

Introducing this into equation (6) verifies the analogy $\psi_p = 2\pi\psi$ between the poloidal flux and the stream function. Note that the initial definition of the poloidal flux implies that the flux ψ_p is automatically zero at the magnetic axis. Thus, it is convenient to set the flux to zero at the magnetic axis, which is equivalent to setting the arbitrary constant, which arises from integration, to zero. In general, the flux surfaces are labeled with the flux, in contrast to $p = \text{const}$ surfaces. Then, whether one uses ψ or ψ_p does not have much implications in theoretical derivations, but when dealing with real quantifications, one should clearly specify which of the two is used.

Ampere's law may now be considered by using the notation (55,56)

$$\mu_0 \mathbf{J} = \mu_0 J_\phi \mathbf{e}_\phi + \frac{1}{R} \nabla (R B_\phi) \times \mathbf{e}_\phi, \quad (57)$$

$$J_\phi = -\frac{1}{\mu_0 R} \Delta^* \psi, \quad (58)$$

where the Grad-Shafranov operator is defined as

$$\Delta^* \psi = R^2 \nabla \cdot \left(\frac{\nabla \psi}{R^2} \right) = R \frac{\partial}{\partial R} \left(\frac{1}{R} \frac{\partial \psi}{\partial R} \right) + \frac{\partial^2 \psi}{\partial Z^2}. \quad (59)$$

At last, these two identities need to be introduced into the momentum equation (49). As above, it is useful to use the projection along \mathbf{B}, \mathbf{J} and $\nabla \psi$ separately. The first projection gives $\mathbf{B} \cdot \nabla p = 0$, which can be written as

$$\mathbf{e}_\phi \cdot (\nabla \psi \times \nabla p) = 0. \quad (60)$$

This certifies that p is a surface quantity, $p = p(\psi)$. Similarly, projecting on \mathbf{J} gives

$$\mathbf{e}_\phi \cdot (\nabla \psi \times \nabla (R B_\phi)) = 0, \quad (61)$$

so that RB_ϕ is also a surface quantity $RB_\phi = F(\psi)$. It should be noted that the function $F(\psi)$ may be substituted into the formulation of the poloidal current (57). The Grad-Shafranov equation is obtained by introducing the two flux functions $p(\psi)$ and $F(\psi)$ into the $\nabla\psi$ projection of the momentum equation, giving the *Grad-Shafranov equation*

$$\Delta^*\psi = -\mu_0 R^2 \frac{dp}{d\psi} - F \frac{dF}{d\psi}. \quad (62)$$

The two functions $p(\psi)$ and $F(\psi)$ are thus free functions. The choices of these two functions, together with the boundary conditions for ψ associated to the equation, determine the equilibrium of plasma pressure against magnetic forces.

1.4.2 Tokamak Equilibrium

The equilibrium configuration of interest here is the tokamak configuration. There are many different tokamak configurations, and the Grad-Shafranov equation can be solved to obtain a description of the equilibrium. Although numerical computation is more straight forward, analytical solutions of the equation may be computed, either for special cases, or for relatively simple configurations. One important feature is that the analytical approach of the Grad-Shafranov equation enables one to determine the additional vertical magnetic field needed to counter the toroidal force acting on the plasma due to the $1/R$ dependence of the toroidal field. As an example, the equilibrium of a high- β tokamak is derived here. This derivation will give an insight to the Grad-Shafranov equilibrium of tokamaks in a more general consideration, and it will introduce an important aspect of the equilibrium, called the *Shafranov shift*, which is due to toroidal geometry.

First, it is more convenient to use the poloidal coordinates (r, θ) where r and θ are defined by $r = \sqrt{(R - R_0)^2 + Z^2}$ and $\theta = \tan^{-1} \left(\frac{Z}{R - R_0} \right)$. Then, the assumption of *large aspect ratio* will be made, that is $\epsilon = a/R_0 \ll 1$.

This leads to the following expansion for the main plasma parameters,

$$\frac{B_p}{B_\phi} \sim \epsilon, \quad (63)$$

$$\beta_t \sim \frac{2\mu_0 p}{B_\phi^2} \sim \epsilon, \quad (64)$$

$$\beta_p \sim \frac{2\mu_0 p}{B_p^2} \sim \frac{1}{\epsilon}, \quad (65)$$

$$q \sim \frac{rB_\phi}{RB_p} \sim 1, \quad (66)$$

$$\frac{\psi}{rRB_\phi} \sim \epsilon, \quad (67)$$

where $B_p = |\mathbf{B}_p| = \sqrt{B_r^2 + B_\theta^2}$. Note that $q \sim 1$ is needed for stability, so that $B_p/B_\phi \sim \epsilon$ follows immediately. The ordering of β_p means that the poloidal field has only a minor effect on the radial pressure balance, but is still required for the toroidal force balance (as seen previously). The last ordering $\psi/rRB_\phi \sim \epsilon$ expresses the fact that the force due to the toroidal magnetic field is larger than that due to the poloidal flux. Hence, the function $F(\psi)$ has to provide the pressure balance, so the appropriate expression is the following

$$F^2(\psi) = R_0^2 B_0^2 \left[1 - \frac{2\mu_0 p(\psi)}{B_0^2} + \frac{2B_{\phi 2}(\psi)}{B_0} \right], \quad (68)$$

where $B_{\phi 2}(\psi)$ is the new free function, and where B_0 is the vacuum toroidal field at $R = R_0$. Introducing this function into the Grad-Shafranov equation gives the equation

$$\nabla^2 \psi = -R_0^2 B_0^2 \left[\frac{B'_{\phi 2}}{B_0} + \frac{2\mu_0 p'}{B_0^2} \frac{r}{R_0} \cos \theta \right], \quad (69)$$

where prime denotes differentiation with respect to ψ . Note that the Grad-Shafranov operator has reduced to the Laplacian. This is done by expanding the operator as

$$\Delta^* \psi = \nabla^2 \psi - \frac{2}{R} \nabla \psi \cdot \nabla R \quad (70)$$

$$= \nabla^2 \psi + 2\mathbf{B}_p \cdot \nabla \theta \quad (71)$$

$$= \nabla^2 \psi + 2B_\theta. \quad (72)$$

Thus, the first term scales as $\nabla^2 \psi \sim \psi/r^2$, so that multiplying both terms by r/RB_ϕ gives $\psi/rRB_\phi \sim \epsilon$ for the first term and $rB_\theta/RB_\phi \leq rB_p/RB_\phi \sim \epsilon^2$

for the second term. Thus, the Grad-Shafranov operator reduces to the Laplacian at first order in ϵ . Usually, equation (69) is solved numerically, but for special choices of $B_{\phi 2}(\psi)$ and $p(\psi)$, it can be solved analytically. For example, the *Haas model* takes the free functions to be linear in ψ , so that, say

$$B'_{\phi 2}(\psi) = -\frac{A}{R_0^2 B_0}, \quad (73)$$

$$p'(\psi) = -\frac{C}{2\mu_0 R_0}, \quad (74)$$

with A and C constant. Hence, equation (69) reduces to

$$\nabla^2 \psi = A + Cr \cos \theta, \quad (75)$$

which has solution

$$\psi(r, \theta) = \frac{1}{4}A (r^2 - a^2) + \frac{1}{8}C (r^3 - a^2 r) \cos \theta. \quad (76)$$

$$(77)$$

Note that we chose the boundary condition $\psi(a, \theta) = 0$, since if the plasma surface is circular with radius a and surrounded by vacuum, equation (69) means that the toroidal current is almost uniform in the plasma and jumps to zero at the plasma surface. With the solution for ψ , one may then calculate p , F , and also B_p . It is convenient to express the constants A and C in terms of more physical parameters, such as the *kink safety factor* q_* and the toroidal beta β_t ,

$$\frac{1}{q_*} = \frac{\mu_0 R_0 I_0}{2\pi a^2 B_0} = \frac{R_0}{2\pi a^2 B_0} \int_0^{2\pi} a B_\theta(a, \theta) d\theta = \frac{A}{2B_0}, \quad (78)$$

$$\beta_t = \frac{2\mu_0 \langle p \rangle}{B_0^2} = \frac{2\mu_0}{\pi a^2 B_0^2} \int_0^{2\pi} \int_0^a r p(r, \theta) dr d\theta = \frac{a^2 AC}{8R_0 B_0^2}. \quad (79)$$

Then the expression for ψ takes the form

$$\psi(\rho, \theta) = \frac{a^2 B_0}{2q_*} [\rho^2 - 1 + \nu (\rho^3 - \rho) \cos \theta], \quad (80)$$

where $\rho = r/a$ and $\nu = \beta_t q_*^2 / \epsilon$. The *magnetic axis* is defined to be the point ($r = \Delta_0, \theta = 0$) where $\partial\psi/\partial r = 0$. This gives the *Shafranov shift*

$$\Delta_0 = \frac{a\nu}{1 + \sqrt{1 + 3\nu^2}}. \quad (81)$$

Since with the high- β ordering, $\nu \sim 1$, we have that $\Delta_0 \sim \frac{1}{3}a$, which is not negligible.

Once the equilibrium has been solved, all plasma parameters such as β 's and safety factors may be evaluated, giving a good insight to the characteristics of the high- β tokamak. Similar procedures can be used to solve the Grad-Shafranov equation for more sophisticated plasmas, in particular non-circular plasmas. For complicated equilibria such as X-point plasmas, the equation is usually solved numerically. Fig.9 shows the analytical solution (80) derived above, and an X-point plasma equilibrium solved numerically. In both cases, the Grad-Shafranov shift can clearly be seen.

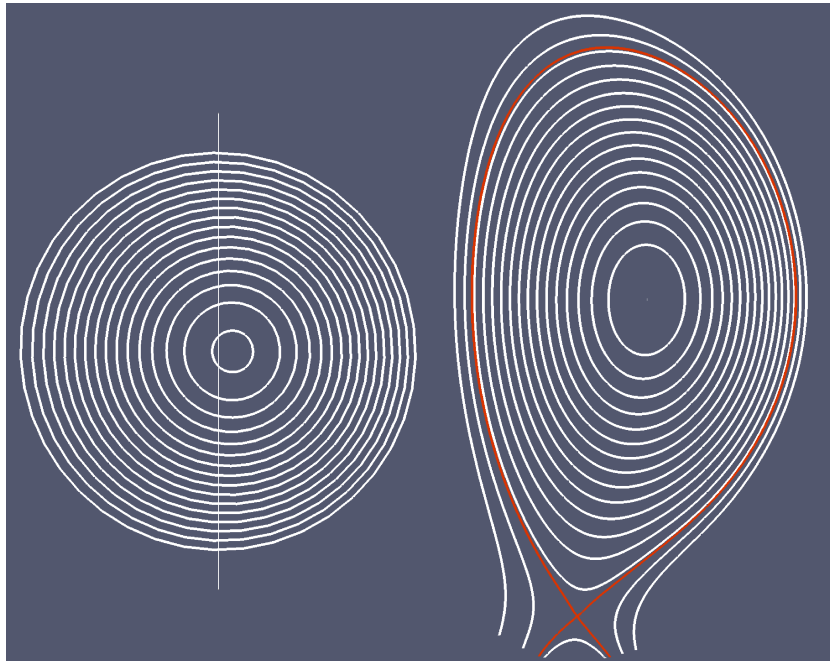


Figure 9: *Left, the analytical solution of the Grad-Shafranov equation for a circular plasma, featuring the Shafranov shift (the distance from the vertical line). Right, the numerical solution of the Grad-Shafranov equation for an X-point plasma.*

1.5 Turbulent Transport and MHD Instabilities

1.5.1 Parallel and Perpendicular Transport

It has been explained above that in a magnetic configuration like the tokamak, charged particles follow field lines by gyrating around them. The speed of a particle along a field line depends on its temperature and mass: $v_{\parallel} = \sqrt{2T/m}$. Since there is no magnetic restriction in the parallel direction,

the particles travel much faster along field lines than in the perpendicular (ie. radial) direction $\nabla\psi$. As a result, density and temperature are quickly redistributed along the magnetic field, so that pressure remains approximately constant on a given flux surface, and thus gradients are mostly radial. In other words, $\partial/\partial\phi \ll \partial/\partial\psi$. It is thus convenient to consider a poloidal cut of the plasma, assuming that the density and temperature distribution on this cut is the same all along the torus. Of course, were this to be true, so that axisymmetry of density and temperature was satisfied at all times, fusion power would be accomplished already! Indeed, turbulent transport and large-scales resonant instabilities affect the plasma and contribute to large radial loss of pressure.

1.5.2 Classical and Neoclassical Predictions

Chronologically, the first mechanism for perpendicular transport that was understood, called *classical transport*, is the diffusion due to electrostatic interactions between particles (collisions). The resulting perpendicular flux may be interpreted as a perpendicular diffusion, using the classical coefficient D_{\perp}^c ,

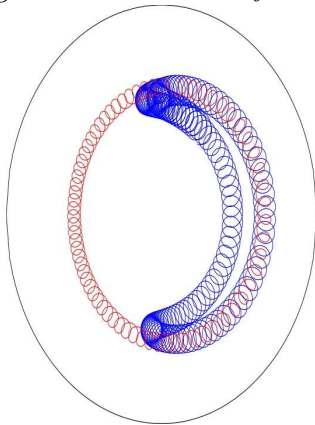
$$\Gamma_{\perp} = -D_{\perp}^c \nabla_{\perp} n. \quad (82)$$

This diffusion coefficient can be expressed as the product of the collision frequency ν_c and the interaction area of particles which is directly related to the Larmor radius, so that $D_{\perp}^c \sim \nu_c \rho_L^2$. The collision frequency depends on the density and temperature of particles $\nu_c \sim nT^{-3/2}$. This frequency varies from around 1kHz in the plasma core to 15kHz at the edge. Since the Larmor radius varies inversely, the classical diffusion coefficient does not vary so much radially. Typically, $D_{\perp}^c \sim 10^{-2} \text{m}^2 \cdot \text{s}^{-1}$.

In a straight toroidal field, the only perpendicular transport would come from this classical diffusion. However, in a tokamak the curvature of field lines gives rise to multiple regimes of perpendicular transport depending on the collisionality of the plasma. In particular, this so-called neoclassical theory explains the presence of *banana particles* in the Low-Field Side of the tokamak: because of the $\frac{1}{R}$ -dependence of B_T , the magnetic field is weaker on the outer side of the torus than on the inner side, hence the notation *High/Low-Field Side* (HFS,LFS). Thus, as particles travel along field lines, the amplitude of the magnetic field varies, inducing a perpendicular drift of the guiding centre of particles (the axis of gyration). It is equivalent to say that the non-uniformity of the magnetic field deviates particles from their parallel trajectory. If the particle speed along the field line is high enough, it will go around the torus and undergo a complete poloidal turn. These are

called *passing particles*. In this case, the perpendicular drift is compensated between LFS and HFS, so that these particles remain passing particles. However, if a particle speed along the field line is too weak, it may be subject to a mirror effect of the magnetic field due to the perpendicular drift. Particles that are captured on the LFS of the torus are called *trapped particles*, or *banana particles*, because the poloidal projection of their trajectories resembles a banana (see Figure 1.8). The banana particles are particularly important when considering plasma edge stability because they produce a parallel current called *bootstrap current* that increases with the pressure gradient [12].

Figure 10: *Banana Trajectories.*



1.5.3 Turbulence

Practically, when operating a tokamak, anomalous perpendicular transport is observed. The averaged perpendicular diffusion D^{exp} observed experimentally is about 100 times higher than the classical and neoclassical predictions. Experimental and theoretical studies have proved that this perpendicular transport is due to turbulence. In fact, turbulent variations of the electric potential results in perpendicular fluxes called electric or $\mathbf{E} \times \mathbf{B}$ drifts. This is the electrostatic part of the turbulence. There is another important effect of turbulence, which is due to the perturbation of the magnetic field. Indeed, as has been stated previously, parallel transport along the field lines is very fast, so that a perturbation of the magnetic field can result in consequent loss of plasma pressure. For example, if a field line initially inside the separatrix is perturbed across the separatrix, it opens an evacuation exit to plasma. However, turbulence is not the only mechanism responsible for radial loss of pressure. Resonant fluctuations may provoke brutal exhausts of part of the plasma pressure. In particular, MHD instabilities considerably restrict toka-

mak performances by limiting the energy confinement, and may also release large amounts of energy from the plasma and thus damage PFCs.

1.5.4 MHD Instabilities

If a given equilibrium is perturbed, the forces induced by the perturbation may lead to an exponential growth of the perturbation amplitude (*instability*). In the case of stability, the forces due to the initial perturbation will either conduct the system to a permanent oscillation around the equilibrium, or eventually bring the system back to the equilibrium state, that is, if the oscillation of the system is damped. Instability may be studied explicitly by expressing each variable with an equilibrium part and a small perturbation term, $Q(\mathbf{r}, t) \rightarrow Q(\mathbf{r}) + \tilde{Q}(\mathbf{r}, t)$, with $\tilde{Q} \ll Q$. When applying this transformation to the static ideal MHD equilibrium equations (49-51), it is convenient to express all perturbed quantities in terms of a so-called *displacement vector* $\boldsymbol{\xi}$ defined by $\tilde{\mathbf{v}} = \partial_t \boldsymbol{\xi}$, with the following initial conditions

$$\boldsymbol{\xi}(\mathbf{r}, 0) = \tilde{\mathbf{B}}(\mathbf{r}, 0) = \tilde{\rho}(\mathbf{r}, 0) = \tilde{p}(\mathbf{r}, 0) = 0, \quad (83)$$

$$\frac{\partial \boldsymbol{\xi}(\mathbf{r}, 0)}{\partial t} = \tilde{\mathbf{v}}(\mathbf{r}, 0) \neq 0. \quad (84)$$

Thus, applying this transformation, the mass conservation equation (13), the energy equation (15) and Faraday's Law (17) may be integrated with respect to time, giving

$$\tilde{\rho} = -\nabla \cdot (\rho \boldsymbol{\xi}), \quad (85)$$

$$\tilde{p} = -\boldsymbol{\xi} \cdot \nabla p - \gamma p \nabla \cdot \boldsymbol{\xi}, \quad (86)$$

$$\tilde{\mathbf{B}} = \nabla \times (\boldsymbol{\xi} \times \mathbf{B}). \quad (87)$$

Note that in order to derive these, the mass conservation needs to be introduced into the energy equation, and Ohm's Law has been used in Faraday's Law. Also, the relation $\nabla \cdot \tilde{\mathbf{B}} = 0$ follows directly from Faraday's Law. Hence, all six equations of the MHD model are respected. Substituting these into the momentum equation (14) gives the equation for the displacement vector $\boldsymbol{\xi}$,

$$\rho \frac{\partial^2 \boldsymbol{\xi}}{\partial t^2} = \mathbf{F}(\boldsymbol{\xi}), \quad (88)$$

$$\mathbf{F}(\boldsymbol{\xi}) = \mathbf{J} \times \tilde{\mathbf{B}} + \tilde{\mathbf{J}} \times \mathbf{B} - \nabla \tilde{p}. \quad (89)$$

Note that using the above expressions (86,87) for \tilde{p} and $\tilde{\mathbf{B}}$, as well as the relation $\mu_0 \mathbf{J} = \nabla \times \mathbf{B}$, the force operator $\mathbf{F}(\boldsymbol{\xi})$ may be expressed in terms

of $\boldsymbol{\xi}$ and equilibrium quantities only,

$$\mathbf{F}(\boldsymbol{\xi}) = \frac{1}{\mu_0}[\nabla \times \mathbf{B}] \times \mathbf{Q} + \frac{1}{\mu_0}[\nabla \times \mathbf{Q}] \times \mathbf{B} + \nabla(\boldsymbol{\xi} \cdot \nabla p + \gamma p \nabla \cdot \boldsymbol{\xi}) \quad (90)$$

where $\mathbf{Q} = \tilde{\mathbf{B}} = \nabla \times (\boldsymbol{\xi} \times \mathbf{B})$.

A first reduction of equation (88) may be obtained by using the common exponential representation $\boldsymbol{\xi}(\mathbf{r}, t) \rightarrow \boldsymbol{\xi}_0(\mathbf{r})\exp(-i\omega t)$. Then, the displacement equation becomes

$$-\omega^2 \rho \boldsymbol{\xi} = \mathbf{F}(\boldsymbol{\xi}), \quad (91)$$

which is called the *normal mode eigenvalue equation*. Now, the force operator \mathbf{F} has the particular property of being self-adjoint, that is, for any two arbitrary displacement vectors $\boldsymbol{\xi}$ and $\boldsymbol{\eta}$, the relation $\int \boldsymbol{\eta} \cdot \mathbf{F}(\boldsymbol{\xi}) = \int \boldsymbol{\xi} \cdot \mathbf{F}(\boldsymbol{\eta})$ holds (integration is done over the plasma volume). Now, applying the computation $\int \boldsymbol{\xi}^* \cdot (\text{eq.91}) - \int \boldsymbol{\xi} \cdot (\text{eq.91})^*$, and making use of the self-adjointness of \mathbf{F} , together with the fact that the displacement vector $\boldsymbol{\xi}$ is arbitrary, one obtains that $\omega^2 = \omega^{*2}$. That is, ω^2 is real. This also implies that the displacement vector $\boldsymbol{\xi}$ is real, since the force operator in equation (91) is real. The consequence of ω^2 being real is most convenient. It means that $\omega^2 > 1$ corresponds to a pure oscillation (stability) and that $\omega^2 < 1$ corresponds to exponential growth (instability). Clearly, the transition from stability occurs at $\omega^2 \approx 0$.

Another way to formulate the normal mode eigenvalue equation is by taking the dot product of $\boldsymbol{\xi}^*$ with equation (91) and then integrating over the plasma volume. This gives the variational formulation of the perturbation equation,

$$\omega^2 = \frac{\delta W(\boldsymbol{\xi}^*, \boldsymbol{\xi})}{K(\boldsymbol{\xi}^*, \boldsymbol{\xi})}, \quad (92)$$

$$\delta W(\boldsymbol{\xi}^*, \boldsymbol{\xi}) = -\frac{1}{2} \int \boldsymbol{\xi}^* \cdot \mathbf{F}(\boldsymbol{\xi}) d\mathbf{r}, \quad (93)$$

$$K(\boldsymbol{\xi}^*, \boldsymbol{\xi}) = \frac{1}{2} \int \rho |\boldsymbol{\xi}|^2 d\mathbf{r}. \quad (94)$$

It may be shown [2] that the variational formulation (92) is exactly equivalent to the normal mode eigenvalue equation (91). Furthermore, the Energy Principle (also proved in [2]) states that the equilibrium is stable (ie. $\omega^2 \geq 0$) if and only if $\delta W(\boldsymbol{\xi}^*, \boldsymbol{\xi}) \geq 0$ for all allowable displacements $\boldsymbol{\xi}$ (ie. those bounded and satisfying the appropriate boundary conditions).

A more explicit form of δW , called the intuitive form of δW , may be obtained after several steps of straight-forward algebra. In particular, one

uses the assumption that the plasma is bounded by a perfectly conducting wall, so that the only boundary condition is $\mathbf{n} \cdot \boldsymbol{\xi}|_{wall} = 0$, where \mathbf{n} is the outward normal to the wall. This permits integration by parts of several terms in δW that result in vanishing surface integrals. Also, defining parallel and perpendicular components for all vector quantities, such that $\mathbf{V} = \mathbf{V}_\perp + V_\parallel \mathbf{b}$, one can greatly simplify the expression for δW . Here, $\mathbf{b} = \mathbf{B}/B$ is the parallel unit vector. The resulting *intuitive form* of δW writes (Furth *et al.*, 1965, [13])

$$\begin{aligned} \delta W(\boldsymbol{\xi}^*, \boldsymbol{\xi}) = & \frac{1}{2} \int \left[\frac{|\mathbf{Q}_\perp|^2}{\mu_0} + \frac{|\mathbf{B}|^2}{\mu_0} (\nabla \cdot \boldsymbol{\xi}_\perp + 2\boldsymbol{\xi}_\perp \cdot \boldsymbol{\kappa})^2 + \gamma p |\nabla \cdot \boldsymbol{\xi}|^2 \right] d\mathbf{r} \\ & - \frac{1}{2} \int [2(\boldsymbol{\xi}_\perp \cdot \nabla p)(\boldsymbol{\xi}_\perp \cdot \boldsymbol{\kappa}) + J_\parallel \mathbf{Q}_\perp \cdot (\boldsymbol{\xi}_\perp^* \times \mathbf{b})] d\mathbf{r}. \end{aligned} \quad (95)$$

where $\boldsymbol{\kappa} = \mathbf{b} \cdot \nabla \mathbf{b}$ represents the *field line curvature*. It is important to understand the role of each term in this expression. The $|\mathbf{Q}_\perp|^2$ term represents the energy required to bend magnetic field lines, the second term represents the energy required to compress magnetic field lines, and the $\gamma p |\nabla \cdot \boldsymbol{\xi}|^2$ term represents the energy required to compress the plasma. Note that these three terms are strictly positive, and thus stabilizing. The second integral represents the unstable contribution, with the first term proportional to the pressure gradient ∇p and the curvature $\boldsymbol{\kappa}$, and the second term proportional to the parallel current density J_\parallel . These are the two quantities that may drive MHD instabilities.

The instabilities driven by parallel currents are called *kink modes*. These modes are macroscopic instabilities with low toroidal and poloidal wave numbers (n, m) , where $\boldsymbol{\xi}(\mathbf{r}) = \boldsymbol{\xi}(r)e^{i(m\theta+n\phi)}$. Experimentally, the most frequent internal kink mode is the so-called *sawteeth* instability, which occurs at the rational surface $q = 1$, and is characterized by the temperature time trace it produces. With constant heating, pressure increases linearly until the stability threshold is reached, leading to a rapid crash and loss of pressure. After the crash, the plasma is stable again and pressure starts rising once more until the next crash, and so on, leading to a time trace of the form rise-crash-rise-crash..., that looks like a sawteeth [6]. The sawteeth is an $m = n = 1$ mode that may be stabilized using various methods, one of which consisting in keeping the whole q -profile above 1. Other current driven instabilities, called external kink-modes, may lead to plasma disruption (loss of all plasma current). These are also low (n, m) instabilities, which are often caused by rational surfaces outside the plasma (in the vacuum region).

Plasma instabilities caused by the pressure gradient can be classified in two categories: *interchange* and *ballooning* modes. Interchange instabilities

are seldom relevant in tokamaks, because of the stabilizing magnetic shear and the favorable field line curvature on the HFS of the plasma. Ballooning modes however, are most relevant in tokamak plasmas, in particular because they set β -limits to experimental performances. As seen from equation (95), the pressure gradient term is balanced by the field line curvature κ , so that the modes are most unstable on the LFS, where curvature is unfavorable. The name ‘ballooning’ comes from the fact that the modes alternate between favorable and unfavorable curvature as they pass inside and outside the torus. In cases where the pressure gradient is steep at the edge of the plasma, near the separatrix, ballooning modes can develop and lead to repetitive crashes, and loss of pressure. Such instabilities are also called *Edge-Localised Modes*.

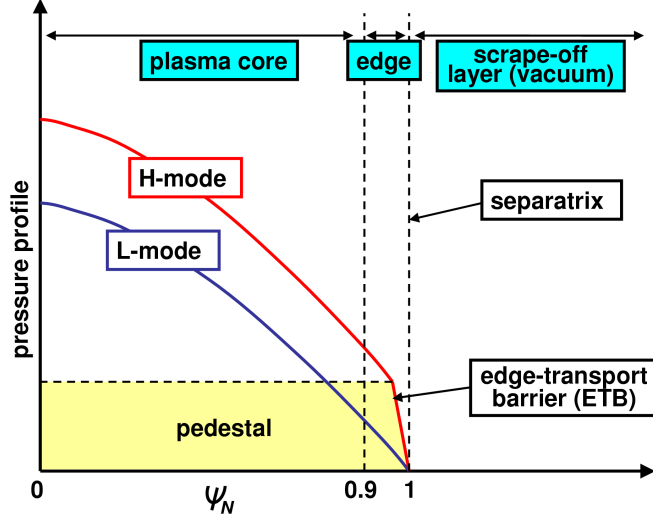
1.6 Edge-Localised-Modes

1.6.1 The H-mode

In the early 1980’s, the German tokamak ASDEX discovered that two different states of plasma confinement existed: by increasing heating power above a certain threshold, an abrupt transition is observed, after which the confinement is considerably improved [14]. In particular, a transport barrier forms at the edge of the plasma, just inside the separatrix (typically between $\psi_N = 0.9$ and $\psi_N = 1$). The resulting pressure gradients at the edge are particularly steep, so that this edge region is often given the name of *pedestal region*, which comes from the shape of radial profiles during the H-mode (with steep gradient at the edge, see Fig.11). In this new regime, the confinement time is improved by a factor 2, which led to the quotation of *H-mode*, where the H stands for High confinement, as opposed to *L-mode* for Low confinement.

After this discovery, the H-mode was achieved in most X-point tokamaks and extensively studied, but despite the strong efforts to try and understand the transition between the L-mode and the H-mode, no theoretical or numerical model has ever been able to reproduce this transition accurately. There is nevertheless a good understanding of the mechanism that produces this *Edge Transport Barrier* (ETB). Experimentally, a strong poloidal rotation of the plasma is observed in the pedestal region, due to a deep well in the radial electric field, and it has been shown theoretically that the strong shear of such a flow (ie. its gradient) destroys turbulent convection cells, thus restricting radial transport [15-19]. The H-mode is the reference operational mode planned for ITER. However, there is a disadvantage to this confinement mode: the strong pedestal gradients provoke violent instabilities at the edge of the plasma.

Figure 11: *L-mode and H-mode confinement regimes.*



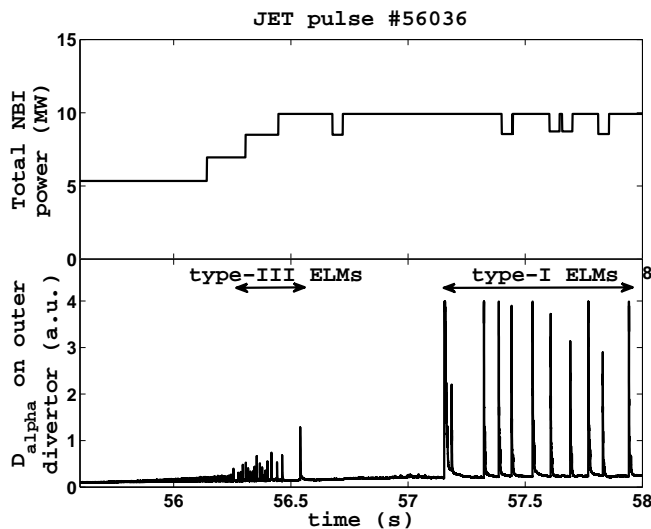
1.6.2 Edge-Localised-Modes

The discovery of the H-mode was closely accompanied by another, less satisfying encounter. Because radial transport is reduced in the pedestal region during H-mode, the pressure gradient increases due to the energy flux arriving from the core plasma. When trying to further increase the heating power after the L-H transition, the edge pressure gradient increases until the MHD stability limit of ballooning modes is reached, resulting in a so-called ELM crash. This crash evacuates the excess of energy through the separatrix, so that the pressure gradient decreases and ballooning modes become stable again. Hence, after the first crash, the edge pressure gradient starts building back up, until the next crash and so on.

Experimentally, this relaxation process is best observed from D_α emissions. This tokamak diagnostic measures the emission of α rays produced when the Deuterium is recycled, ie. when it comes back into the plasma after hitting the divertor. Thus, the D_α signal gives a direct measure of how much plasma hits the divertor, which gives a rough measure of the ELMs size, and a precise measure of their frequency. Experimentally, a typical plasma pulse starts with the L-H transition, which is shortly followed by a series of high-frequency (several hundred Hz) bursts. These small and irregular crashes are usually associated to *type-III* (or resistive) ELMs. If the injected power P_{inj} is further increased, these small bursts disappear and a so-called *ELM-free* H-mode is reached. Then, if P_{inj} is still further increased, large,

quasi-periodic bursts are observed on the D_α signal. These large crashes are called *type-I* (or giant) ELMs. A typical plasma pulse from JET is shown on Fig.12, where the three stages (type-III, ELM-free, type-I) are clearly observed.

Figure 12: D_α emissions during a JET pulse.



1.6.3 Characterization of ELMs

Detailed reviews on ELMs physics can be found in [20,21], but their main characteristics should be summarized here. First it should be noted that ELMs are classified into three types. The *type-II* ELMs are small instabilities, even smaller than type-III ELMs. Their physics is not as well understood as type-I and type-III ELMs, and the damage they cause to PFCs is negligible, so attention should be focused on type-I and type-III ELMs. There is a number of characteristics which are necessary to classify and understand these two types of ELMs. These are the *ELM frequency* f_{ELM} and the duration of an ELM; the amount of density Δn , temperature ΔT and total energy ΔW_{ELM} lost during an instability; the basic MHD properties and geometrical structure of the instabilities; and the way energy is released from the pedestal into the SOL and onto PFCs.

The duration of an ELM does not vary significantly from one type to the other and is usually around $200\mu s$. One of the big differences that distinguishes the two types is their ELM frequency. First, for type-III ELMs, f_{ELM} decreases with increasing injected power P_{inj} , whereas it increases for

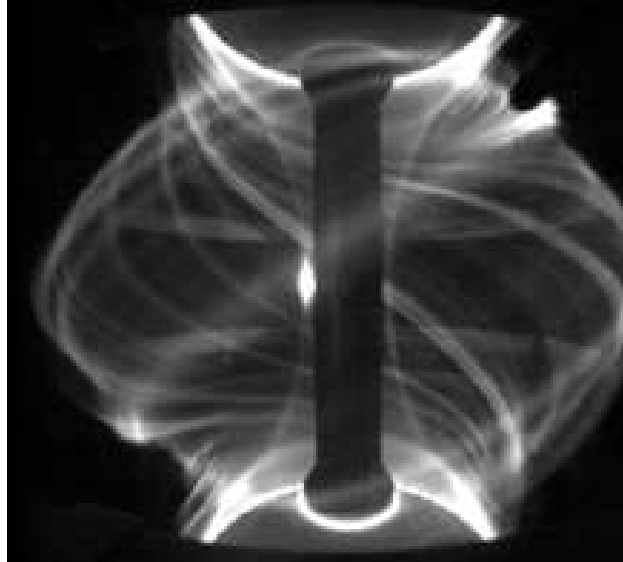
type-I ELMs. Also, f_{ELM} is notably smaller for type-I ELMs (generally below 100Hz) than for type-III ELMs (up to several hundred Hz).

The other distinction between the two ELM types is that the total energy ΔW_{ELM} released by type-I ELMs is much larger than for type-III ELMs, as can be seen from the D_α signal in Fig.12. Type-I ELM losses can reach above 15% of the pedestal energy: big type-I ELMs in the JET tokamak can evacuate up to 1MJ from the plasma. The fact that type-I ELMs release far more energy than type-III ELMs makes them more important to understand. A type-I ELM can also be classified as conductive or convective, whether it evacuates more temperature or density respectively. Conductive ELMs happen to be more violent for PFCs that thus have to support bigger heat fluxes.

Also, one of the main characteristics of ELMs is the fact that they are MHD instabilities with toroidal mode numbers n varying between 8 and 20. As introduced above, ballooning modes are driven by the pressure gradient and kink (peeling) modes are driven by the parallel current density. A theoretical model for ELMs is a mixed *peeling-ballooning* mode interpretation, which is supported by the fact that the steep pedestal pressure gradient in H-mode plasmas results in a strong bootstrap current, so that both terms in the second integral of equation (95) could contribute to the instability. Peeling-ballooning modes are MHD instabilities with high perpendicular wave vectors $k_\perp \rightarrow \infty$, so that the resulting structure of the mode is aligned to the magnetic field. This so-called *filamentation* of the plasma is well observed experimentally - see fast camera picture on Fig.13. These *filaments* are localised in the pedestal (pressure gradient) region, and are ejected through the separatrix into the SOL.

At last, it should be noted that although a non-negligible amount of energy is carried by the filaments across the separatrix, it is known from experimental evidence that these filaments do not carry *all* the energy lost during an ELM. In fact, all variables are affected by the MHD instability - including the magnetic field - so that the perturbation of the magnetic field near the separatrix results in large energy losses, because magnetic field lines connect the pedestal to the divertor targets during this perturbation. And due to fast parallel transport of energy along the field lines, energy is evacuated directly from the pedestal onto the divertor. A consequence of this is that the divertor has to face large heat-loads during ELMs, reaching up to over 100MW.m^{-2} [22].

Figure 13: *Filamentation of the plasma during an ELM.*



1.6.4 Advantages and Disadvantages of ELMs

There are many problematic consequences of ELMs for tokamak machines, but the main one is that PFCs are faced with large heat-fluxes. The resulting damages on PFCs are significant, and extrapolation for machine size predicts that big type-I ELMs in ITER could release up to $20MJ$ on the divertor. No material can resist such heat fluxes, especially on a daily basis. A direct consequence of this is that ELMs represent a limit for tokamak performances in terms of energy confinement.

However, although Edge-Localised Modes present critical inconveniences, they may also be advantageous. In fact, each ELM relaxes the plasma from its impurities, which turns out to be a necessary clean-up when running long pulses, otherwise impurities accumulate in the plasma core, eventually leading to disruption of the plasma (loss of all confinement and plasma current). In other words, ELMs are necessary to achieve continuous H-mode, and so the type-I ELMy H-mode is planned to be the regular operating mode for ITER.

1.6.5 Avoiding and Controlling ELMs

Hence, ITER is planned to run routinely on type-I ELMy H-mode, because this regime is the most successful tokamak scenario. However, the tungsten divertor of ITER will not be able to survive the heat fluxes of large type-I ELMs, so that ELMs need to be controlled in order to avoid those large

ELMs. At present, three techniques have been developed to avoid, mitigate or control ELMs:

- The first option consists in applying *Resonant Magnetic Perturbations* (RMPs) at the plasma edge using non-axisymmetrical coils. The mechanism involved is still not fully understood, but it is suspected that the magnetic perturbations ergodize the magnetic field near the separatrix, and thus increase the radial transport in the pedestal region, allowing for energy to escape from the pedestal into the SOL. This way, the pedestal pressure gradient may be kept under the stability threshold, and thus ELMs are avoided. This control tool has been proved successful on all machines with ITER-like configurations [23-25].
- Another technique relies on the *pellet injection*. This provokes an ELM, even in an ELM-free H-mode. As a result, pellet injection at a regular frequency will enable the ELM frequency to be controlled. If the frequency chosen is higher than the typical ELM frequency of the ELMy H-mode operated, the energy losses per ELM will be diminished. This technique is also very attractive, because it combines the fueling of the plasma (which is essential for long pulses) with the control of ΔW_{ELM} [26,27]. In addition, because the ELMs are not avoided, impurities are still evacuated. The only disadvantage of ELM control by pellet injection is that the pellet injector is a very delicate machine, due to the extremely small size of the pellets and the high speed at which they have to be propelled in order to penetrate the plasma deep enough before being ionized.
- There is a third technique, called *kicks*: A sudden displacement of the magnetic field also provokes an ELM. Here as well, the ELM frequency may be controlled [28,29], and thus the ELM size reduced.

1.7 Understanding ELM Physics

1.7.1 Experimental Observation

In order to understand the ELM instabilities, numerous experimental studies have been undertaken, from which much has been learned. In fact, the understanding of tokamak physics mostly relies on experimental observations. Many phenomena, like the L-H transition, have been well understood experimentally, whereas theoretical models have not always been able to match. Still the best way to refine our understanding of ELM physics is to run more and more plasma shots. In addition, the technological advances regularly

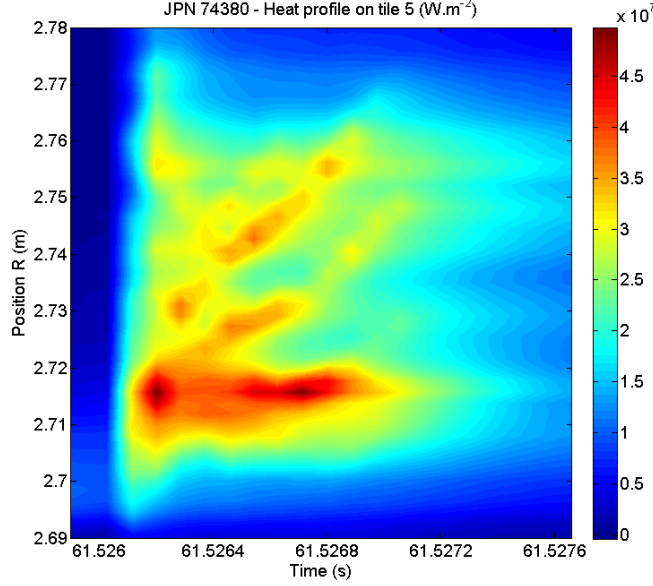
improve diagnostics, so that observations of tokamak plasmas become more and more precise. There are many different diagnostics which can give out useful informations about ELMs:

- As has been stated earlier, the D_α signal gives the signature of the ELM. It also gives a good idea of the ELMs size and a very precise measure of their frequency [30].
- Else, the Thomson Scattering diagnostics give radial profiles of electron density and temperature, which enables one to determine the total energy loss of an ELM, together with its convective/conductive proportions. High Resolution Thomson Scattering (HRTS) may also take radial profiles of filaments, provided they are shot at the right time [31].
- The magnetic measures from Mirnov coils can be used to determine the magnetic activity of the ELMs, and extrapolation may result in a rough estimate of the toroidal mode number evolution during the instability [32].
- An aesthetic diagnostic is the fast camera. It gives a good idea of the geometrical structure of filaments during an ELM, as well as their dynamics (Fig.13) [33].
- By measuring the charge exchange rate at the edge of the plasma, one can obtain a radial profile of the toroidal and poloidal rotation of the plasma in the pedestal region. This is the case of the CXRS diagnostic in JET [34,35]. Although the time resolution of this diagnostic is not fast enough to see the precise evolution of the rotation during an ELM, it gives an idea of the influence of an ELM on the plasma kinetic equilibrium.
- The last but not least diagnostic is the Infra-Red camera. It focuses on the heat fluxes that hit PFCs. They not only give a good measure of heat fluxes, but also catch the structure and dynamics of these fluxes. In sight of the importance of PFCs survival in ITER, this diagnostic is an important tool among ELMs studies (see Fig.14) [22].

1.7.2 Theoretical Interpretation

Observations obtained from tokamak diagnostics would be all but useful if some kind of theoretical interpretation was not done. However, recent phe-

Figure 14: *Heat fluxes on outer divertor as a function of time during an ELM.*



nomenologies like the H-mode or ELMs have not found such a strong theoretical background yet. In the case of ELMs, it was quickly understood that the plasma was subject to an MHD instability. One may develop equation (95) using a *ballooning representation* for the perpendicular displacement vector in toroidal geometry,

$$\begin{aligned}\boldsymbol{\xi}_{\perp} &= \boldsymbol{\eta}_{\perp} e^{iS}, \\ S &= n[-\phi + q(r)(\theta - \theta_0)],\end{aligned}\tag{96}$$

where $q(r) = rB_{\phi}/R_0B_{\theta}$ is the safety factor and θ_0 is some arbitrary integration function. Then, using further mathematical methods, such as the *quasi-mode* assumption for the periodic function $\boldsymbol{\xi}$ (see Connor, Hastie and Taylor, 1979, [36]), one obtains an expression for the integral (95) as a function of the pressure gradient $\alpha = -q^2 R_0 \beta'$ and the shear $s = rq'/q$,

$$\delta W \approx 1.39s^2 - 2.17s\alpha + \alpha^2 - \alpha + 0.5.\tag{97}$$

Setting $\delta W = 0$ to represent marginal stability, one may solve the above equation to obtain a curve that separates stable and unstable regions in the (s, α) diagram (see Fig.15). This analytical approach not only gives a good geometrical perception of the mode structure, but the (s, α) -stability diagram is also in good agreement with experimental observations. However, there are still many questions about ELMs theory fails to answer. In particular, three questions arise:

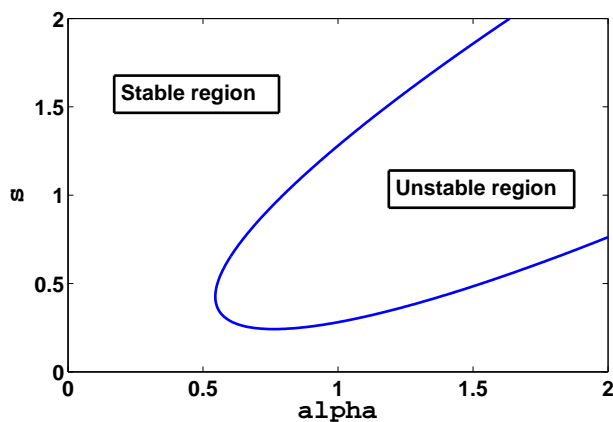


Figure 15: *The stability boundary of the ballooning modes, as a function of the pressure gradient α and the shear s .*

- The first question concerns the difference between type-I and type-III ELMs. Experimentally, the differences between those two ELM-types are well known, in particular for the amount of energy losses and for the relation between heating power and ELM frequency. No theoretical study has yet been able to explain these two crucial points.
- There is also the challenge of understanding how energy is evacuated. In particular, how much energy is carried inside the filaments, and how energy is transported from the pedestal to the divertor. And most of all, what determines the size of an ELM and its conductive/convective properties.
- The third question concerns the filaments themselves. They are aligned to the magnetic field, but is the magnetic field also perturbed, or is it just the pressure? What about the current inside the filaments, their size, their speed...

These questions and issues have already been approached and a good insight to what the answers could be has been given by many theoreticians and experimentalists. However, just like the H-mode, there is yet no theoretical model able to answer all these questions together in concordance with experimental observations. Of course, given the complexity of the instability, together with the surrounding plasma environment and geometry, it would be quite amazing to get such a global model, which is why usually all these questions are approached separately.

1.7.3 Numerical Approach

Another way of studying ELMs physics is by developing numerical codes. There is a wide range of physical models to choose from, and many different numerical schemes. Thanks to the important progress in High-Performance-Computing (HPC) during the last two decades, numerical computation has been able to reproduce many plasma nonlinear phenomena with impressive accuracy. However, there is at present very few numerical codes that can produce ELMs simulations in reasonable agreement with experimental results.

Most of these codes are 3D nonlinear MHD codes. To achieve the same result with a kinetic, or even gyro-kinetic description, is not thinkable at the moment. Even for MHD codes, high-resolution grids are needed to obtain a non-linear evolution of ballooning modes. Kinetic codes need even higher a resolution, in order to solve the small length-scale dynamics of the kinetic equations. This adds to the numerical size of the problem. But both the length-scales and the time-scales of kinetic dynamics are much smaller than MHD scales, and thus become irrelevant in simulations of ELMs, at least at first order. For example, considering time-scales, the dynamics of ELMs is much slower than the gyro-kinetic average time-scale, namely an ELM lasts about $200\mu s$, and the ion gyro-period is about ten thousand times faster.

In the following study the 3D, non-linear MHD code JOREK is used to obtain a better understanding of ELM physics. One of the characteristics of this code, as is presented in the next chapter, is that it considers the X-point geometry, which has been shown experimentally to be an essential ingredient for the H-mode and ELMs. Also, throughout the manuscript, references to and use of linear MHD codes will be made for ELMs stability studies. These are mainly the HELENA and the MISHKA codes.

1.7.4 Combining the Three Methods

Each one of these three methods (experimental observation, theoretical interpretation and prediction, and numerical simulation) may individually bring an important amount of information concerning ELMs, so that a consequent understanding of the instability has been achieved in recent years. But far more insight to ELM physics can be obtained by combining the three approaches.

Effectively, there is always a close interaction between one method and another. For example, one generally uses experimental observation to get a hint of what the instability looks like and how it behaves, in order to build up some analytical theory. Such theories usually bring more information than was observed initially during experiments, so that once verified against

experimental results, these informations bring a further understanding of the plasma instability. Eventually, a theoretical prediction may even be used to achieve new experimental advances and discover new plasma behaviors.

The other common interaction between these three methods is that which involves numerical simulations and theory. In fact, although theoretical understanding often relies on numerical simulations, it only needs experimental observations, and the relation simulation \rightarrow theory is only optional. On the other hand, there is a great need for theoretical advances in order to progress in numerical simulations, the simplest example being that numerical calculations need to solve some physics equations obtained from theory, such as the reduced MHD model.

At last, simulations often rely on experimental observations, not only to check that simulations are actually computing some physical behavior (as opposed to some numerical artifact), but also to obtain a quantitative validation of simulations against experimental results. This way, if it may be shown that simulations are close enough to experiments, the numerical code could be used to understand the behavior of ELM instabilities in present machines, and also give some predictions for future machines such as ITER.

1.8 Thesis Plan

The present manuscript first gives a description of the JOREK code in Chapter 2. In particular, the finite elements composing the X-point grid are defined, and the structure of the X-point grid is described. Then, the implicit time-stepping is presented, and a brief overview of the PastiX library (used for solving the nonlinear system of equation) is given. Following the numerical scheme, the two-fluid reduced MHD model used for simulations is detailed, together with the normalization and the boundary conditions. The last part of the chapter describes how simulations of ballooning modes are obtained, first by building the flux-aligned X-point grid, then simulating a steady kinetic equilibrium, and finally starting the ballooning mode perturbations.

The third chapter focuses on equilibrium poloidal flows in JOREK simulations. The flow is thoroughly studied, first in circular plasmas and then in X-point geometry. In particular, transitions between equilibrium flow structures are simulated, and the effect of parallel velocity on the poloidal flow is presented. Both in the circular and the X-point cases, analytical approaches result in expressions for the poloidal flow, which are compared to simulation results and interpreted. It will be shown that the X-point, together with mass diffusivity, causes density to deviate from flux surfaces near the X-point, which is compensated by parallel velocity and results in a strong

poloidal flow. At last, the effect of the equilibrium poloidal flow on the stability of ballooning modes is described. It will be seen that poloidal flows play an important role in ELMs simulations, especially concerning multiple ELMs simulations.

The last chapter of the manuscript focuses on the simulations of JET and MAST plasmas. A reconstruction of two shots (one for JET, the other for MAST) is obtained, and simulations of ELMs are studied. First, the filamentation of the plasma is studied, giving an analysis of their size, composition and speed. Then divertor heat fluxes are considered, since they may play a major role in ITER, due to the tungsten divertor. A reasonable agreement is obtained with the Infra-Red camera of JET, both concerning the structure of heat fluxes and their dynamics. Finally, the ELM size is studied and its dependency on collisionality presented. Two distinct regimes are identified: a resistive and an ideal regime. For the ideal regime, good agreement with experiments is obtained. Throughout the chapter, particular interest is given to the influence of the poloidal flow on ELMs simulations. It will be seen that, as is first introduced in the second chapter, the poloidal flows do play a major role in ELMs physics. The chapter ends with the simulations of MAST and comparisons to JET simulations and experimental observations. MAST simulations are not taken as far as JET simulations, but they give a good insight to how multi-machine simulations can improve our understanding of ELMs. A global conclusion ends the thesis.

2 The Numerical Tool: JOREK

2.1 Résumé du chapitre

La discrétisation de l'espace et du temps fait partie des caractéristiques qui démarquent JOREK des autres codes MHD. La séparation de l'espace entre une grille dans le plan poloidal, et une représentation de la direction toroidale à l'aide de séries de Fourier, est une technique souvent utilisée dans la simulation numérique des tokamaks. Elle est surtout pratique car elle permet d'isoler les modes résonants, donc si l'on connaît, grâce aux observations expérimentales, les modes dominants lors d'un crash d'ELM, on peut choisir de ne simuler que ces modes. Evidemment, pour obtenir une simulation plus précise et plus détaillée du crash, il est préférable de calculer un nombre maximum d'harmoniques, mais cela n'est pas toujours nécessaire car une simulation avec peu de modes peut déjà contenir les informations physiques principales du crash.

Ensuite, la géométrie poloidale de la grille utilisée est d'une importance primordiale. Les ELMs sont des instabilités qui provoquent une forte augmentation du transport au niveau de la séparatrice, entre les lignes de champs fermées, et les lignes de champs ouvertes, comme l'a été décrit dans le premier chapitre. Il est donc nécessaire d'inclure la partie extérieure du plasma (la Scrape-Off Layer, ou SOL). Les lignes de champs fermées sont discrétisées par une grille polaire, ce qui reste relativement simple. De même, discrétiser les lignes de champs ouvertes n'est pas si compliqué, en soi. La difficulté arrive lorsqu'il faut que les deux domaines s'épousent de manière élégante. La technique utilisée est présentée.

Ajouté à cette géométrie poloidale complète, ce qui contribue à la particularité du code JOREK, ce sont les éléments finis utilisés pour construire la grille: Les *éléments finis de Bezier*. Ces éléments, dits *cubiques*, sont composés de quatre nœuds et de trois vecteurs par nœud. Une base de polynômes d'ordre trois (d'où 'éléments cubiques') est utilisée pour représenter chaque point de l'élément, reposant sur la base vectorielle. Le premier avantage de cette construction, c'est qu'elle assure la continuité des variables et de leurs dérivées, y compris pour les variables spatiales (x,y,z). En d'autres termes, les côtés des éléments ne sont pas droits, mais courbes. Ainsi, puisque la grille est alignée aux surfaces de flux dans le plan poloidal, cette précision apporte à la stabilité numérique. L'autre avantage de cette construction, à l'opposé des *éléments Hamiltoniens*, c'est qu'elle n'impose pas d'identité entre la taille d'un élément et ses éléments voisins. Il est donc possible de raffiner un ou plusieurs éléments (les diviser en deux ou quatre éléments distincts), sans devoir raffiner les éléments voisins. Cette technique d'éléments

finis de Beziere est détaillés dans la première partie de ce chapitre.

Une autre particularité numérique du code JOREK, décrite dans la première partie de ce chapitre, c'est sa discrétisation temporelle, qui est entièrement implicite. Cela a un grand avantage, mais aussi un point faible qu'il faut bien identifier. L'avantage, c'est que ce genre de schéma implicite, comme le Crank-Nicholson par exemple, n'est pas restreint par la taille des éléments de la grille spatiale, comme le sont les schéma explicites, dont le pas de temps dépend directement de la taille minimale des éléments finis. Ainsi, suivant le niveau de non-linéarité de la simulation, et l'amplitude des taux de croissance des modes instables, il est possible d'augmenter le pas de temps, ce qui diminue considérablement la facture d'heure CPUs (le temps de calcul). En revanche, le désavantage de ce genre de schéma, c'est qu'il nécessite de résoudre un système linéaire d'équation sous forme $\mathbf{A} \cdot \mathbf{x} = \mathbf{B}$. Cette calcul peut être plus ou moins couteuse, car elle dépend de la taille de la grille, du nombre de variables, et du nombre d'harmoniques toroidales. Dans les cas les plus extrêmes, la difficulté survient lorsque la mémoire des *clusters* de processeurs utilisés est insuffisante. Néanmoins, comme le schéma de résolution temporelle est parallélisé, les limites de calcul et de taille de grille sont quotidiennement repoussées, grâce aux progrès significatifs acquis ces dernières années en matière de fermes de calculs.

Bien que l'étude achevée dans ce manuscrit soit basée principalement sur des résultats de simulations numériques, la partie analytique reste des plus importante, sous plusieurs points de vue. Notamment, les équations qui sont résolues numériquement doivent être choisies avec précision, afin d'obtenir des résultats physiquement cohérents. Il existe une multitude de modèles MHD, avec chacun ses particularités. Dans le choix d'un modèle, deux critères se démarquent. Tout d'abord, le modèle doit être une bonne représentation de la réalité, avec tous les éléments (termes physiques) nécessaires à une description correcte et fiable du phénomène à étudier, dans le cas présent, les ELMs ou modes de ballonnement. Ensuite, le modèle doit pouvoir être résolu numériquement, donc il ne doit pas être trop complexe, tout en restant fiable à la physique, pour respecter le premier point.

Ainsi est utilisé, pour l'étude qui suit, ce que l'on appelle un modèle de MHD réduite, dont la principale approximation est basée sur la distinction entre la dynamique parallèle et la dynamique perpendiculaire. En effet, comme les particules se déplacent nettement plus rapidement le long des lignes de champs magnétiques que dans la direction perpendiculaire à ces lignes de champs, et que l'amplitude du champ magnétique toroidal se trouve être bien plus élevée que celle du champ poloidal, on peut assumer que la direction perpendiculaire est orthogonale la direction toroidale (et

non à la direction du champ magnétique). Cette réduction a été développée par H.R. Straus [ref.], pour alléger la complexité des simulations numériques. En particulier, cela réduit la non-linéarité du problème, puisque l'équation de moment perpendiculaire se retrouve perpendiculaire à la direction toroidale, qui est constante, et non pas perpendiculaire au champ magnétique, qui peut varier dans le temps.

A partir de ce modèle réduit, certains ingrédients peuvent être ajoutés ou ignorés pour pouvoir enrichir le côté simulations d'un côté, ou simplifier la complexité numérique de l'autre. La résistivité électrique donne l'exemple d'un ingrédient qui ne peut pas être mis à part, car elle joue un rôle majeur dans la stabilité des modes de ballonnements. Un autre ingrédient, qui lui peut très bien être négligé, est la séparation de la température fluide en deux températures distinctes, celle des ions et celle des électrons. Cette option est prise en compte dans la majeure partie de l'étude, car elle permet de comprendre certains phénomènes observés dans les expériences. D'autres modèles, utilisés au sein du groupe travaillant sur JOREK, sont présentés afin de démontrer qu'à chaque étude correspond un modèle bien spécifique. D'autres détails sont traités dans la première partie de ce chapitre, notamment la description des conditions limites, la normalisation choisie, et la représentation sous *forme faible* des équations, simple technique numérique.

Enfin, la troisième et dernière partie de ce chapitre vise à expliquer, de manière simple et compréhensible, les étapes fondamentales d'une simulation d'ELMs. Ceci est fait d'abord pour la partie pratique des simulations, car avant de simuler une instabilité, il faut d'abord obtenir un équilibre stationnaire; mais aussi pour le côté réfléchi d'une simulation, comme choisir les paramètres principaux, choisir le type d'équilibre en fonction du résultat attendu, choisir le nombre d'harmoniques etc... Cela n'est pas décrit afin de servir de manuel d'utilisation, mais plutôt pour expliquer comment se déroule une simulation, ce qui est absolument fondamental lorsque l'on rentre dans les détails numériques, mais aussi (et surtout) dans les détails physiques. Car dans la simulation numérique de phénomènes physiques, le numérique et le physique forment un couple inséparable.

2.2 Discretization

2.2.1 Poloidal and Toroidal Discretization

One of the principal aspects of the numerical scheme of the JOREK code is its spacial discretization, which includes the X-point geometry. As was first explained in Chapter 1, ELMs occur only in X-point plasmas, which justifies the

necessity of having an X-point grid for the present study. There are different ways to discretize the tokamak geometry. One of them consists in separating the toroidal direction ϕ from the poloidal plane (r, θ) . Of course, the most straight-forward discretization would be to produce a three-dimensional grid in the form of a torus, with a polar grid in the poloidal plane, repeated n times by partitioning the toroidal angle from 0 to 2π . However, this quickly generates a huge amount of grid elements, which is restricted by computing memory. Instead, one may produce a two-dimensional grid in the poloidal plane (r, θ) , and represent the toroidal direction using Fourier harmonics. In fact, it is possible to use only a one-dimensional grid in the radial direction r of the poloidal plane, and to represent both the poloidal and toroidal directions θ and ϕ using Fourier discretization, which is numerically more efficient for some physical applications. The constraint of this discretization, however, is that the X-point geometry cannot be treated because periodicity in the θ and ϕ directions is needed, so that this method is not relevant for the present study. By constructing a 2D poloidal grid, one may choose to align the grid elements to the poloidal flux in order to include the complex X-point geometry. Also, having a flux-aligned grid is particularly important due to the fast parallel dynamics of tokamaks. In fact, this is needed for an accurate description of the large parallel conduction of temperature.

The advantage of using a 2D poloidal grid rather than a 3D toroidal grid is that a Fourier representation of the toroidal physics can be used, which significantly reduces the numerical weight of simulations. It also gives the user the choice of toroidal modes to be computed. As has been seen in the previous chapter, the ELMs are toroidal modes with a finite n number. Physically, the most adequate way of representing an ELM would be to simulate all Fourier modes from 0 to ∞ . Then, one expects all modes to be stable, except for a certain number of harmonics, which would be unstable due to the pressure gradient. Of course, to approach this infinity of modes, one would compute all harmonics up to, say n of the order of a few hundreds, but this is numerically too expensive. Instead since it is known, both experimentally and theoretically, that the most unstable ballooning modes have n -values between 5 and 20, one may choose to simulate only those mostly unstable modes. Even if some physical aspects of the instability are lost because of neglecting some range of the Fourier spectrum, the simulations may give a coherent description of the ELMs. Alternatively, the most extreme simulation would consist in modeling only one Fourier mode, which is physically not a complete representation of an ELM instability, but may nevertheless give a good insight to ELMs physics and ballooning modes behaviour. At last, simulations may also be run with only the $n = 0$ toroidal harmonic. This is called axisymmetry, which corresponds to non-static MHD equilibrium, since

no toroidal mode perturbs the plasma. Such simulations may prove useful, as will be seen in the next Chapter, to study equilibrium flows and diffusive transport properties of the MHD equations.

2.2.2 Finite Elements

The description of the 2D poloidal grids used in simulations first requires the definition of the finite elements used for spacial discretization. The grids used in JOREK are constructed with *finite bi-cubic elements* called *Bezier finite elements*, which have the main advantage of respecting the continuity of variables and their derivatives, including the spacial variables (R, Z) of the poloidal plane. The other advantage of Bezier finite elements is that they permit the local refinement of chosen elements, whereas usual *Hermite cubic finite elements* do not. In order to define these finite elements, *Bezier curves* first need to be defined.

BEZIER CURVES

The cubic Bezier curves are defined by two nodes, \mathbf{P}_0 and \mathbf{P}_3 , two *control points*, \mathbf{P}_1 and \mathbf{P}_2 , and the cubic polynomial basis, composed of the *Bernstein cubic polynomials*

$$\begin{aligned} B_0(s) &= (1 - s)^3, \\ B_1(s) &= 3(1 - s)^2s, \\ B_2(s) &= 3(1 - s)s^2, \\ B_3(s) &= s^3, \end{aligned} \tag{98}$$

where $0 \leq s \leq 1$, so that a 3rd order cubic Bezier curve is defined by

$$\mathbf{P}(s) = \sum_{i=0}^3 \mathbf{P}_i B_i(s). \tag{99}$$

Note that the nodes and control points \mathbf{P}_i may be contained in the 2D or 3D space, to define a curve on a plane or in a 3D space. In the present case, since the grid of interest lies in the poloidal plane, these points should lie on a plane, $\mathbf{P}_i = (x, y)_i$. However, one may also add a finite number of other functions to the points, $\mathbf{P}_i = (x, y, \psi_1, \dots, \psi_m)_i$, to represent the variation of each function along the Bezier curve. Here, these functions would be the MHD variables. To simplify further algebra, these m functions will be represented by a single function ψ , so that $\mathbf{P}_i = (x, y, \psi)_i$. Fig.16

Given two Bezier curves defined by the two sets of four points $\{\mathbf{P}_0, \mathbf{P}_1, \mathbf{P}_2, \mathbf{P}_3\}$ and $\{\mathbf{P}'_3, \mathbf{P}_4, \mathbf{P}_5, \mathbf{P}_6\}$, continuity is respected if $\mathbf{P}_3 = \mathbf{P}'_3$. Similarly, for the two curves to have continuous tangents at \mathbf{P}_3 , the condition

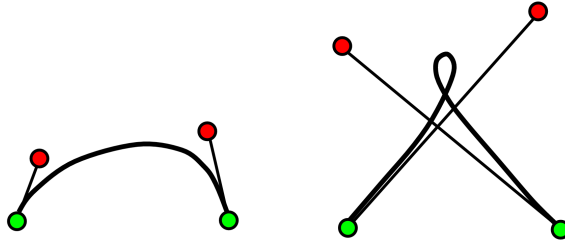


Figure 16: *Two examples of Bezier curves.*

$(\mathbf{P}_2 - \mathbf{P}_3) = \alpha(\mathbf{P}_4 - \mathbf{P}_3)$ should be satisfied. It should be noted that if $\alpha \neq 1$, then continuity of the derivative with respect to the local variable s is not respected. Finite elements with $\alpha = 1$ are called *Hermite finite elements*, which are a special case of Bezier elements. The Hermite elements have the disadvantage of not being locally refinable, because the condition $\alpha = 1$ implies that if one curve ζ is refined (ie. separated into two distinct curves), then the two curves joining ends with ζ need to be refined as well.

2D BEZIER PATCHES

The Bezier formalism can easily be generalized to a surface by multiplying two Bezier curves,

$$\mathbf{P}(s, t) = \sum_{i=0}^3 \sum_{j=0}^3 \mathbf{P}_{i,j} B_i(s) B_j(t), \quad (100)$$

so that there are now 4 *nodes*, and two *control points* plus one *twist point* for each node. Fig.17 shows a Bezier surface with its four nodes, its 8 control points, and its 4 twist points.

The subtle point when dealing with Bezier patches is to express the conditions on continuity in a simple and robust way. Consider the corner $P_{0,0}$ where 4 Bezier patches meet. This collection of patches is defined by 9 points, and the continuity of tangents is most easily described after defining the 8

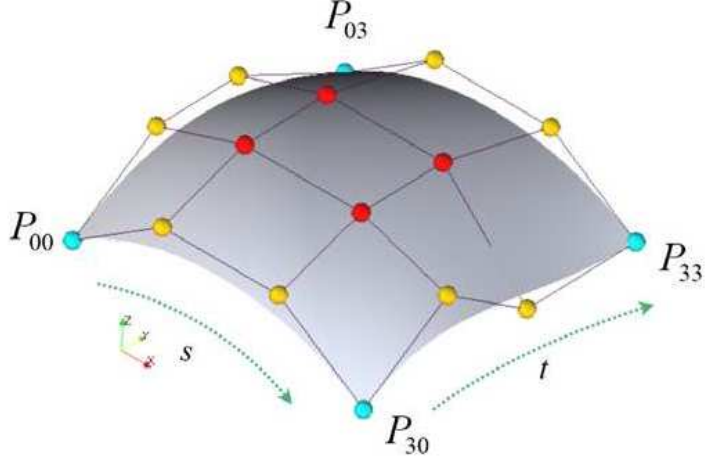


Figure 17: A Bezier surface.

vectors

$$\begin{aligned}
\mathbf{u}_1 &= \mathbf{P}_{1,0} - \mathbf{P}_{0,0}, \\
\mathbf{u}_{-1} &= \mathbf{P}_{-1,0} - \mathbf{P}_{0,0}, \\
\mathbf{v}_1 &= \mathbf{P}_{0,1} - \mathbf{P}_{0,0}, \\
\mathbf{v}_{-1} &= \mathbf{P}_{0,-1} - \mathbf{P}_{0,0}, \\
\mathbf{w}_{1,1} &= \mathbf{P}_{1,1} + \mathbf{P}_{0,0} - \mathbf{P}_{1,0} - \mathbf{P}_{0,1}, \\
\mathbf{w}_{-1,1} &= \mathbf{P}_{-1,1} + \mathbf{P}_{0,0} - \mathbf{P}_{-1,0} - \mathbf{P}_{0,1}, \\
\mathbf{w}_{1,-1} &= \mathbf{P}_{1,-1} + \mathbf{P}_{0,0} - \mathbf{P}_{1,0} - \mathbf{P}_{0,-1}, \\
\mathbf{w}_{-1,-1} &= \mathbf{P}_{-1,-1} + \mathbf{P}_{0,0} - \mathbf{P}_{-1,0} - \mathbf{P}_{0,-1}.
\end{aligned} \tag{101}$$

One may notice that for a given node $\mathbf{P}_{0,0}$, its three control points $\mathbf{P}_{1,0}$, $\mathbf{P}_{0,1}$, $\mathbf{P}_{1,1}$ may be found using the three vectors \mathbf{u}_1 , \mathbf{v}_1 , $\mathbf{w}_{1,1}$, with the relations

$$\begin{aligned}
\mathbf{P}_{1,0} &= \mathbf{P}_{0,0} + \mathbf{u}_1, \\
\mathbf{P}_{0,1} &= \mathbf{P}_{0,0} + \mathbf{v}_1, \\
\mathbf{P}_{1,1} &= \mathbf{P}_{0,0} + \mathbf{u}_1 + \mathbf{v}_1 + \mathbf{w}_{1,1}.
\end{aligned} \tag{102}$$

Now, the continuity of tangents at the corner $\mathbf{P}_{0,0}$, defined by the alignment of the points $\{\mathbf{P}_{-1,0}, \mathbf{P}_{0,0}, \mathbf{P}_{1,0}\}$ and the alignment of the points $\{\mathbf{P}_{0,-1}, \mathbf{P}_{0,0}, \mathbf{P}_{0,1}\}$ is easily expressed by the two conditions

$$\begin{aligned}
\mathbf{u}_1 &= \alpha \mathbf{u}_{-1}, \\
\mathbf{v}_1 &= \beta \mathbf{v}_{-1}.
\end{aligned} \tag{103}$$

In a similar way, one may observe that the continuity at the points $\mathbf{P}_{1,0}$, $\mathbf{P}_{0,1}$, $\mathbf{P}_{-1,0}$ and $\mathbf{P}_{0,-1}$, which is defined by the alignment of the points

$$\begin{aligned} & \{\mathbf{P}_{-1,-1}, \mathbf{P}_{-1,0}, \mathbf{P}_{-1,1}\}, \\ & \{\mathbf{P}_{-1,-1}, \mathbf{P}_{0,-1}, \mathbf{P}_{1,-1}\}, \\ & \{\mathbf{P}_{-1,1}, \mathbf{P}_{0,1}, \mathbf{P}_{1,1}\}, \\ & \{\mathbf{P}_{1,-1}, \mathbf{P}_{1,0}, \mathbf{P}_{1,1}\}, \end{aligned} \tag{104}$$

is satisfied if

$$\begin{aligned} \mathbf{w}_{1,1} &= -\alpha \mathbf{w}_{-1,1}, \\ \mathbf{w}_{1,1} &= -\beta \mathbf{w}_{1,-1}, \\ \mathbf{w}_{1,1} &= \alpha \beta \mathbf{w}_{-1,-1}. \end{aligned} \tag{105}$$

This is the condition adopted here, with the slight modification of definition for the vectors,

$$\begin{aligned} \mathbf{u}_i &= \frac{1}{h_{u,i}} (\mathbf{P}_{i,0} - \mathbf{P}_{0,0}), \\ \mathbf{v}_i &= \frac{1}{h_{v,i}} (\mathbf{P}_{0,i} - \mathbf{P}_{0,0}), \\ \mathbf{w}_{i,j} &= \frac{1}{h_{u,i} h_{v,j}} (\mathbf{P}_{i,j} + \mathbf{P}_{0,0} - \mathbf{P}_{i,0} - \mathbf{P}_{0,j}), \end{aligned} \tag{106}$$

with the scale factors defined by

$$\begin{aligned} h_{u,i} &= \|\mathbf{P}_{i,0} - \mathbf{P}_{0,0}\|, \\ h_{v,i} &= \|\mathbf{P}_{0,i} - \mathbf{P}_{0,0}\|. \end{aligned} \tag{107}$$

With this new definition of the node vectors, the continuity conditions simplify to

$$\begin{aligned} \mathbf{u}_1 &= -\mathbf{u}_{-1}, \\ \mathbf{v}_1 &= -\mathbf{v}_{-1}, \\ \mathbf{w}_{1,1} &= -\mathbf{w}_{-1,1} = -\mathbf{w}_{1,-1} = \mathbf{w}_{-1,-1}. \end{aligned} \tag{108}$$

Hence, the scale factors h_u and h_v are used in the definition of the patch $\mathbf{P}(s, t)$, but the conditions for continuity are the same for every patch, which enables the refinement of any given patch. It is important to notice that the Bezier patches not only include the m variables ψ_1, \dots, ψ_m of the system, but they also include the spacial coordinates (R, Z) of the poloidal plane, so that the Bezier patches are *isoparametric*, which considerably enhances

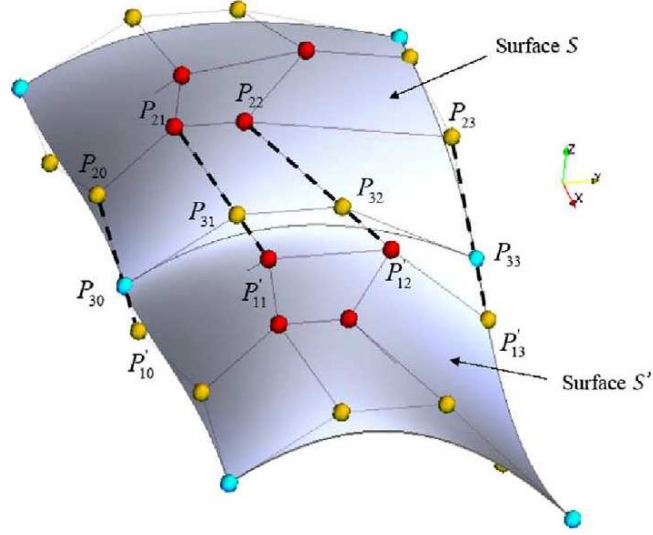


Figure 18: *The continuity requirements for two Bezier surface.*

numerical stability. Fig.18 shows the continuity of two Bezier patches, which can be expressed as the alignment of the neighbouring control points.

FINITE ELEMENTS FORMULATION

Thus, it has been demonstrated that each grid element E is composed of 4 nodes \mathbf{P}_i , $i = 1, \dots, 4$, each of which associated to 3 unit vectors \mathbf{u}_i , \mathbf{v}_i and \mathbf{w}_i , and two scale factors $h_{i,u}$ and $h_{i,v}$. From the relations (102), one may obtain the three control points of the node \mathbf{P}_i using the three vectors \mathbf{u}_i , \mathbf{v}_i and \mathbf{w}_i , together with the scale factors $h_{i,u}$ and $h_{i,v}$. It thus follows that the Bezier formalism (100) may be rearranged to obtain

$$\mathbf{P}(s, t) = \sum_{i=1}^4 \tilde{\mathbf{P}}_i, \quad (109)$$

where the contributions $\tilde{\mathbf{P}}_i$ from each node is given by

$$\begin{aligned}
\tilde{\mathbf{P}}_1 &= (1-s)^2(1-t)^2[(1+2s)(1+2t)\mathbf{P}_1 + 3s(1+2t)h_{1,u}\mathbf{u}_1 \\
&\quad + 3(1+2s)th_{1,v}\mathbf{v}_1 + 9sth_{1,u}h_{1,v}\mathbf{w}_1], \\
\tilde{\mathbf{P}}_2 &= s^2(1-t)^2[(3-2s)(1+2t)\mathbf{P}_2 + 3(1-s)(1+2t)h_{2,u}\mathbf{u}_2 \\
&\quad + 3(3-2s)th_{2,v}\mathbf{v}_2 + 9(1-s)th_{2,u}h_{2,v}\mathbf{w}_2], \\
\tilde{\mathbf{P}}_3 &= s^2t^2[(3-2s)(3-2t)\mathbf{P}_3 + 3(1-s)(3-2t)h_{3,u}\mathbf{u}_3 \\
&\quad + 3(3-2s)(1-t)h_{3,v}\mathbf{v}_3 + 9(1-s)(1-t)h_{3,u}h_{3,v}\mathbf{w}_3], \\
\tilde{\mathbf{P}}_4 &= (1-s)^2t^2[(1+2s)(3-2t)\mathbf{P}_4 + 3s(3-2t)h_{4,u}\mathbf{u}_4 \\
&\quad + 3(1+2s)(1-t)h_{4,v}\mathbf{v}_4 + 9s(1-t)h_{4,u}h_{4,v}\mathbf{w}_4].
\end{aligned} \tag{110}$$

In practice, for numerical elegance, the polynomials composing each $\tilde{\mathbf{P}}_i$ may be reformulated using a new polynomial basis $B_{i,j}$, $j = 1, \dots, 4$, so that any variable ψ , composing the Bezier patch $\mathbf{P}(s, t)$, is constructed in a very general way for a given element, with the recipe

$$\psi(s, t) = \sum_{i=1}^4 \sum_{j=1}^4 \sum_{n=1}^N \psi_{i,j,n} B_{i,j}(s, t) S_{i,j} e^{in\phi}, \tag{111}$$

where $B_{i,j}$ is the new polynomial basis and $S_{i,j}$ represent the element size (the scale factors). The Fourier representation has also been included, with the number of toroidal harmonics N . The $\psi_{i,j,n}$'s are the coefficients composing the variable ψ .

2.2.3 The X-point Grid

There are many different kinds of poloidal discretization. The first kind of discretization used in JOREK is simply a polar grid, where the radial direction r and the poloidal angle θ are partitioned into a chosen number of points. This grid is used to compute Grad-Shafranof equilibria, although polar grids may be used to study other MHD instabilities. In the case of a circular polar grid, the discretization is straight-forward, and the elements are simply aligned to concentric circles. It is often the case, however, that the polar grid is chosen to be non-circular, with a given ellipticity, quadrangularity and triangularity. Fig.19 shows a circular and a non-circular grid. The five parameters used to determine the shape of non-circular grids are the upper and lower triangularities T_u and T_l , the upper and lower quadrangularities Q_u and Q_l , and the ellipticity L , so that a non-circular contour is given by

the parametrization

$$\begin{aligned}
 x &= \cos(\theta + T_u \sin \theta + Q_u \sin 2\theta), & 0 \leq \theta < \pi \\
 &= \cos(\theta + T_l \sin \theta + Q_l \sin 2\theta), & \pi \leq \theta < 2\pi \\
 y &= L \sin \theta.
 \end{aligned} \tag{112}$$

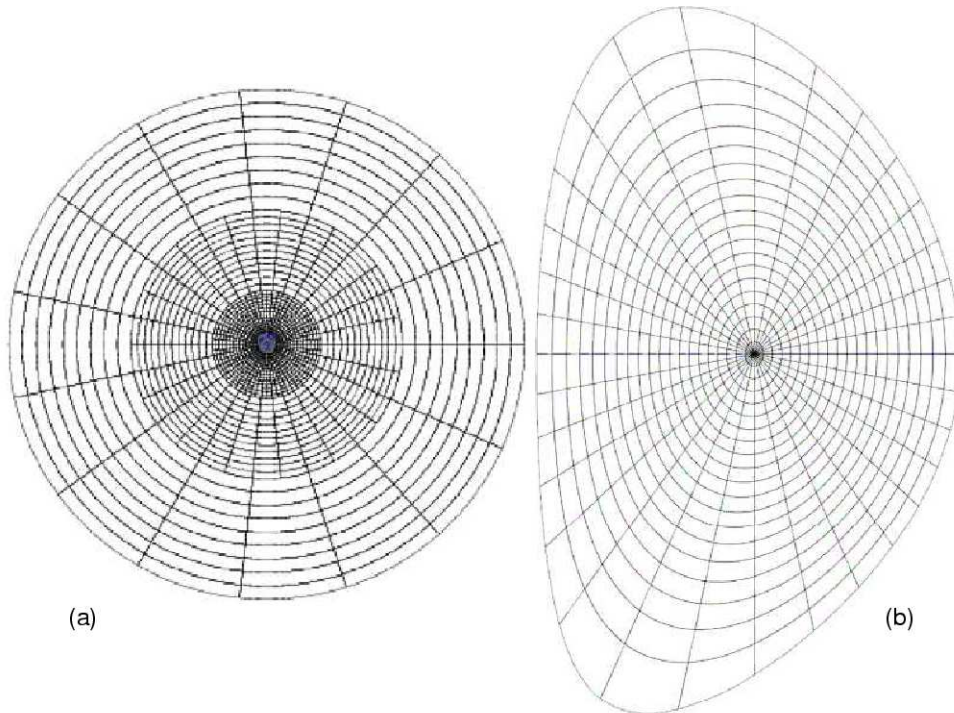


Figure 19: *a). A circular polar grid, with refined elements in the core. b). A non-circular polar grid.*

Once the poloidal flux has been obtained from solving the Grad-Shafranov equation on the polar grid, one may build a new poloidal grid, with elements that are aligned to flux contours. In the case of a circular plasma, it is rather straight-forward and the method is similar to building a non-circular polar grid. However, if the flux ψ calculated from the Grad-Shafranov equation has an X-point, the method is less trivial, and the grid has to be built step by step.

First, the separatrix needs to be identified, as well as the magnetic axis, so that closed and open field lines (ie. core and SOL) may be distinguished. Also, the last open flux surface needs to be chosen; it will be the plasma

boundary, or at least part of it. Then, since the final aim is to obtain a grid aligned to flux surfaces, the radial discretization may be done straight away, by simply taking a chosen set of flux contours, both inside and outside the separatrix.

The poloidal discretization is more complex, however. The poloidal plane is separated into two parts by intersecting it with a horizontal line at the level of the X-point. Thus, the upper part is composed of both closed and open flux contours, and the main idea is that the region inside the separatrix may be treated as a nearly circular region, so that the poloidal discretization is done simply by taking straight lines from the magnetic axis out to the separatrix. Then, for the upper semi-circle, above the magnetic axis, these straight lines are carried out straight to the last open flux surface, thus completing the upper half of the grid. For the region below the magnetic axis, these Bezier curves are carried out into the SOL such that their intersection with the separatrix is located at the same height Z as their intersection with the last open flux surface (the SOL boundary). The lower part of the grid, below the X-point, may also be separated into two SOL regions and the so-called private region. Thus, the discretization method is very similar to that of the upper part of the grid, expect that some last flux surface has to be chosen as a boundary fo the private region, and that two straight lines are chosen for the divertor targets, which forms the two non-flux-aligned boundaries. Fig.20 shows an X-point grid, with weak resolution to exhibit the construction of the grid around the X-point and the junction between closed and open flux surfaces.

2.2.4 Continuity at X-point

The procedure used to build up the X-point grid, explained above, has a particularity at the X-point. One may notice that in an X-point plasma, the magnetic flux ψ has a vanishing gradient $\nabla\psi = 0$ only at two points in the plasma: the magnetic axis, and the X-point. Looking at those points on the grid, it is clear that more than 4 elements meet there. Thus these two points are not standard and have to be dealt with particularly.

For the magnetic axis, a standard method is used, that consists in considering this point not as one node, but as an infinitesimally small circle, so that all nodes on this circle are corners of only two surfaces. This way, the problem of having more than 4 elements meeting at a single node is avoided. In the case of the X-point, the circle method cannot be used because $\nabla\psi$ has a saddle point there, whereas it has a minimum at the magnetic axis. Using the circle method at the X-point would lead to 5-nodes elements, which is not possible. Hence, continuity at the X-point is only partially satisfied for

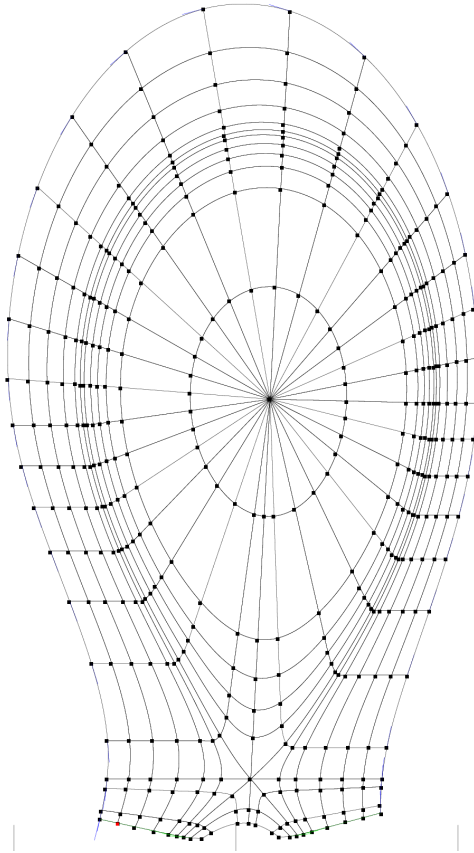


Figure 20: *An X-point grid*

the derivatives, only along the coordinate lines (not across).

2.3 Time Stepping

2.3.1 Implicit Scheme

In addition to the Bezier finite element formulation, a second important particularity of JOREK is that the time-stepping is entirely *implicit*. The resulting advantages and disadvantages ought to be detailed, together with an argumentation that explains why an implicit time-stepping scheme has been chosen, and not an explicit one.

Let us first define the time-stepping used in the code. The *Crank-Nicholson scheme* is most commonly used, although other schemes are available. Consider a system of m equations for m variables y_i , $i = 1, \dots, m$.

$$\frac{\partial y_i}{\partial t} = A_i(y_1, \dots, y_m), \quad (113)$$

where $A_i(y_1, \dots, y_m)$ is a known operator of all variables y_i of the system. Consider this equation at a given time t_n , for which all variables are known (already solved) and given by $y_{i,n}$. In order to solve the equation for a given time step δt , the Crank-Nicholson method evaluates the time derivative $\delta y_i / \delta t$ at the mid-point $t_n + \frac{1}{2}\delta t$. Hence, in order to obtain the next values $y_{i,n+1} = y_i(t_n + \delta t) = y_{i,n} + \delta y_i$, one approximates

$$y_i = \frac{y_{i,n} + y_{i,n+1}}{2} = y_{i,n} + \frac{1}{2}\delta y_i,$$

$$\frac{\partial y_i}{\partial t} = \frac{y_{i,n+1} - y_{i,n}}{\delta t} = \frac{\delta y_i}{\delta t}.$$

Substituting into the above equations, and ignoring all quadratic δ -terms when Taylor expanding, one obtains

$$\begin{aligned} \frac{\delta y_i}{\delta t} &= A_i \left(\left[y_{1,n} + \frac{1}{2}\delta y_1 \right], \dots, \left[y_{m,n} + \frac{1}{2}\delta y_m \right] \right) \\ &= A_{i,n} + \frac{1}{2} \sum_{j=1}^m \left(\frac{\partial A_i}{\partial y_j} \right)_n \delta y_j, \end{aligned}$$

where the subscript F_n means the quantity F should be evaluated at $t = t_n$. Thus, multiplying by δt and rearranging, one obtains a solvable linear system of equations

$$\begin{pmatrix} 1 - \frac{1}{2}\delta t \frac{\partial A_1}{\partial y_1} & -\frac{1}{2}\delta t \frac{\partial A_1}{\partial y_2} & \dots & -\frac{1}{2}\delta t \frac{\partial A_1}{\partial y_m} \\ \frac{1}{2}\delta t \frac{\partial A_2}{\partial y_1} & 1 - \frac{1}{2}\delta t \frac{\partial A_2}{\partial y_2} & \dots & -\frac{1}{2}\delta t \frac{\partial A_2}{\partial y_m} \\ \vdots & \vdots & \vdots & \vdots \\ \frac{1}{2}\delta t \frac{\partial A_m}{\partial y_1} & \frac{1}{2}\delta t \frac{\partial A_m}{\partial y_2} & \dots & 1 - \frac{1}{2}\delta t \frac{\partial A_m}{\partial y_m} \end{pmatrix} \begin{pmatrix} \delta y_1 \\ \delta y_2 \\ \vdots \\ \delta y_m \end{pmatrix} = \delta t \begin{pmatrix} A_{1,n} \\ A_{2,n} \\ \vdots \\ A_{m,n} \end{pmatrix}. \quad (114)$$

The main advantage of the Crank-Nicholson scheme is that the time step is independent from the grid size, as opposed to explicit time-stepping schemes, which are numerically unstable unless the ratio $\delta x / \delta t$ is bigger than any velocity in the system - δx represents the dimension of a grid element. With the Crank-Nicholson scheme, one may use big time steps, even for a highly refined grid, which is advantageous when dealing with systems which are not always highly nonlinear. This way, the only regulation needed for the time step comes from the level of nonlinearity of the system.

The counter point of the Crank-Nicholson time stepping is that the system of equations described in (114) needs to be solved, which becomes difficult if

the order of the matrix multiplying the vector $(\delta y_1, \dots, \delta y_m)$ is large. Thus, one time step is more time consuming than an explicit time-step, which only computes a matrix algebra and does not need to solve a linear system of equations. In practice, each variable coefficient $\psi_{i,j,n}$ from the variable construction (111) needs to be solved, so that a given equation has to be decomposed into $4N$ distinct equations per element (4 Bezier polynomials times N toroidal harmonics). Hence, for a model including m variables solved on a grid of N_e elements, the order of the matrix is $(4mNN_E)^2$. For example, take a system with 4 variables, with a polar grid made of (50 radial times 100 poloidal) = 5000 elements, and 20 toroidal harmonics, the order of the matrix is 2.5×10^{12} . However, and luckily, not all entries are non-zero. The non-zero entries of the matrix are stored in a so-called *sparse matrix*.

2.3.2 PastiX Solver

In order to solve the linear system of equations given by (114), JOREK uses a *library* called *PastiX*, developed by the Bacchus team from INRIA in Bordeaux. PastiX is a parallelized, multi-threaded library that may resolve a linear system of equations $\mathbf{A} \cdot \mathbf{x} = \mathbf{B}$ in two ways. If the matrix \mathbf{A} is symmetric and positive-definite, it either uses the *Cholesky method*, expressing \mathbf{A} as the product of a lower triangular matrix \mathbf{L} with its transpose \mathbf{L}^t , or it uses the *Cholesky-Crout method*, expressing \mathbf{A} as \mathbf{LDL}^t where \mathbf{D} is a diagonal matrix. Otherwise, if the matrix \mathbf{A} is not symmetric, PastiX uses an *LU-decomposition*, \mathbf{U} being an upper triangular matrix.

In most cases with JOREK, the matrix \mathbf{A} is not symmetric, so the *LU-decomposition* is used. The main steps of the procedure used by the PastiX library are

- (i). A reordering of the unknowns in the matrix, in order to reduce the fill-in of the matrices \mathbf{L} and \mathbf{U} induced by the decomposition (the sparse matrix).
- (ii). An estimative factorization of the matrix in order to predict the structure of the factorized matrix.
- (iii). The distribution of matrix blocks among processors (the parallelization).
- (iv). The *LU*-decomposition of the matrix.
- (v). The solving of the system.
- (vi). A convergence refinement of the solution, based on the estimation (ii).

2.3.3 GMRES Convergence and Numerical Limits

The complete system of equations (114) can be solved with the direct solution method using the PastiX library. However this method becomes numerically too expensive for large matrices. In practice, the system is solved using a so-called GMRES iterative solution method. Due to the bad conditioning of the matrix, a good *preconditioner* is essential, so that the submatrix of each Fourier harmonic is solved separately using the PastiX library and the solutions are used as a preconditioner. This amounts to a so-called *block-Jacobi* preconditioner. The GMRES convergence of the solution depends mainly on the non-linearity of the system. If the convergence is not achieved in a relatively small number of steps, the preconditioning of the matrix \mathbf{A} is done at the next time-step, but if convergence is quick, the same preconditioning is used for all time-steps. If convergence is not achieved after a chosen number of time-steps (higher than that required for a new preconditioning), the size of the time-step is divided by two.

The main limit to PastiX is the memory available on the clusters of parallel processors. If the matrix \mathbf{A} is too big, the \mathbf{LU} -decomposition may fail to find enough memory to carry out the simulation. In practice, this usually happens if the size of the grid is too high, so that there is always a limit on the grid size, due to the memory. However, the memory available strongly depends on the clusters, so that some clusters, such as HPC-FF in Juelich, enable simulations with high grid-resolution. More details on simulations with high grid resolution can be found in Chapter 4, where the need to simulate plasmas with parameters close to experimental conditions has pushed the requirements on the grid size.

2.4 The Physical Models

2.4.1 Reduced Resistive MHD

The standard MHD model used in JOREK is the so-called *reduced MHD* model, first introduced in Chapter 1. This model, sometimes called RMHD, is based on the two following approximations,

- (i) The toroidal magnetic field amplitude B_ϕ dominates over the poloidal magnetic field strength B_θ , so that $B_\phi \gg B_\theta$, which is the case for most tokamaks,
- (ii) The toroidal magnetic field strength is constant in time, so that $F(\psi) = F_0$, where $F(\psi) = RB_\phi$ was defined in Chapter 2.2.

Reconsider the set of ideal MHD equations introduced in Chapter 2.1, and repeated here for convenience,

$$\frac{\partial \rho}{\partial t} + \nabla \cdot (\rho \mathbf{v}) = 0, \quad (115)$$

$$\rho \frac{d\mathbf{v}}{dt} = \mathbf{J} \times \mathbf{B} - \nabla p, \quad (116)$$

$$\frac{d}{dt} \left(\frac{p}{\rho^\gamma} \right) = 0, \quad (117)$$

$$\mathbf{E} + \mathbf{v} \times \mathbf{B} = 0, \quad (118)$$

$$\nabla \times \mathbf{E} = -\frac{\partial \mathbf{B}}{\partial t}, \quad (119)$$

$$\nabla \times \mathbf{B} = \mu_0 \mathbf{J}, \quad (120)$$

$$\nabla \cdot \mathbf{B} = 0. \quad (121)$$

Using the two assumptions above, these equations may be reduced to a set of equations that are much less complex to solve numerically. The procedure is derived in Appendix A, and the result directly presented here, together with details on the meanings of the main physical consequences of this reduction. The set of RMHD equations used in JOREK are

$$\frac{\partial \rho}{\partial t} = -\nabla \cdot (\rho \mathbf{v}) + \nabla \cdot (D_\perp \nabla_\perp \rho) + S_\rho, \quad (122)$$

$$R \nabla \cdot \left[R^2 \rho \nabla_\perp \left(\frac{\partial u}{\partial t} \right) \right] = [R^4 \rho W, u] - \frac{1}{2} [R^2 \rho, R^4 |\nabla_\perp u|^2] \\ - [R^2, p] + [\psi, j] - \frac{F_0}{R} \frac{\partial j}{\partial \phi} + \mu R \nabla^2 W, \quad (123)$$

$$\rho F_0^2 \frac{dv_\parallel}{dt} = F_0 \frac{\partial p}{\partial \phi} - R [\psi, p] + \mu_\parallel \nabla^2 v_\parallel. \quad (124)$$

$$\rho \frac{\partial T}{\partial t} = -\rho \mathbf{v} \cdot \nabla T - (\gamma - 1) p \nabla \cdot \mathbf{v} + \nabla \cdot (\kappa_\perp \nabla_\perp T + \kappa_\parallel \nabla_\parallel T) + S_T, \quad (125)$$

$$\frac{\partial \psi}{\partial t} = \eta (j - j_A) + R [\psi, u] - \frac{\partial u}{\partial \phi}, \quad (126)$$

where the *velocity* \mathbf{v} and the *toroidal vorticity* W , as well as the *magnetic field* \mathbf{B} and the *toroidal current* j are defined, respectively, by

$$\mathbf{v} = \mathbf{v}_\parallel + \mathbf{v}_\perp = v_\parallel \mathbf{B} + R^2 \nabla \phi \times \nabla u, \quad (127)$$

$$W = \nabla \phi \cdot (\nabla \times \mathbf{v}_\perp) = \nabla_\perp^2 u, \quad (128)$$

$$\mathbf{B} = F_0 \nabla \phi + \nabla \psi \times \nabla \phi, \quad (129)$$

$$j = -R^2 \nabla \phi \cdot \mathbf{J} = \frac{1}{\mu_0} \Delta^* \psi, \quad (130)$$

where Δ^* is the Grad-Shafranov operator, u is the electric potential, and pressure is defined as $p = \rho T$. Note that the Poisson brackets have been used, with the definition $[a, b] = \mathbf{e}_\phi \cdot (\nabla a \times \nabla b)$.

In order to understand fully the main characteristics of the RMHD model and its differences with the full MHD model, the main approximations done to derive each equations need to be discussed. The approximation that the toroidal magnetic field dominates the poloidal field may be interpreted in terms of parallel and perpendicular length scales L_\parallel and L_\perp , so that it is assumed that the perpendicular velocity has no toroidal component (ie. it lies in the poloidal plane). The other approximation that the toroidal magnetic field be constant in time is also crucial. First, it removes the fast magneto-acoustic waves from the system (compression of the magnetic field), which would be numerically expensive to solve and not necessarily relevant for the application of interest here, which involves slower magneto-acoustic waves (compression of pressure). Hence, variations of the magnetic field are assumed to be principally due to variations of the magnetic potential ψ . Also, the assumption that $\mathbf{B}_\phi = F_0 \nabla \phi$ implies that only the parallel plasma current j appears in the equations. These two assumptions form the base of the RMHD model, and they are reasonable if $B_\phi \gg B_p$. Notably, this reduction of the model permits a much simpler approach of the equations, both analytically and numerically, since \mathbf{v}_\perp is not directly related to ψ anymore (which reduces the nonlinearity of the system), and also because the poloidal component of the current density does not appear in the equations.

The RMHD model was first derived by H.R. Strauss in 1976, with many subsequent modifications [8]. A good reference for the equations used here is his paper from 1997 [9], where it is shown that the model conserves energy at first order in $\epsilon \sim B_p/B_\phi \sim L_\perp/L_\parallel$. This paper is also relevant to the model used here because it includes parallel velocity. Some reduced models did not include \mathbf{v}_\parallel , which may have important consequences for the perpendicular flow \mathbf{v}_\perp , as seen in [Montgomery.1992], and as will be observed in Chapter 4, where a thorough study of equilibria with flow is undertaken.

2.4.2 The Weak Form of Equations

A particularity of the implementation of the RMHD model into the code JOREK is that the equations are solved in *weak form*, which is necessary due to the finite element formulation, since it requires the isolation of each variable component (Fourier and Bezier components). The main advantage of this numerical method is that it reduces all divergence terms $\nabla \cdot \mathbf{V}$, which is particularly useful concerning diffusion terms, because all second derivatives are removed. The weak form consists in multiplying the equation of a given

variable ψ by a *test-function* ψ^* , and integrating the whole over the plasma volume. The test-functions used in JOEREK are simply $T^* = B_{i,j}(s, t)S_{i,j}e^{in\phi}$, as in formulation (111). As an example for the whole model, the temperature equation will be treated. Multiplying (125) with T^* and integrating over the volume V ,

$$\begin{aligned}
& \int \left(\rho T^* \frac{\partial T}{\partial t} \right) dV \\
&= \int \left(-\rho T^* \mathbf{v} \cdot \nabla T - (\gamma - 1)p T^* \nabla \cdot \mathbf{v} + T^* \nabla \cdot (\kappa_{\perp} \nabla_{\perp} T + \kappa_{\parallel} \nabla_{\parallel} T) + T^* S_T \right) \\
&= \int \left(-\rho T^* \mathbf{v} \cdot \nabla T - (\gamma - 1)p T^* \nabla \cdot \mathbf{v} - \nabla T^* \cdot (\kappa_{\perp} \nabla_{\perp} T + \kappa_{\parallel} \nabla_{\parallel} T) + T^* S_T \right), \tag{131}
\end{aligned}$$

where the diffusion term has been integrated by parts, so that a boundary term remains. This term has been ignored here for the following reason. Suppose one evaluates equation (131) on a given grid, and take two adjacent elements E_1 and E_2 with common boundary ζ . Let S_1 and S_2 represent the areas of each element, and let ζ_1 and ζ_2 be their total boundaries, respectively, so that $\zeta \subset \zeta_1$ and $\zeta \subset \zeta_2$. The boundary term arising from integrating by parts the diffusion term over element E_1 is given by

$$\int_{S_1} T^* \nabla \cdot (\kappa \nabla T) dS = - \int_{S_1} \nabla T^* \cdot (\kappa \nabla T) dS + \int_{\zeta_1} T^* \mathbf{n}_1 \cdot (\kappa \nabla T) dl, \tag{132}$$

where \mathbf{n}_1 is the outward normal to the boundary ζ_1 . The same result holds for element E_2 . Now, at the common boundary ζ , we have that $\mathbf{n}_1 = -\mathbf{n}_2$. Hence, the total boundary integral of both elements E_1 and E_2 vanishes on ζ . Generalizing to an element E_0 surrounded by a finite number of elements, it follows that the boundary integral vanishes everywhere on the grid, except at the boundary.

2.4.3 Boundary Conditions

The boundary conditions are separated into three regions: the wall, which is aligned to a flux surface outside the separatrix, the private region, which is also aligned to a flux surface, and the divertor targets, which is the only boundary where ψ is not constant.

For the wall and the private region, Dirichlet boundary conditions are implemented for all variables, but may be changed to Neumann conditions for density and temperature. If Neumann conditions are chosen, so that density and temperature are not fixed, their gradients are assumed to be zero, which

is numerically convenient since the boundary term in (132) simply vanishes. Hence, there is no conductive or diffusive losses at the wall. This approximation is reasonable in the case where the boundary is far from the last closed flux surface, so that density and energy crossing the separatrix are evacuated in the parallel direction through the divertor targets, via convection with v_{\parallel} and conduction with κ_{\parallel} .

For the divertor targets, the boundary conditions implemented for the parallel velocity are the so-called *Bohm* boundary conditions (sometimes called *sheath* or *Mach1* b.c's), arising from sheath currents at the targets [37], forcing v_{\parallel} to the sound speed,

$$v_{\parallel} = \frac{1}{B} \sqrt{\gamma_c T}. \quad (133)$$

Initially, the boundary condition concerns the total energy flux $\Gamma = \beta n T c_s$ at the targets. However, the coefficient β is experimentally and theoretically hard to determine, especially when the energy arriving at the targets varies in time (which is the case during ELMs). Hence, for simplicity, *free outflow* is assumed, so that β is set to 1, leading the boundary condition (133). Also, $\gamma_c = 1$ is assumed, and the diffusive and conductive boundary term arising in (132) is ignored, so that the energy outflow at the divertor targets is convective.

2.4.4 Normalization

A particular normalization is used for the RMHD model implemented in JOREK, using only the total particle density ρ_o and the magnetic permeability μ_o . Hence, the first natural normalizations are done to density and current,

$$\rho \rightarrow \frac{\rho}{\rho_o}, \quad (134)$$

$$j \rightarrow \frac{\mu_o}{j}. \quad (135)$$

In order to be consistent with the equations, the other variables are normalized to

$$t \rightarrow \frac{t}{\sqrt{\rho_o \mu_o}}, \quad (136)$$

$$\mathbf{v} \rightarrow \mathbf{v} \sqrt{\rho_o \mu_o}, \quad (137)$$

$$T \rightarrow T \rho_o \mu_o \quad (138)$$

$$\eta \rightarrow \sqrt{\frac{\rho_o}{\mu_o}} \eta, \quad (139)$$

$$\mu \rightarrow \mu \sqrt{\frac{\mu_o}{\rho_o}}, \quad (140)$$

$$D \rightarrow D \sqrt{\rho_o \mu_o}, \quad (141)$$

$$\kappa \rightarrow \kappa \sqrt{\frac{\mu_o}{\rho_o}}. \quad (142)$$

Note that the only analytical implication of this normalization is that the current is redefined as $j = \Delta^* \psi$ (ie. removed μ_o). Otherwise, the equations do not change. However, the consequence of this normalization is that the time scales are changed to a near Alfvén time scale, so that for a deuterium plasma with $n_o = 6.10^{19} \text{m}^{-3}$ particle density, a unit time scale corresponds to about $0.7 \mu\text{s}$.

In addition, one should be careful when converting simulation variables to experimental values, and inversely. In particular, when dealing with temperature and pressure, one should recall that our definition of pressure is $p = \rho T$, so that if one compares to the usual pressure $p = nT$, we have that temperature is initially normalized with ion mass $m_i = 3, 2.10^{-27} \text{kg}$. Thus, in order to convert a temperature of $T = 12 \text{keV} \approx 1, 9.10^{-15} \text{J}$, the numerical value should not be $\tilde{T} = \mu_o \rho_o T$ but rather $\tilde{T} = \mu_o n_o T = 1, 4.10^{-1}$. This is somewhat confusing, but it turns out to be quite convenient both numerically and analytically, since numerical temperatures are of the order of 10^{-1} to 10^{-2} , and on the other hand, having $p = \rho T$, one does not need to carry around a mass coefficient m_i when manipulating the equations analytically.

2.4.5 Extensions of the Model

The RMHD model presented above and derived in Appendix A is the standard model used for JOREK ELMs simulations. There exist other models, already exploited or under development, that are worth discussing. The three models of interest are (i). the two-fluid model, including distinct ion and electron temperatures, (ii). the full MHD model, where the resistive

MHD equations are not reduced, and (iii). the model for massive injection of neutral gas, which involves a new variable (the neutral density).

The Two-Fluid Model

There is a special closure of the MHD equations, which enables one to replace the single-fluid temperature T by two separate temperatures for ions and electrons, T_i and T_e respectively. Usually, in order to derive the single-fluid MHD equations, one has to make the following assumptions to combine ions and electrons physics,

$$n_i = n_e \text{ and } \rho = n_i m_i + n_e m_e \approx n_i m_i, \quad (143)$$

$$\mathbf{v}_i = \mathbf{v}, \quad (144)$$

$$\mathbf{v}_e = \mathbf{v} - \frac{1}{en} \mathbf{J}, \quad (145)$$

$$T_i = T_e = \frac{1}{2}T, \text{ and } T = T_i + T_e. \quad (146)$$

Each of these assumptions needs comment. The first approximation is simply due to quasi-neutrality, which holds for the two-fluid model as well. And since $m_e \ll m_i$, the total mass density is defined as $\rho = m_i n$. The assumption on plasma velocity also holds in the two-fluid case, and a single equation is obtained for \mathbf{v} . The two initial equations are given by [7],

$$nm_\alpha \frac{d\mathbf{v}_\alpha}{dt} - nq_\alpha (\mathbf{E} + \mathbf{v}_\alpha \times \mathbf{B}) + \nabla p_\alpha = \mathbf{R}_\alpha, \text{ with } \alpha = i, e. \quad (147)$$

Then, adding the ion and electron equations, the collision term \mathbf{R}_α cancels out, since $\mathbf{R}_i = -\mathbf{R}_e$, and so does the \mathbf{E} term. The resulting velocity equation is obtained by assuming $m_e \ll m_i$, so that the convective derivative of plasma velocity corresponds to that of ions. This assumption is reasonable since the ions have a much higher momentum than electrons because of their higher mass. The velocity equation thus reads

$$\rho \frac{d\mathbf{v}}{dt} = \mathbf{J} \times \mathbf{B} - \nabla p, \quad (148)$$

with total pressure $p = \rho(T_i + T_e)$.

Now, the last assumption (146) is true for some special regimes of tokamak operation. There are many cases however, and in particular regimes of most interest for fusion purpose, where $T_i \neq T_e$. For example, one of the most promising tokamak scenarios involves strong ion cyclotron heating, since the fusion of deuterium and tritium ions needs high T_i but not necessarily high T_e . In addition, it has been observed experimentally that ion and electron

physics are very different due to the mass difference. Nevertheless, this approximation is reasonable considering global plasma properties. Thus, for single-fluid models, temperature is defined as $T = T_i + T_e$, and both temperature equations are combined to form one. It should be noted that the current terms, arising from the electron velocity in the electron temperature equation, are typically ignored in single-fluid models. If the temperatures are not combined, the two equations are

$$\begin{aligned} \rho \frac{\partial T_i}{\partial t} &= -\rho \mathbf{v}_i \cdot \nabla T_i - (\gamma - 1) \rho T_i \nabla \cdot \mathbf{v}_i \\ &+ \nabla \cdot \left(3.9 \frac{\rho T_i \tau_i}{m_i} \nabla_{\parallel} T_i \right) + \frac{3m_e}{m_i} \frac{\rho}{\tau_e} (T_e - T_i), \end{aligned} \quad (149)$$

$$\begin{aligned} \rho \frac{\partial T_e}{\partial t} &= -\rho \mathbf{v}_e \cdot \nabla T_e - (\gamma - 1) \rho T_e \nabla \cdot \mathbf{v}_e \\ &+ \nabla \cdot \left(3.16 \frac{\rho T_e \tau_e}{m_e} \nabla_{\parallel} T_e \right) - \frac{3m_e}{m_i} \frac{\rho}{\tau_e} (T_e - T_i), \end{aligned} \quad (150)$$

where the collision times are given by

$$\tau_e = k \frac{T_e^{\frac{3}{2}}}{\rho}, \quad (151)$$

$$\tau_i = k \left(\frac{2m_i}{m_e} \right)^{\frac{1}{2}} \frac{T_i^{\frac{3}{2}}}{\rho}, \quad (152)$$

$$k \approx 1.1 \times 10^{12}. \quad (153)$$

Note that the factor k has been calculated from the theoretical value [ref],

$$k = \frac{3(2\pi)^{\frac{3}{2}} \epsilon_o^2 m_i m_e^{\frac{1}{2}}}{e^4 \lambda},$$

with Coulomb logarithm $\lambda = 16$, and assuming the ion charge is $z = 1$. Introducing the definition of plasma velocity $\mathbf{v}_e = \mathbf{v}_i - \frac{m_i \mathbf{J}}{e\rho}$ and $\mathbf{v}_i \approx \mathbf{v}$, and normalizing with ρ_o and μ_o ,

$$\begin{aligned} \rho \frac{\partial T_i}{\partial t} &= -\rho \mathbf{v} \cdot \nabla T_i - (\gamma - 1) \rho T_i \nabla \cdot \mathbf{v} \\ &+ \nabla \cdot (\kappa_{i,\parallel} \nabla_{\parallel} T_i) + Q (T_e - T_i) + S_i \end{aligned} \quad (154)$$

$$\begin{aligned} \rho \frac{\partial T_e}{\partial t} &= -\rho \mathbf{v} \cdot \nabla T_e - (\gamma - 1) \rho T_e \nabla \cdot \mathbf{v} \\ &+ \sigma \left(\vec{J} \cdot \nabla T_e - (\gamma - 1) \frac{T_e}{\rho} \vec{J} \cdot \nabla \rho \right) \\ &+ \nabla \cdot (\kappa_{e,\parallel} \nabla_{\parallel} T_e) - Q (T_e - T_i) + S_e \end{aligned} \quad (155)$$

where the parallel thermal conductivities $\kappa_{i,\parallel}$ and $\kappa_{e,\parallel}$, the heat transfer factor Q , and the coefficient σ for current effects are given respectively by

$$\kappa_{i,\parallel} = k_i T_i^{\frac{5}{2}}, \quad k_i \approx 1, 23.10^6 \quad (156)$$

$$\kappa_{e,\parallel} = k_e T_e^{\frac{5}{2}}, \quad k_e \approx 4, 25.10^7 \quad (157)$$

$$Q = \bar{Q} \frac{\rho^2}{T_e^{\frac{3}{2}}}, \quad \bar{Q} \approx 2, 23.10^{-7} \quad (158)$$

$$\sigma \approx 4, 81.10^{-2}. \quad (159)$$

The main advantage of the Two-Fluid model over the usual RMHD is that it may be used to study ion and electron energy transport. The principal difference between the two temperatures is the parallel thermal conductivity. Because of their lower mass, electrons are transported much faster in the parallel direction, by a factor $\frac{3.16}{3.9} \sqrt{\frac{m_i}{2m_e}} \approx 34, 5$. This has important and interesting consequences in ELMs simulations, concerning the amount of ion and electron energy reaching the divertor targets and the vessel walls. More details on Two-Fluid simulations will be given in Chapter 4. Notably, since the effect of interest sought here is the difference of parallel conduction for T_i and T_e , the current terms in the equation for T_e are ignored in the simulations presented throughout this study, although they should be included in future for more precise comparisons with experiments. In addition, it should be noted that the normalization used here implies that the coefficients k_j , appearing in the parallel conductivities $\kappa_{\parallel,j} = k_j T_j^{\frac{5}{2}}$, depends on the plasma density as $k_j \sim \rho_o^{-3}$. This is an important aspect of the normalization, and it will be used later in Chapter 4 for collisionality scans, where the plasma density ρ_o is varied.

The Full MHD Model

The RMHD equations introduced above have the great advantage of being easy to manipulate, and less nonlinear than the initial (full) MHD model. In particular, the assumption that the toroidal component of \mathbf{B} be constant in time eliminates the fast compressional magneto-acoustic waves, which are believed not to influence the slower magneto-acoustic waves. This full MHD model should help verify or disprove this assumption. The two other approximations of RMHD, based on the assumption that toroidal length scales dominate poloidal length scales (if $B_\phi \gg B_p$) and that the toroidal magnetic field is constant in time and ψ -independent, imply that the poloidal plasma current does not appear in the equations, and that the plasma perpendicular velocity lies in the poloidal plane. In other words, this is the approximation

that the projection of Maxwell's equations in the parallel direction \mathbf{B} and in the perpendicular direction $\times\mathbf{B}$ is equivalent to their projection in the toroidal direction $\nabla\phi$ and the poloidal plane $\times\nabla\phi$, respectively. Whether this assumption has an influence on the global structure of plasma velocity and current, and may in turn influence ELMs physics, could be verified by comparing the full MHD model with the reduced model.

The MGI Model

Massive gas injections are used to slow down or stop plasma disruptions. This technique is currently being studied and will certainly be needed for large scale tokamaks such as ITER or DEMO. Disruptions are most dangerous; they can damage the vacuum vessel, because during so-called Vertical Displacement Events (VDE), the current displacement toward the wall can cause currents to run through the vessel, inducing titanic material forces (equivalent to several tons) [38,39]. This model was developed to try and understand the physics of massive injections of neutral gases. Unlike the two-fluid model, this not only introduces a new equation for the new variable ρ_n , but also new boundary conditions at the targets. The main physical phenomena to be introduced are the ionization rate of neutral particles σ_{ion} and the charge exchange rate σ_{xs} . These coefficients depend on temperature, and they enter the neutral diffusion coefficient $D_n = D_n(\rho, \sigma_{ion}, \sigma_{xs}) = D_n(\rho, T)$, and the density equations. It follows that the momentum and temperature equations will also be affected, and not only by ionization and charge exchange. In fact, in order to obtain equations for \mathbf{v} and T , one introduces the continuity equation into the momentum and the energy equations to get rid of the $\partial_t\rho$ term, which is a common technique used in fluid dynamics. In general, fluid equations are derived in the ideal case, without diffusions and sources, so that in this procedure, the continuity equation introduced in the momentum and the energy equations is simply $\partial_t\rho = -\nabla \cdot (\rho\mathbf{v})$. This is not the case here, and when substitution of the continuity equation is done into the momentum and the energy equations, all terms in the continuity equation should be taken into account. The boundary conditions are also specific to neutrals, with outward density flux at the targets given by

$$\mathbf{n} \cdot (D_n \nabla \rho_n) = \mathbf{n} \cdot (\rho \mathbf{v} + D \nabla \rho). \quad (160)$$

In other words, the plasma particles hitting the divertor targets are reflected as neutrals into the plasma, to be ionized again.

2.5 ELMs Simulations

2.5.1 Running JOREK

There are three important steps when running JOREK: 1). Building the grid, 2). Obtaining a steady or at least quasi-steady kinetic equilibrium, and 3). Launching the Fourier harmonic perturbations. These three steps are all more or less delicate, and crucial to understand how simulations of ELMs are produced, so the basic procedures are explained.

Building the Grid

As seen in the previous chapter, the Grad-Shafranov equation may be solved for ψ , given that the pressure $p(\psi)$ and the function $F(\psi)$ are known, together with boundary conditions for ψ . The pressure profile is given by temperature and density independently with the function

$$\begin{aligned}
 T &= (T_0 - T_1)P(\psi_n)f(\psi_n) + T_1, \quad \text{with} \\
 P(\psi_n) &= 1 + T_{c1}\psi_n + T_{c2}\psi_n^2 + T_{c3}\psi_n^3, \\
 f(\psi_n) &= \frac{1}{2} - \frac{1}{2} \tanh\left(\frac{\psi_n - T_{c5}}{T_{c4}}\right), \\
 \psi_n &= \frac{\psi - \psi_{axis}}{\psi_{xpoint} - \psi_{axis}},
 \end{aligned} \tag{161}$$

which is more or less a *tanh* function, with pedestal at a distance $1 - T_{c5}$ from the separatrix, and width T_{c4} . The coefficients T_0 , T_1 and T_{ci} determine the shape of the plasma pressure profile. The same function is used for density, and the FF' profile is given by

$$\begin{aligned}
 FF' &= [(F_0 - F_1)P_2(\psi_n) + g(\psi_n)]f_2(\psi_n) + F_1, \\
 P_2(\psi_n) &= 1 + F_{c1}\psi_n + F_{c2}\psi_n^2 + F_{c3}\psi_n^3, \\
 f_2(\psi_n) &= \frac{1}{2} - \frac{1}{2} \tanh\left(\frac{\psi_n - F_{c5}}{F_{c4}}\right), \\
 g(\psi_n) &= \frac{1}{2}F_{c6} \frac{\partial}{\partial \psi_n} \left[\tanh\left(\frac{\psi_n - F_7}{F_{c8}}\right) \right].
 \end{aligned} \tag{162}$$

which is the same function as for temperature and density, except for a perturbation $g(\psi_n)$ to represent the bootstrap current. The constant F_0 is the strength of the toroidal magnetic field.

The last ingredient needed to solve the Grad-Shafranov equilibrium is the flux contour. This is chosen in two ways: the geometrical form of the poloidal contour, and the value of ψ on this contour. For nearly circular plasmas, the

value of ψ may be constant on the contour, but for X-point plasmas, it is more subtle. The form of the contour is determined by the parametrization

$$\begin{aligned} R &= R_geo + a \cos(\theta + \text{tria_u} \cdot \sin \theta + \text{quad_u} \cdot \sin 2\theta), \quad 0 \leq \theta < \pi \\ R &= R_geo + a \cos(\theta + \text{tria_l} \cdot \sin \theta + \text{quad_l} \cdot \sin 2\theta), \quad \pi \leq \theta < 2\pi \\ Z &= Z_geo + a \cdot \text{ellip} \cdot \sin \theta, \end{aligned} \quad (163)$$

where the upper and lower triangularities `tria_u` and `tria_l`, and quadrangularities `quad_u` and `quad_l`, as well as the plasma ellipticity `ellip` may be varied to modify the final geometry of the flux ψ solved from the Grad-Shafranov equation. `a` is the contour radius, and `R_geo` and `Z_geo` determine the centre position of the contour. The value of ψ on this contour is determined by the function

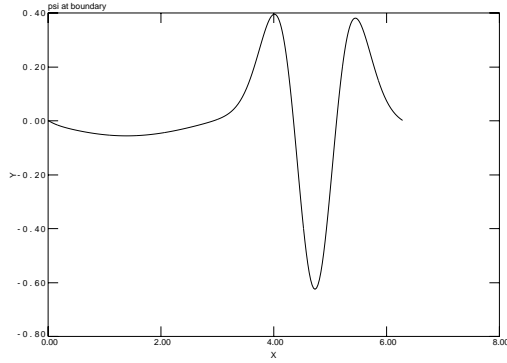
$$\begin{aligned} \psi_{bnd} = & -X_{\text{shift}} \cdot \sin \theta + X_{\text{left}} \cdot \cos \theta \\ & + X_{\text{ampl}} \left[-1.0 + \left(\frac{X_{\text{width}}(\theta - X_{\text{theta}})}{X_{\text{sig}}} \right)^2 \right] \exp \left[- \left(\frac{\theta - X_{\text{theta}}}{X_{\text{sig}}} \right)^2 \right], \end{aligned} \quad (164)$$

where `X_shift` and `X_left` are used respectively for horizontal and vertical shifts of the plasma, `X_theta` is the position of the X-point perturbation, `X_ampl` its amplitude, `X_width` its width, and `X_sig` determines the width of each leg of the perturbation, as shown in Fig.21a.

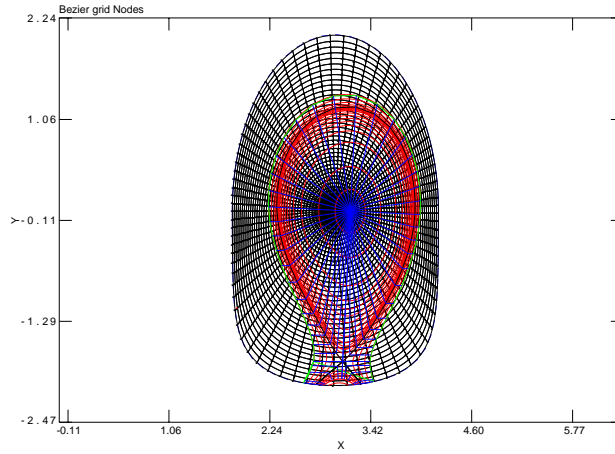
Having all the ingredients to solve the Grad-Shafranov equation, the last thing to choose is the grid size. There are two grids to be chosen. The first grid is the polar grid to solve the Grad-Shafranov equilibrium, and the second grid is the X-point grid determined by (`n_flux`, `n_tht`, `n_open`, `n_leg`, `n_private`). There are other grid parameters to determine the distribution of grid points, in order to increase the grid resolution in chosen regions of the plasma (typically the regions near the separatrix and the X-point). These parameters determine the widths of Gaussian functions that are integrated in order to determine the distribution of nodes. Also, some more parameters determine the size of the open and private regions, ie. the distance of the boundary flux surface from the separatrix. Fig.21b features a non-circular polar grid, on which the X-point flux contours resulting from solving the Grad-Shafranov equation are shown.

Running the Equilibrium

Once the grid has been built, one should run a simulation first with only the $n = 0$ Fourier harmonic, in order to obtain a quasi-steady state. There are different kinds of steady or quasi-steady states. The most correct steady



(a)



(b)

Figure 21: *a). The flux ψ on the domain boundary as a function of the angle θ . b). The polar grid inside the ψ -boundary, on which is calculated the X-point Grad-Shafranov equilibrium, as the red ψ -contours show.*

state equilibrium would be attained after running the simulation for a long time, without any harmonic, until the pressure gradient has adapted to the diffusion profiles. The time-scales needed to reach such an equilibrium are of the order of $\tau \sim a^2 D_{\perp}^{-1}$. For diffusivities of interest ($\sim 10^{-7}$ to 10^{-6}), these time-scales are too long.

Instead, there is another quasi-steady state, which requires far less simulation time. This is obtained once the plasma velocity becomes steady. The perpendicular velocity may become steady rather quickly (a few Alfvén

times, thus a few time steps), because the electric potential u adapts quickly to the pressure profile. The parallel velocity however, requires longer than that, because the Mach1 boundary conditions at the divertor targets need to diffuse into the plasma, with a sonic time-scale. Typically, one requires between 500 and 1000 Alfvén times, depending on μ_{\parallel} .

The other important thing is that in order to diffuse from the targets into the plasma, the first time-steps need to be small, because of the strong gradient ∇v_{\parallel} at the targets. Typically, equilibria are obtained by running 20 time-steps of 10^{-3} , 20 time-steps of 10^{-2} , 100 time-steps of 10^{-1} , 100 time-steps of 1, and 100 time-steps of 10 (in normalized units).

Launching the Ballooning Modes

The Fourier harmonics are perturbed for the electric potential, with a very low amplitude (10^{-30}). The equations are first evaluated on a grid in the toroidal direction, and then Fourier transformed using the *Fast Fourier Transform* (FFT). At first, some numerical noise appears, with also very low amplitude, which does not affect the plasma equilibrium. If the equilibrium is ballooning unstable (ie. high pedestal pressure gradients), the noise will be overtaken by a mode, which will cause an ELM crash.

2.5.2 The Choice of Equilibrium and Harmonics

The equilibrium from which harmonics are launched is crucially important regarding the ballooning mode. The main reason for this is that although one may choose a pressure profile which is ideally unstable to ballooning modes at the beginning of the simulation, for the Grad-Shafranov equilibrium, one has to check that these profiles do not vary too much when running the equilibrium. For example, if the perpendicular diffusivities are not consistent with the initial profile, the pressure gradient at the pedestal may fall considerably, in which case the ballooning mode may become stable.

The other aspect of equilibrium regarding the ballooning modes is that the equilibrium plasma velocity may have a strong influence on ballooning modes stability, both regarding the linear growth rates and the nonlinear evolution of the modes. A thorough overview of the influence of poloidal rotation on ballooning modes is given in the next Chapter.

Concerning the number of harmonics, it has been seen that the size of the matrix was linear in N^2 , so that the memory and CPU limit is reached rather quickly. It is possible to use a periodic representation of the toroidal direction. Using this method, one can simulate a single ballooning mode number ($n=8$, say) if only one non-zero Fourier harmonic is simulated, with a chosen periodicity (8 in that case). Alternatively, one can simulate a range

of modes if many Fourier harmonics are simulated with a given periodicity. For example, with $N = 5$ and a periodicity of 5, the modes simulated will be 5, 10, 15, 20, 25.

Simulations of a single ballooning mode are extensively used for two reasons. First of all, it saves considerable computing time, so that far more simulations may be run, leading to more quantitative studies. The other reason is that in a simulation with many modes, it is not clear which mode should be most unstable. When launching harmonics, with perturbation amplitudes around 10^{-30} , numerical noise is observed before the ballooning modes start to grow. Now, it cannot be guaranteed that the first mode to grow is the most unstable. It may well be the case that the numerical noise randomly favors one mode rather than the others. In addition, it is often the case that this first mode will produce an ELM crash, so that by the time the other modes have grown, the plasma has become stable again, and the other modes will not grow strong enough to perturb the plasma. In such a situation, it becomes highly preferable to simulate a single ballooning mode, which in the end gives approximately the same result, and has a far smaller computing cost.

2.5.3 The Main Plasma Parameters

All non-ideal MHD parameters (diffusive parameters) have a strong influence on simulations. The resistivity η , the parallel and perpendicular viscosities μ_{\parallel} and μ , and the parallel thermal conductivities for ions and electrons, $\kappa_{i,\parallel}$ and $\kappa_{e,\parallel}$, should be chosen as close to experimental or theoretical values as the numerical limits allow. The perpendicular mass diffusivity and thermal conductivity D_{\perp} and κ_{\perp} are particular, because they are used to obtain a transport barrier. Since no numerical or theoretical model is yet able to provide a method for transport barrier coefficients, the H-mode pedestal region, where perpendicular turbulent transport is weak, is represented by a well in the perpendicular diffusivity and thermal conductivity. Thus, a typical profile for D_{\perp} , shown in Fig.22a, is obtained via the function

$$D_{\perp} = D_1 \left[1 - D_2 + D_2 \left(\frac{1}{2} - \frac{1}{2} \tanh \left(\frac{\psi_n - D_5}{D_4} \right) \right) \right] + D_6 \left(\frac{1}{2} - \frac{1}{2} \tanh \left(\frac{-\psi_n + D_5 + D_3}{D_4} \right) \right) \quad (165)$$

with coefficients D_i to be chosen according to the density profile prescribed in (161). The same is done for κ_{\perp} . Thus, D_1 gives the amplitude of D_{\perp} in the plasma core, D_2 gives the depth of the well, D_5 is the positions of the tanh fall and D_4 the width of the tanh gradient. The second function with amplitude

D_6 is used if one wants D_\perp to come back up in the SOL, giving a well width D_3 .

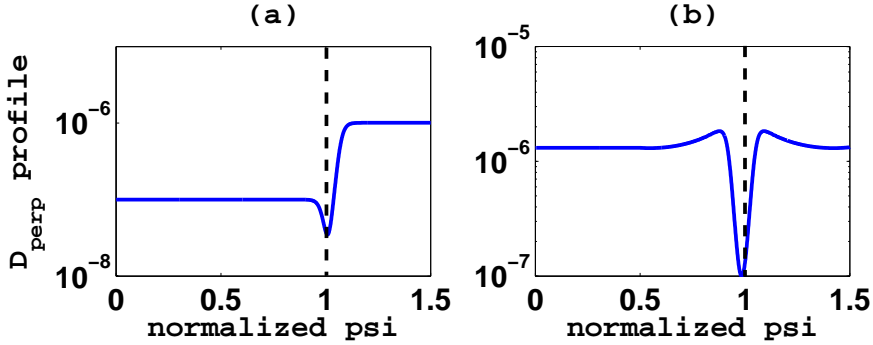


Figure 22: *a). A hand-made D_\perp profile with a well at the pedestal and a higher diffusivity in the SOL. b). A D_\perp profile coherent with the pressure gradient, to keep a pedestal pressure gradient constant in time.*

An alternative to these hand-made profiles has also been implemented in the code, so that the perpendicular diffusion profiles depend on the density and temperature gradients. Namely, these profiles are taken to be $D_\perp \sim (\nabla\rho)^{-1}$ and $\kappa_\perp \sim (\nabla T)^{-1}$, at least in the pedestal region, although a symmetry is applied at the middle of the pedestal, to ensure that the profiles will not jump to extremely high values in the SOL, where the density and temperature gradients are almost zero. Also, in the core region of the plasma, the profiles are set to constants, because at the magnetic axis, the pressure gradient is also zero. Such a profile ensures that the perpendicular diffusive flux $D_\perp \nabla\rho$ remains constant, so that the density and temperature profiles are constant in time, which is quite convenient when one wants to ensure a given ideal MHD stability of pressure gradients in the pedestal, since it is crucial for the study of ballooning modes (see Chapter 4). Fig. 22b shows this profile.

There are also numerical (*hyper-*) diffusivities for all equations. These are coefficients of fourth order derivatives $\Delta(\Delta\psi)$, and they are either set to zero, or set at a value at least 10^{-3} times the corresponding diffusivity amplitude. One should be careful to keep these hyper-diffusivities low enough, so as not to influence the stability of ballooning modes or their non-linear behaviours. At last, heating sources for ion and electron temperatures, as well as the density source, may be used with given radial profiles (usually only in the core plasma, and zero otherwise).

2.6 Summary

The spacial and temporal discretization used in JOREK has been described. The bi-cubic Bezier finite elements composing the X-point grid were defined, together with their advantageous properties, and the technique used to construct the X-point was presented. Also, the implicit time-stepping and the PastiX solver have been introduced. They form one of the pillars of JOREK, since implicit time stepping enables the simulation of a wide range of MHD instabilities, with different time-scales. In addition to the numerical scheme, the two-fluid reduced MHD model used for simulations was discussed, and the equations implemented in the code were detailed (a derivation of the equations is found in the Appendix A). In particular, the correct (Braginskii) parallel thermal conductivity is used, respecting the difference between ion and electron thermal conductivities. The last part of the chapter presented how simulations of ballooning modes are obtained, first by building the flux-aligned X-point grid, then simulating a steady kinetic equilibrium, and finally starting the ballooning mode perturbations. This introduction to ELMs simulations is crucial, since it is needed to understand what the resulting simulations may produce, and what the important features of ELMs simulations are.

3 The Influence of the Poloidal Flow in Simulations of ELMs

3.1 Résumé du chapitre

Il est souvent observé, dans les simulations d'ELMs, que le mode instable et l'équilibre cinétique (l'écoulement poloidal du plasma) ont une influence l'un sur l'autre. En particulier, le mode peut déclencher une rotation poloidale de forte amplitude, lorsque les filaments dus au mode de ballonnement sortent du plasma. Lorsque c'est le cas, cette rotation sépare les filaments du reste du plasma, un effet d'une grande importance et qui mérite d'être étudié. Cette rotation aide les filaments à se séparer du plasma, mais cela ne veut pas forcément dire qu'elle aide l'instabilité à évacuer de l'énergie. Au contraire, il se pourrait que cette rotation survienne lorsque des filaments sortent du plasma, justement pour empêcher que ces filaments évacuent trop d'énergie, car lorsque la rotation se met en place, le mode est stabilisé. Il est donc certain que la rotation poloidale puisse jouer un rôle important dans la non-linéarité et l'amplitude de l'instabilité. D'autre part, dans les simulations d'équilibres, en l'absence de modes, une rotation poloidale importante est observée. Il se pourrait ainsi que la rotation, déjà présente à l'équilibre, puisse influencer les modes de ballonnements.

Puisqu'il s'agit de la rotation poloidale, une première étude a été menée sur la rotation à l'équilibre sans vitesse toroidale, qui est simplement exclue du modèle physique. Une première partie du travail a pour rôle d'identifier et de comprendre cette rotation d'équilibre dans les plasma circulaires (sans point-X), et une interprétation analytique est donnée, puis comparée aux résultats des simulations. S'en suit l'étude de la rotation dans les plasmas avec point-X, qui révèle les principaux paramètres ayant une influence sur la rotation. Aussi, dans les plasmas avec point-X, un phénomène singulier se produit de manière très régulière: une transition entre deux états stationnaire distincts de rotations. Etant donnée l'importance de la transition L-H dans la physique des tokamaks, ce phénomène est étudié avec précaution. Enfin, pour parfaire cette analyse progressive de la rotation d'équilibre, les plasmas avec point-X sont simulés en incluant la vitesse parallèle dans le modèle. Il s'avère que cette variable a une importance significative concernant la structure de la rotation poloidale. En clair, si le même plasma est simulé avec et sans vitesse toroidale, la structure de la rotation poloidale d'équilibre peut être, dans certains cas, tout à fait différente. De plus, la structure de la rotation, lorsque v_{\parallel} est incluse, est fortement similaire à celle observée après les transitions qui surviennent lors des simulations sans v_{\parallel} . Ici encore, une interprétation

analytique est présentée, puis comparée aux résultats de simulations. En résumé, cette interprétation montre que la rotation poloidale observée est causée par la déviation de la densité par rapport aux surfaces de flux (due à la diffusion), qui est minimisée par la vitesse parallèle v_{\parallel} ; à son tour, la vitesse parallèle, ainsi engendrée, provoque une rotation poloidale. Ceci, entre autres, montre l'influence majeure que peut avoir le point-X dans les simulations des plasma de tokamaks.

Enfin, après avoir identifié la rotation poloidale d'équilibre avec minutie, son influence envers les modes de ballonnements est considérée. On démarque trois effets majeurs. Le premier effet est que la rotation poloidale peut réduire les taux de croissance des modes, ce qui est assez bienvenu, non seulement de par cette étude sur les ELMs, mais aussi d'une manière plus générale, lorsque l'on considère la transition L-H. Car si la rotation poloidale peut diminuer le taux de croissances des modes instables et qu'en plus, comme a été énoncé plus haut, les modes instables provoquent une forte rotation poloidale en revers, alors une réaction en chaîne pourrait très bien se produire, grâce à ce genre de causes et effets. Mais enfin, pour en revenir à l'effet de la rotation poloidale sur les ELMs, le deuxième aspect s'observe lorsque les filaments sortent du plasma: en l'absence de rotation d'équilibre, ces filaments ne sont pas arrêtés, et il évacuent une grande quantité d'énergie du piédestal. En revanche, si la rotation d'équilibre est prise en compte dans les simulations, celle-ci freine les filaments, et peut même les empêcher de vraiment sortir du plasma. Là encore, la relation entre la rotation et le transport transverse est évidente. Le troisième effet, le plus significatif, c'est que lors d'une simulation d'ELMs, la rotation poloidale peut stabiliser les modes de ballonnements, et ceci pendant assez de temps pour pouvoir observer un arrêt du crash, jusqu'à ce que le mode réapparaisse, pour être stabilisé à nouveau par la rotation. Ainsi, on observe des crash assez réguliers, qui pourraient bien correspondre à certains types d'ELMs (les type-III en particulier). Ce résultat est un premier pas vers les simulations d'ELMs multiples, et il prouve que la rotation poloidale, dans les plasmas avec point-X, joue un rôle très important, en matière de dynamique non-linéaire.

3.2 Introduction and Motivation

3.2.1 Starting From an Unstable Equilibrium

It has been stated, at the end of the previous section, that simulations of ballooning modes are started from an already unstable plasma equilibrium. As will be seen at the end of this chapter, some simulations may produce multiple crashes at regular frequencies. However the simulation of type-I

ELMy H-modes has yet not been achieved with JOEUK. One reason for this is that simulating one real type-I ELM is numerically very demanding, because of the grid resolution required to solve the fine filamentary structures of the modes. Therefore, such simulations cannot be run on a daily basis. In addition, it is never guaranteed that, after a first ELM crash, the pressure gradient will build back up in such a way that a second crash is obtained. Two extreme examples are presented here to illustrate these two issues. A first example where the crash never ends, evacuating pressure permanently, and a second example where, after the first crash, the gradients build back up until the mode is slowly excited again, and a quasi-steady state of turbulent transport is reached.

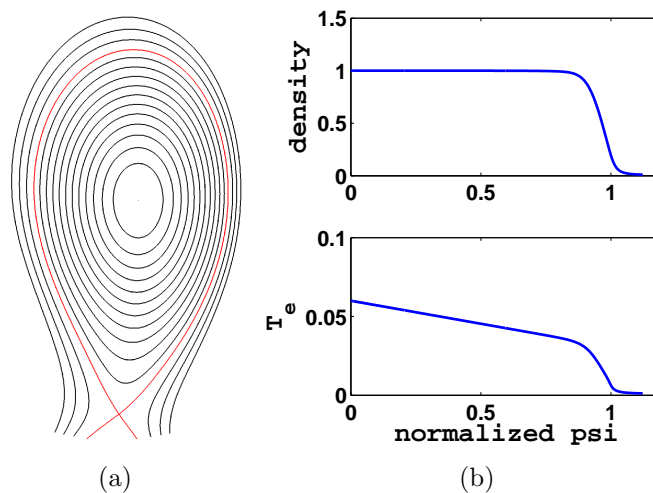


Figure 23: *a). Poloidal flux contours for the standard plasma equilibrium chosen. b). The density and T_e profiles chosen for this same equilibrium.*

The linear MHD stability of a given plasma equilibrium can be tested with linear codes, such as HELENA. Two similar equilibria are tested and compared. The main difference between the two cases is the pressure, which is varied by a factor of 2. The global geometry is the same, and close to that of JET, with a major radius of 3.2m, a minor radius of 0.85m and an ellipticity of 1.6. For the high pressure plasma, the electron temperature at the magnetic axis is chosen to be $T_e = 0.3 \times 10^{21} n_0^{-1} \text{keV}$, where n_0 is the plasma density at the magnetic axis - recall that equations are normalized with density, as described in Chapter 3. So for a plasma density of 6.10^{19}m^{-3} , the plasma electron temperature is $T_e = 5 \text{keV}$. The ion temperature is taken identical to that of electrons, and the pedestal width is chosen to be 6cm. The density profile is chosen to be almost flat, so that the density at the top of the

pedestal is not far below the density at the magnetic axis. The temperature profile, however, is chosen to be a little peaked, so that the temperature at the top of the pedestal is half the temperature at the magnetic axis. The magnetic field strength is set to $B_0 = 2.6\text{T}$ and the total plasma current is 2.75MA . The corresponding poloidal and toroidal beta-values are $\beta_p = 0.55$ and $\beta_t = 0.018$, and the safety factor is 1.1 at the axis and $q_{95} = 3$. Fig.23a shows poloidal flux contours of the plasma equilibrium and Fig.23b shows the profiles of normalised density and electron temperature. Unless specified otherwise, this is the standard equilibrium used throughout this chapter.

The two equilibria are tested with the linear code HELENA, and the result is shown in Fig.24, where the pressure gradient α is plotted as a function of the radial coordinate ψ_n . The red crosses mark locations that are unstable with respect to ballooning modes. The weaker pressure equilibrium is stable with respect to ballooning modes, even though the pressure is not that weak - T_e is still 2.5keV . This shows that the ideal MHD stability of ballooning modes is very sensible to pressure profiles. Starting with a plasma equilibrium inspired from experimental conditions and tested for its linear MHD instability brings some insurance that the simulations will effectively produce a pedestal collapse.

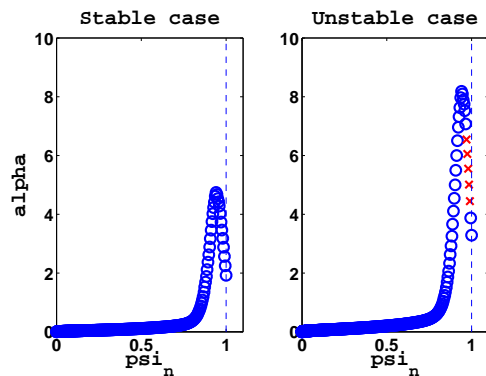


Figure 24: Two plasma equilibria are tested with the HELENA code for their linear ideal MHD ballooning stability. The left plot shows the pressure gradient α as a function of ψ_n for a plasma with low pressure, and the right plot shows the same for an equilibrium with a twice higher pressure. The red crosses mark unstable locations: the weaker pressure plasma is stable to ballooning modes.

However, some non-ideal MHD parameters, such as resistivity η and viscosity μ , may have a strong influence on the linear stability of ballooning modes, so that, the growth rates of the modes may either be damped or increased by these parameters. In fact, even if a given plasma equilibrium is ideally stable with respect to ballooning modes, it may still be used to sim-

ulate pedestal crashes if those plasma parameters are chosen carefully. Likewise, an ideally unstable plasma equilibrium, like the one described above, may turn out stable in simulations, provided the plasma parameters are kept within certain limits. As an example to illustrate this fact, Fig.25 shows the dependency of ballooning growth rates as a function of the two plasma parameters η and μ , for the mode number $n = 8$ with the above (ideally unstable) equilibrium. The modes are excited with increasing resistivity, and damped with increasing viscosity. All other plasma parameters (D_{\perp} , κ_{\perp} , κ_{\parallel} , μ_{\parallel}) also have an influence on the linear stability of ballooning modes. Ideally, one wishes to produce simulations with all parameters at the correct experimental or theoretical values, but numerical limits do not allow it (due to grid resolution).

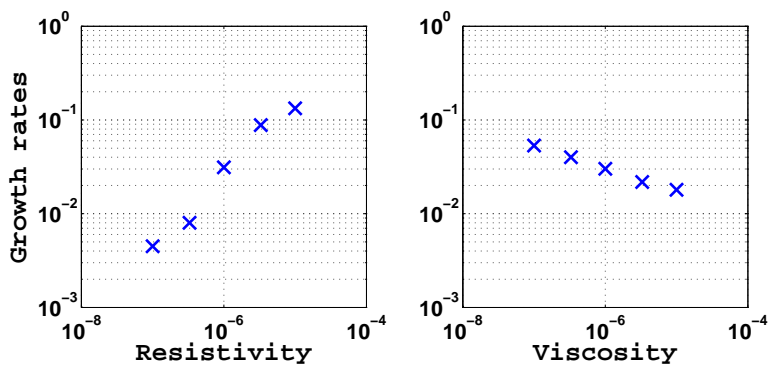


Figure 25: *The growth rates of ballooning mode $n = 8$ as a function of resistivity η and viscosity μ .*

In order to produce simulations with a resistivity close to correct (Spitzer) values, one needs to solve the thin current structures formed during the crash, so that a high-resolution grid is necessary. This significantly increases the number of unknowns to be solved, so that numerical limits (in terms of CPU memory) are quickly reached. Such simulations are presented in Chapter 4, although few of those simulations could be achieved due to the CPU costs they represent. Usually, simulations are run with a reasonable amount of parallel CPUs (256-512), which limits the grid-size, and thus limits the minimum value of η to be used. A poloidal grid of about 6 000 elements is used for the simulations shown in this chapter (40 radial times 100 poloidal plus SOL elements). With such grid resolutions, resistivity is taken between 10^{-7} and 10^{-5} . The simulation shown in Fig.26 is that of a JET plasma, with a resistivity of 10^{-6} . This is $2 \cdot 10^3$ times higher than the correct Spitzer resistivity. The evolution of the ELM-affected area is plotted as a function of time (a), together with a poloidal cut of density before and after the crash (b). The

ballooning mode progressively evacuates the whole plasma pressure, which is clearly not what is observed in experiments, where ELMs only evacuate pressure from the plasma edge. In such a case, a type-I ELMy H-mode will clearly not be obtained. More details about simulations of JET are given in Chapter 5, this example is presented here to show that a simulation with high resistivity does not usually lead to what is experimentally referred to as a type-I ELM crash.

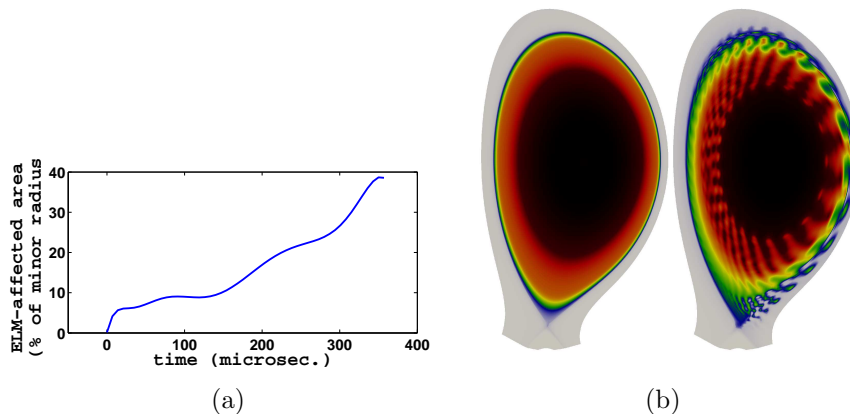


Figure 26: A ballooning mode simulation with relatively high resistivity. a). shows the evolution of the ELM-affected area as a function of time, and b). shows the density before and after the crash.

There is a second example that illustrates why it is not so trivial to produce multiple ELMs simulations. In cases where a first pedestal collapse is obtained, followed by a quiet (stable) phase - as opposed to the case described above - a second ELM crash may never be obtained. Fig.27 shows the time evolution of the plasma equilibrium in blue (kinetic energy), and the kinetic energies of the sine and cosine components of the ballooning mode $n = 8$. During the quiet phase, the heating and density sources cause the pressure gradient to increase progressively, until the mode is excited and starts evacuating pressure again. At this point, instead of a second pedestal collapse, one observes that the mode only evacuates pressure at a steady rate, creating a rather regular turbulent transport. After a time, heating power is increased again, in the hope that this might provoke a pedestal crash. Instead, a second level of steady turbulence is reached. This second example, together with the first one above, justifies why simulations of ballooning modes are started from an initially unstable equilibrium. Nevertheless, there is hope that with the constant progress of simulation performances and CPU capabilities, one may be able to use the JOREK code, in near future, to simulate experimentally relevant type-I ELMy H-modes, with an ELM-frequency related to heating

power. For now, simulations may already bring some further understanding of ballooning modes and their role in ELMs physics.

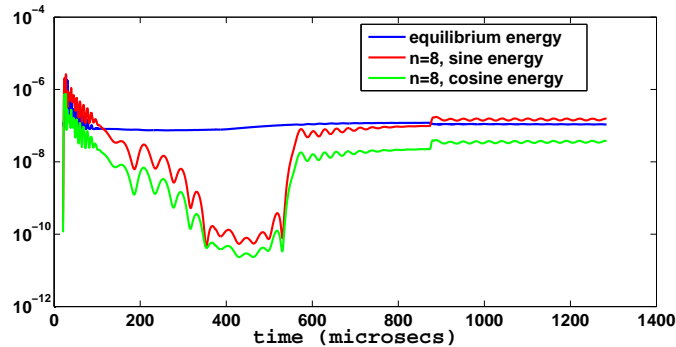


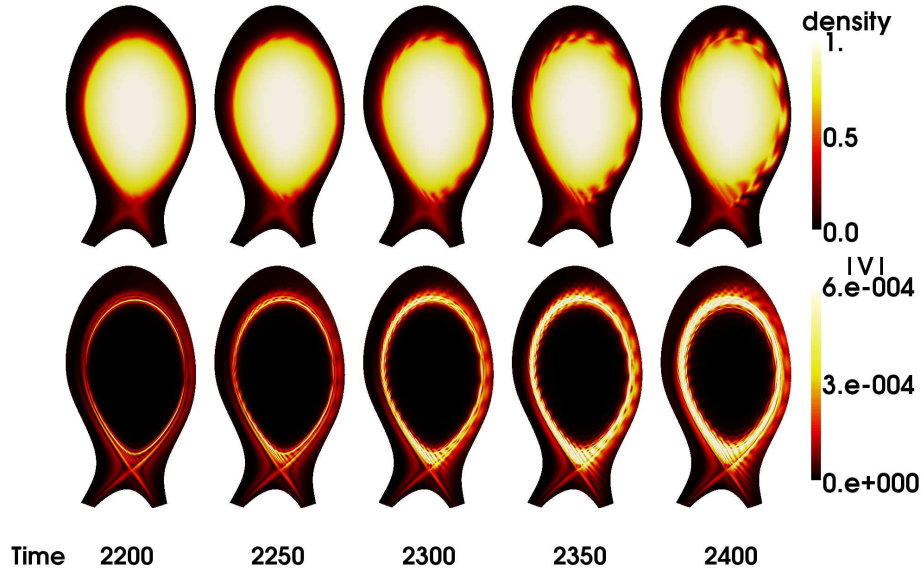
Figure 27: A simulation where after a first pedestal crash, heating and density sources cause the pedestal pressure gradient to increase progressively. When the mode becomes unstable again, a steady-state turbulence is reached. After some time, heating power is increased again, and a second (higher) steady turbulence state is reached.

3.2.2 Poloidal Flows at Equilibrium and During ELMs

Although the L-H transition has yet never been clearly explained theoretically, it has been shown, both experimentally and theoretically, that the $\mathbf{E} \times \mathbf{B}$ rotation played a fundamental role in H-mode physics [15-19]. In H-mode regime, large pressure gradients build up in the pedestal region, due to a stabilization of turbulent transport in that region. This suppression of transport is commonly agreed to be due to a large poloidal flow inside the last closed flux surface. Since the H-mode and ELMs are tightly related, one expects the equilibrium poloidal flow to play an important role in the stability and evolution of ballooning instabilities.

In nonlinear simulations of ELMs with JOEUK, a strong $m=n=0$ poloidal flow is nonlinearly induced by the instability (see Fig.28) - m and n are the poloidal and toroidal mode numbers respectively. This flow layer is localised in the H-mode pedestal region and has a significant effect on the nonlinear behaviour of ballooning instabilities. The equilibrium is perturbed as soon as the first density filaments (density tubes aligned to field lines) start crossing the separatrix, resulting in a poloidal rotation that prevents more plasma from escaping into the Scrape Of Layer (SOL). At equilibrium, in the absence of ballooning modes, simulations also exhibit strong poloidal flows. Such equilibrium poloidal rotations have already been observed in the H-mode pedestal region, both experimentally [40-45] and numerically [46-49]. Depending on plasma parameters and pressure gradients, different flow

Figure 28: *Nonlinear Simulation of a ballooning mode instability (ELM). Top row shows the density filaments coming through the separatrix, and bottom row shows the poloidal rotation with a strong $m=0$ structure.*



patterns are observed (see Fig.29), with structures and amplitudes that are sometimes very close to the rotation induced during a ballooning instability.

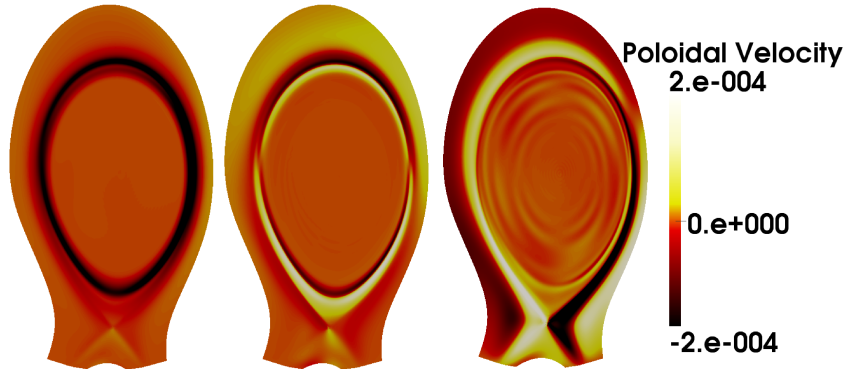


Figure 29: *Different steady-state equilibrium poloidal flow structures, obtained by varying plasma parameters such as η , μ and D_{\perp} . Left is an $m=0$ structure, middle is an $m=1 \sin \theta$ structure with multiple sheared layers inside the separatrix, and right is an $m=1 \cos \theta$ structure (mostly) outside the separatrix*

Since, as explained above, simulations of ballooning modes are started from initially unstable equilibria, it is important to understand the basic

mechanisms of poloidal equilibrium flows, particularly if the structure and amplitude of these flows significantly changes from one equilibrium to the other. In addition, since in some cases the amplitude of the equilibrium flow is close to that which is nonlinearly induced by the ELMs, one may expect the equilibrium flow to play an important role in simulations of ELMs. This chapter focuses on the edge poloidal rotation of quasi-steady equilibria, and its influence on ballooning modes. It takes a long time for the pressure profile to settle according to the balance between sources and diffusivities, with transport time scales inversely proportional to perpendicular diffusions, reaching up to $\tau \sim 10^7$ normalized times (ie. near Alfvén times). On the other hand, the electric potential will steady much faster (on Alfvén time scales), according to the Grad-Shafranov equilibrium $\vec{J} \times \vec{B} = \nabla p$. Nevertheless, due to the sonic boundary conditions for parallel velocity at the divertor (see Chapter 2), sound speed time scales are needed to reach a steady equilibrium. In order to respect this sonic time scale, which is longer than the Alfvén time scale, simulations are run over 10^3 Alfvén times. In the following, the 'quasi-steady' is dropped for convenience, and equilibrium denotes an axisymmetric plasma with a stationary flow. It should also be noted that this stationary flow is a consequence of the MHD equations (122-130) solved in simulations, and is therefore self-consistent with the plasma pressure, current, geometry and so on. This distinguishes from *equilibria with flow*, where the plasma equilibrium settles according to an externally prescribed flow source, which is a different procedure used to study the influence of plasma flows on equilibria and MHD instabilities [50-52].

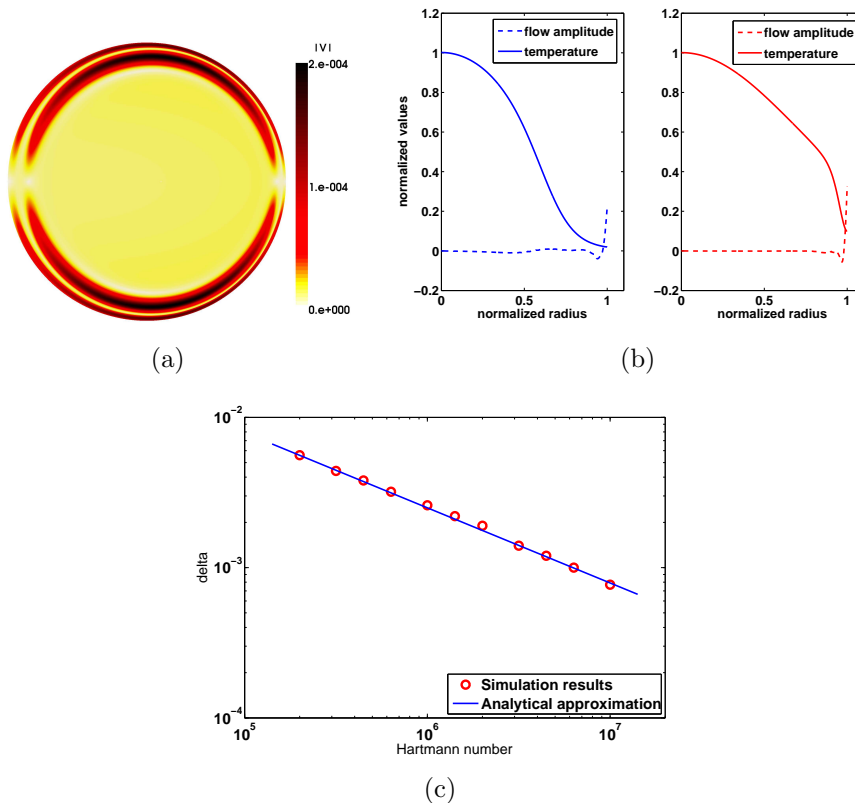
3.3 Equilibrium Poloidal Flows without Parallel Velocity

3.3.1 Flows in Circular Plasmas

ELMs are known to occur only in H-mode plasmas, ie. in tokamaks with an X-point configuration, but before studying equilibrium flows in such geometry circular plasmas should be investigated, which enables straight-forward analytical investigation. Also, the parallel velocity v_{\parallel} is neglected for now, both in the simulations and the theoretical approach. In simulations of circular plasmas at equilibrium, two distinct flows are observed: one in a thin boundary layer near the ideal wall and the other at the pressure gradient, away from the wall. Although these two flows are caused by different physics, their structures are very similar. Fig.30a shows the amplitude of the poloidal flow: there is a clear $\sin \theta$ dependence. Hence in the following text (unless otherwise specified), the notation $m=1$ or $\sin \theta$ will be used to express the

sine component of the first poloidal mode $m=1$. A similar flow structure at the pressure gradient is also observed in simulations of X-point plasmas, so the flow located at the pressure gradient will be addressed in the next section. For now, consider the boundary layer flow near the wall.

Figure 30: *The poloidal flow in a circular plasma is shown in figure (a). Two $m=1$ convection cells form at the pressure gradient situated inside the plasma, but also in a thin layer near the wall. The legend is normalized to the Alfvén speed, so that the flow is of the order of the $\text{km}\cdot\text{s}^{-1}$. On Figure (b) is shown the temperature and flow profiles for two simulations with identical parameters ($\eta, \mu\dots$). The first simulation (left) has a temperature gradient away from plasma, and the other simulation is the same as shown in Figure (a), with a temperature gradient near the wall. Both simulations exhibit a strong boundary layer flow. Figure (c) shows the thickness of the boundary layer as a function of the Hartmann number. The red circles represent simulation results and the blue line represents identity (175) derived above.*



At equilibrium, all ∂_t terms are balanced by the sources, and toroidal axisymmetry implies that all ∂_ϕ terms be zero. Also, to simplify the derivation, the density is fixed at $\rho = 1$ inside the plasma (at least near the wall) and it is assumed that the temperature profile is known. There is no particular requirement for the temperature profile except that it cannot be con-

stant, in which case the $[R^2, p]$ term in the momentum equation vanishes at the boundary). This is illustrated in Fig.30b, where two simulations are run with identical parameters, except for the position of the temperature gradient. Both simulations exhibit similar boundary flows. Thus, the two equations governing the equilibrium are

$$[\psi, j] - [R^2, T] + \mu R \nabla^2 (R^2 W) = \frac{1}{2} [R^2, R^2 |\nabla_{\perp} u|^2] - [R^4 W, u] \quad (166)$$

$$\text{and } \eta(j - j_A) = -R[\psi, u]. \quad (167)$$

The Poisson brackets in circular coordinates (r, θ) are given by $[f, g] \approx \frac{1}{a} (f_r g_{\theta} - g_r f_{\theta})$, where f and g are arbitrary functions, and subscripts denote partial differentiation with respect to r and θ . Also, the minor radius has been approximated to $r \approx a$ for the boundary region near the wall. The boundary layer near the wall is represented by $r = a - \delta$, with $\delta \ll 1$. Based on numerical observations, the following choice is made

$$u = u_1 \sin \theta \quad (168)$$

$$\text{and } \psi = \psi_0 + \psi_1 \cos \theta, \quad (169)$$

with $\psi_1 \ll \psi_0$, and it is assumed that the radial profile of ψ_0 is linear near the wall, say $\partial_r \psi_0 = \text{const} = \psi'_0$. Thus, using $\partial_r \equiv -\delta^{-1}$ inside the boundary layer,

$$j \approx \partial_r^2 \psi = \frac{\psi_1}{\delta^2} \cos \theta \quad (170)$$

$$\text{and } W \approx \partial_r^2 u = \frac{u_1}{\delta^2} \sin \theta. \quad (171)$$

Now, using the above expressions for u , ψ and j , and assuming that $a \ll R_0$, one can solve for the $\cos \theta$ component of equation (167) to obtain

$$u_1 = -\frac{a\eta\psi_1}{R_0\psi'_0\delta^2}. \quad (172)$$

Note that equation (167) also involves an $m=0$ component, which may be used to solve the non-varying part of the current. Namely, if $j = j_0 + j_1 \cos \theta$ and $R \approx R_0$, then $j_0 = j_A$ which is zero near the wall. Using formula (172) and assuming that $\eta \sim \mu$, it follows that the two terms on the right-hand side of equation (166) are of higher order in $\left(\frac{\psi_1}{\psi_0}\right)$ than the viscous term of the left-hand side. So with the assumption that $\psi_1 \ll \psi_0$, these two terms become negligible when compared to the viscous term. Now, inside the plasma, away from the boundary layer, the viscous term may

be neglected assuming μ is small, and the momentum equation reduces to the Grad-Shafranov equilibrium $[R^2, T] = [\psi, j]$. However, the boundary conditions on j (both Neumann or Dirichlet) imply that the term $[\psi, j]$ has to vanish at the wall, which becomes evident when considering the Poisson brackets in (ψ, θ) -coordinates. This is not necessarily the case for the term $[R^2, T]$, both with Neumann or Dirichlet boundary conditions on T . Hence, inside the boundary layer, the momentum equation reduces to $[R^2, T] = \mu R \nabla^2 (R^2 W)$. Physically, this means that the current cannot compensate for the pressure near the boundary, which perturbs the electric potential. Hence, consider the two equations

$$[R^2, T] = [\psi, j] \text{ outside the b.l.} \quad (173)$$

$$\text{and } [R^2, T] = \mu R \nabla^2 (R^2 W) \text{ inside the b.l.} \quad (174)$$

Subtracting to express the meeting point of the two regions ‘outside’ and ‘inside’ the boundary layer,

$$[\psi, j] = \mu R \nabla^2 (R^2 W).$$

Using the previous identities (170),(171) and (172), this equation gives the size of the boundary layer as a function of resistivity and viscosity (the Hartmann number $H = \frac{1}{\sqrt{\eta\mu}}$):

$$\delta = \sqrt{\frac{aR_0}{\psi'_0}} (\mu\eta)^{\frac{1}{4}} = \sqrt{\frac{aR_0}{\psi'_0}} H^{-\frac{1}{2}}. \quad (175)$$

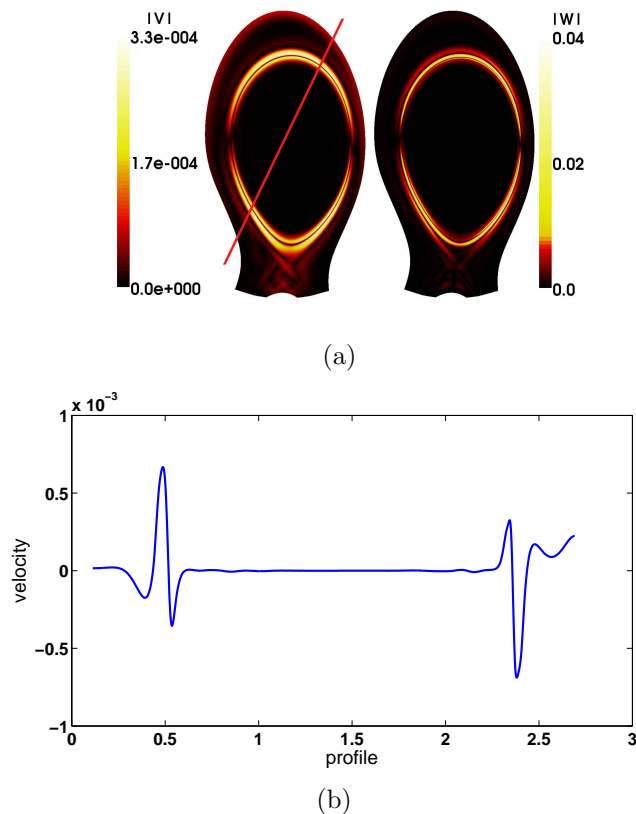
Fig.30c shows a comparison of the analytical approximation (175) with numerical results, where η and μ have both been varied independently.

3.3.2 Flows in X-point Plasmas

In simulations of X-point plasmas without $\vec{v}_{||}$, there are various types of equilibrium flow patterns. Some flows are situated strictly inside the last closed flux surface, and others can be rather outside the separatrix than inside. However, a particular flow is regularly observed inside the separatrix, where the pedestal pressure gradient is very steep. This flow has an $m=1 \sin\theta$ structure, exactly like the flow in circular plasmas. The only difference with the circular plasma flow is that here, this $m=1$ flow consists of multiple convection cells which are radially close and of opposite directions, thus forming a strong vorticity sheath (see Fig.31). The radial number of these flow cells may vary from one to three. In simulations of circular plasmas, only one convection cell is observed at the pressure gradient. Although the reason

for the formation of multiple flow cells in X-point plasmas is clearly due to the separatrix, since geometry is the only difference between section 3 and Section 4, no interpretation of the role of the separatrix (concerning multiple flow cells) is attempted here. Generally, the radial width of these cells does not exceed 15% of the minor radius a (ie. it is of the same order as the pedestal width). Very similar $m=1$ flows, with multiple cells, have already been observed in MHD simulations of equilibria with an X-point geometry [47-49].

Figure 31: *Typical equilibrium flow structure in simulations of X-point plasmas without \bar{v}_{\parallel} . Figure (a) shows the flow amplitude normalized to the Alfvén speed (left) with the corresponding toroidal vorticity (right). The pedestal gradient width is 6cm. Figure (b) gives a profile of the flow taken along the diagonal line on the left plot.*



An interpretation of the flow amplitude may be derived as follows. In the circular case, (r, θ) coordinates were used. With the X-point configuration, it is more convenient to use (ψ, θ) coordinates, specially when dealing with Poisson brackets, so that $[\psi, \cdot] = \partial_{\theta}(\cdot)$. Since the thin layer approximation used in Section 3 is also valid here, where the layer stands for the pedestal

width, it is directly assumed that the equilibrium can be described by the two equations

$$[\psi, j] = [R^2, p] \quad (176)$$

$$\text{and } \eta(j - j_A) = -R[\psi, u]. \quad (177)$$

Also, the following expressions for the electric potential u and the current j will be used

$$u = u_1 \sin \theta \quad (178)$$

$$\text{and } j = j_2 \cos \theta. \quad (179)$$

Solving for the $\cos \theta$ component of equation (177) gives $j_2 = -R_0 u_1 / \eta$. Then, assuming (for crude simplicity) that $R \approx R_0 + a \cos \theta$ in the pedestal region, the $\sin \theta$ component of equation (176) gives $j_2 = -2R_0 \partial_\psi p$. In other words, combining both expressions to eliminate j_2 ,

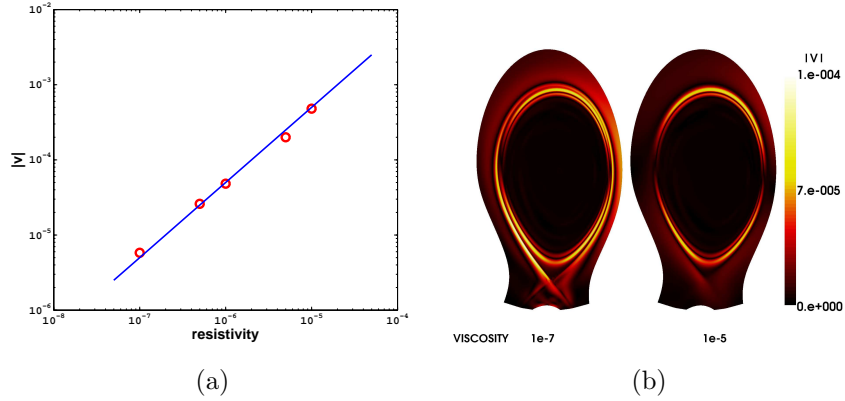
$$u_1 = 2\eta \partial_\psi p. \quad (180)$$

Fig.32a shows a numerical scan of the resistivity parameter. The $\sin \theta$ -component of the poloidal velocity is calculated using Fourier decomposition along flux surfaces. The relation $|\vec{v}_{\sin \theta}| \sim \eta$ is clearly satisfied. This plot focuses on the linear relation to resistivity, but the result (180) is also valid when considering the amplitude of the flow. For those simulations, which have a pedestal pressure $p = 2.10^{-2}$ (normalized units), together with a pedestal width of 5cm and a major radius $R_0 = 3\text{m}$, the poloidal velocity amplitude is expressed as

$$\begin{aligned} |v| &= R^2 |\nabla u \times \nabla \phi| \approx R_0 \partial_\psi u_1 \\ &= \frac{R_0 u_1}{\delta} \\ &= \frac{2R_0 \eta p_0}{\delta^2} \\ &\approx 5.10^1 \eta, \end{aligned}$$

which corresponds to the values shown in Fig.32a. It should also be noted that resistivity has no influence on the width of the flow cells. The resistivity plays an important role in the circular case because the flow is generated by the boundary conditions on the current j , which is directly related to resistivity by Ohm's law. Here, the flow is generated by the pressure gradient, not by boundary conditions, which explains the two different behaviours. Hence, concerning the width of the flow, the Hartmann number does not play such an important role as in the circular case.

Figure 32: Figure (a) shows the amplitude of the $\sin\theta$ -component of the poloidal velocity as a function of the resistivity η . Red circles represent simulation results and the blue line shows the linear dependence $|\vec{v}| \sim \eta$. Figure (b) shows two simulations of equilibrium flows with different viscosities.

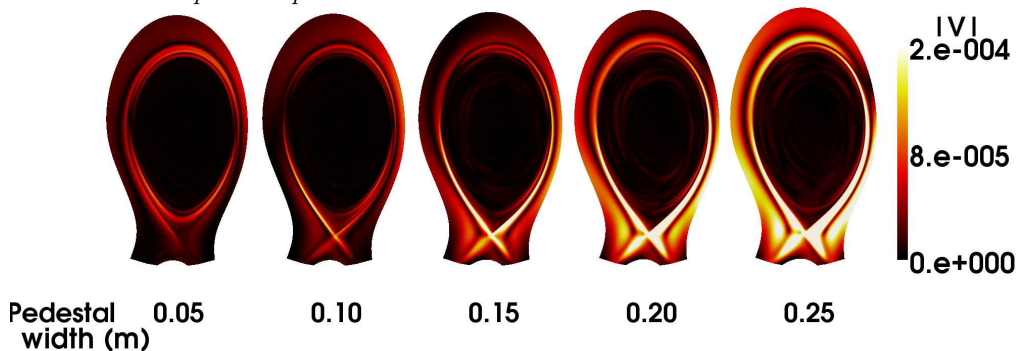


In fact, the viscosity also takes a different role here than with circular plasmas. Although it has a strong influence on the structure of the flow outside the separatrix, it has no influence at all on the flow inside the separatrix: the structure, amplitude and width are identical for all values of μ (between 10^{-7} and 10^{-5}). Fig.32b shows two simulations of equilibria with different viscosities. The only difference is the flow outside the separatrix. This is somehow surprising - one would expect viscosity to have a strong influence on the flow inside the separatrix, considering the latter is strongly sheared. However, this is in good agreement with the fact that the viscous term has been neglected in the derivation above, so that the vorticity equation reduces to $[\psi, j] = [R^2, p]$. Again, this is different from the circular case, where the boundary conditions forced the term $[\psi, j]$ to zero at the boundary, implying that the difference $[\psi, j] - [R^2, p]$ had no choice but to be balanced by the viscous term. In X-point geometry, the absence of boundary conditions for j at the separatrix enable the two terms $[\psi, j]$ and $[R^2, p]$ to balance without influencing the viscous term.

At last, one would also expect the width of the flow cells inside the separatrix to be related to the width of the pedestal pressure gradient, but no clear relation could be identified. Scans on the pedestal width at constant pressure have shown that the flow amplitude does increase linearly with the pressure gradient, as expected from equation (180), but the width of flow cells does not depend on the pedestal width. Instead, the pedestal width seems to affect the whole structure of the flow. Fig.33 shows simulations with constant pressure and pedestal width varying from 0.05 to 0.25m : an-

other flow outside the separatrix overtakes the usual $m=1$ flow. Although no clear relation has been found between the pedestal width and the flow width, this last numerical scan exhibits the strong influence of the pressure gradient on the global structure of the flow. In fact, simulations of equilibria on long time-scales (around 10^5 Alfvén times) with a progressively decaying pedestal resulted in sharp transitions between distinct, stable flow structures.

Figure 33: *This scan shows the poloidal equilibrium flow as a function of the pedestal width at constant pedestal pressure.*



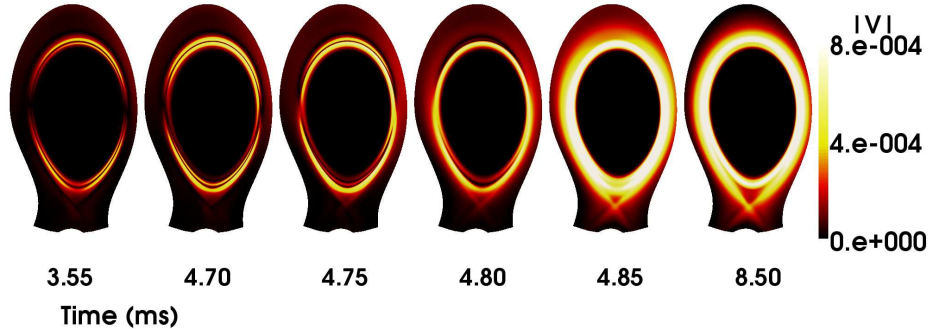
3.4 Circular Poloidal Rotation of the Pedestal Plasma

3.4.1 Transitions Between Equilibrium Flow States

In simulations of ballooning instabilities (ELMs), abrupt changes of the pedestal pressure are involved, which may have a significant effect on the equilibrium flow state. Of course, at equilibrium, if the particle source and heating power are adjusted according to the perpendicular mass diffusivity and thermal conductivity, the density and temperature profiles will remain unchanged, and so will the flow. However, simulations of equilibria have been run without sources on long time scales, resulting in a slow diffusive decrease of the pedestal pressure. These simulations have revealed that there are different steady flow states, and abrupt transitions may occur from one state to the other (see Fig.34). The initial state is the usual $m=1 \sin \theta$ flow structure, and the final state is an $m=0$ flow structure. This rapid bifurcation lasts around a few ms ($\sim 10^4$ Alfvén times). After the transition, if sources are turned back on, a backward transition is observed. Using Fourier decomposition, it has been verified that only the $m=0$ component of the flow is concerned. Fig.35a shows the two components $m=1 \sin \theta$ and $m=0$ as

functions of time, which shows that the usual $m=1$ equilibrium flow is not affected by the transition.

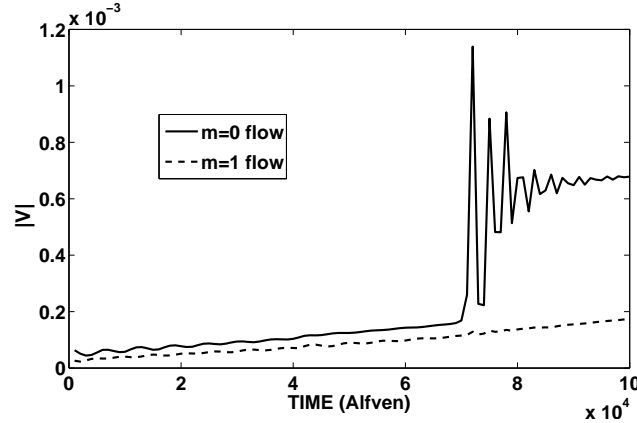
Figure 34: *Transition between a predominantly $m=1$ flow to an $m=0$ flow structure. Note that the first and last images are taken at times long before and long after the transition respectively. This illustrates the fact that both flow patterns are steady.*



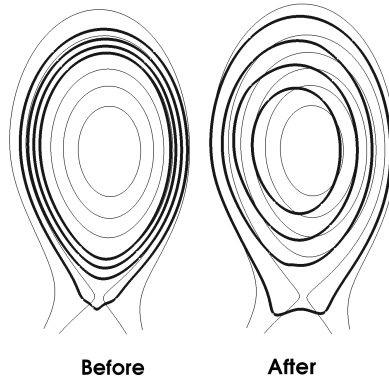
Numerical scans in resistivity have shown that both components are linked to resistivity. As shown above, the relation $v_{\sin\theta} \sim \eta$ holds, and the $m=0$ component of the flow scales as $v_{m=0} \sim \eta$ before the transition, and as $v_{m=0} \sim \eta^{1/2}$ after the transition. This emphasizes the fact that the pre- and post-transition states are distinct, and that resistivity plays an important role in this transition. Scalings with other parameters have also led to some distinction between the two flow components. The usual flow $v_{\sin\theta}$ is strongly linked to the perpendicular thermal conductivity (it scales as $\sim \kappa_{\perp}^{0.5}$ for low values of κ_{\perp}), but it has no dependency on the perpendicular mass diffusivity D_{\perp} . On the other hand, the component $v_{m=0}$ has exactly the opposite behaviour : it depends on D_{\perp} but not on κ_{\perp} . In fact, $v_{m=0}$ is tightly related to density, and the transition comes together with an inward shift of the density, which is illustrated in Fig.35b.

A theory developed by H.R. Strauss predicts such transitions of the flow at equilibrium [46]. Some characteristics of the transition in JOREK simulations are comparable to these predictions. The interpretation given by Strauss is that the X-point geometry, together with the mass diffusivity, induces a slight deviation of pressure from flux surfaces, which is the cause for an $m=0$ flow. Some figures showing flux and pressure contours in [46] exhibit an horizontal shift of the pressure towards the high-field side, as in simulations presented here. However, simulations with JOREK clearly show that there is a relation between the transition and η , whereas Strauss neglects resistivity in his analytical derivation. Also, \vec{v}_{\parallel} has been neglected in simulations so far, whereas Strauss uses the parallel velocity in his approach. In fact, although the deviation of pressure clearly plays one of the main roles

Figure 35: The continuous line on figure (a) represents the $m=0$ flow amplitude as a function of time, and the dashed line stands for the amplitude of the $m=1$ component of the flow. Figure (b) shows two sets of contours taken before (left) and after (right) the transition. Thin lines represent flux contours and thick lines density contours.



(a)



(b)

here and in Strauss' derivation, \vec{v}_{\parallel} should be taken into account for proper comparisons.

3.4.2 Flows in Simulations with Parallel Velocity

In this section, the influence of the parallel velocity on the poloidal flow is discussed. There is a major change in the global structure of the poloidal flow : in simulations where the $m=1 \sin \theta$ flow would be dominant if \vec{v}_{\parallel} were neglected, a strong $m=0$ flow is now observed to be the steady flow pattern (see Fig.36). Furthermore, a strong perturbation of pressure is observed near the X-point. This, together with the fact that \vec{v}_{\parallel} is an essential ingredient for

the flow, confirms Strauss' theory [46]. An analytical interpretation of this $m=0$ flow is now derived, using assumptions based on simulation results.

It is now assumed that resistivity is negligible. In fact, in contrast with the importance of η for the transition in the previous chapter, and in agreement with Strauss' assumptions, simulations including \vec{v}_{\parallel} revealed that resistivity has no influence on the amplitude of the $m=0$ flow and its structure. The induction equation (167) thus gives

$$u = u(\psi). \quad (181)$$

Substituting into equation (128) gives the perpendicular velocity

$$\vec{v}_{\perp} = R \left(-\frac{\partial \mathcal{A}}{\partial \theta}, \frac{\partial u}{\partial \psi} \right). \quad (182)$$

Hence, the notation $\vec{v}_{\perp} = (0, Rv_0)$ will be adopted. Note that the major radius is kept in the poloidal component of the velocity, which corresponds with the permanent $\cos \theta$ asymmetry of the flow amplitude found in simulations, so that the flow is always strongest on the low-field side. Now, it is convenient to assume that the small radius is constant inside the pedestal region, say $r \approx 1$, so that $R \approx R_0 + \cos \theta$. Also, for the sake of simplicity, let us combine the temperature and density equations into one equation for the pressure p , so that the three equations governing the equilibrium are

$$\nabla \cdot (p\vec{v}) = \nabla \cdot (D_{\perp} \nabla_{\perp} p) + Source, \quad (183)$$

$$[\psi, p] = \mu_{\parallel} \nabla^2 v_{\parallel}, \quad (184)$$

$$[R^2, p] = [\psi, j] + \mu R \nabla^2 (R^2 W). \quad (185)$$

Here, the momentum equation has been simplified, as in the previous sections. Similarly, the Laplacian is approximated by $\nabla^2 \sim 1/\delta^2$, and the Poisson brackets in (ψ, θ) -coordinates give $[\psi, \cdot] = \partial_{\theta}(\cdot)$. Note that the equation for parallel velocity has been simplified in the same manner as the momentum equation, so that convection terms of order v^2 are ignored.

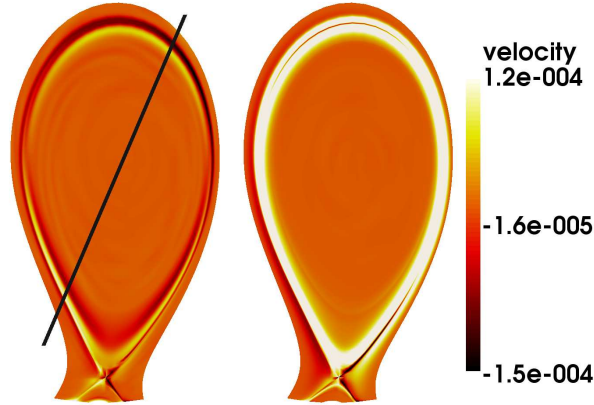
Now, consider the following assumptions on \tilde{p} and \tilde{v}_{\parallel} ,

$$p = p_0 + p_1 \sin \theta, \quad (186)$$

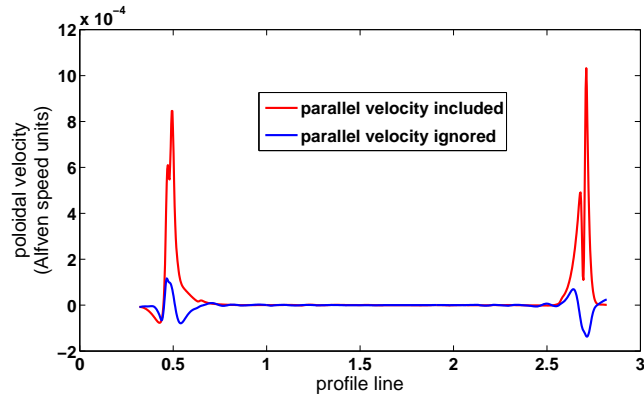
$$v_{\parallel} = v_2 \cos \theta, \quad (187)$$

where p_0 , p_1 and v_2 are functions of ψ only. Note that the assumption for v_{\parallel} is consistent with the X-point geometry and the usual structure of \vec{v}_{\parallel} in the SOL (negative on the HFS and positive on the LFS). Similarly, if the X-point induces a pressure perturbation, it will be localized near the X-point

Figure 36: Figure (a) shows the poloidal velocity if \vec{v}_{\parallel} is neglected (left), and if it is included (right). Figure (b) shows a profile of the poloidal velocity with and without \vec{v}_{\parallel} . This profile is taken along the diagonal line drawn on the left plot.



(a)



(b)

and will thus have a $\sin \theta$ contribution when considering the main Fourier components in (ψ, θ) -coordinates. Introducing these into the parallel velocity equation gives

$$v_2 = \frac{R_0 p_1 \delta^2}{\mu_{\parallel}}. \quad (188)$$

Next, consider the pressure equation. At equilibrium, using $\vec{B} \cdot \nabla =$

$-\frac{1}{R} [\psi, \cdot] \equiv -\frac{1}{R} \partial_\theta(\cdot)$, this equation gives

$$\frac{D_\perp p}{\delta^2} = \partial_\theta (R v_0 p) - \frac{1}{R} \partial_\theta (v_\parallel p). \quad (189)$$

Note that the source has been ignored, according to simulations, where sources are located in the plasma core, and thus vanish in the pedestal region. Clearly, the first term on right-hand side has no $m=0$ component. The second term, however, has a non-zero $m=0$ component because of the $1/R$ coefficient. To obtain the θ -independent part of the equation, consider the integral of the whole equation on a poloidal contour. The diffusion term gives

$$\frac{1}{2\pi} \int_0^{2\pi} \frac{D_\perp p}{\delta^2} d\theta = \frac{D_\perp p_0}{\delta^2}, \quad (190)$$

the first term on right-hand side vanishes, and the last term gives

$$\begin{aligned} & \frac{1}{2\pi} \int_0^{2\pi} \frac{p_0 v_2 \sin \theta - p_1 v_2 \cos(2\theta)}{R_0 + \cos \theta} d\theta \\ &= \frac{1}{2\pi} \left[-p_0 v_2 \log(R_0 + \cos \theta) + F(\theta) - \cancel{2R_0 p_1 v_2 \sin \theta} + 2R_0 p_1 v_2 \theta \right]_0^{2\pi} \\ &= 2R_0 p_1 v_2, \end{aligned}$$

where the function $F(\theta)$ is given by

$$F(\theta) = \frac{2p_1 v_2 (2R_0^2 - 1)}{\sqrt{1 - R_0^2}} \tanh^{-1} \left(\frac{R_0 - 1}{\sqrt{1 - R_0^2}} \tan \left(\frac{\theta}{2} \right) \right). \quad (191)$$

Hence, the $m=0$ part of the pressure equation gives

$$p_1 v_2 = \frac{D_\perp p_0}{2R_0 \delta^2}. \quad (192)$$

Now, combining the last two results (188) and (192), one may solve for p_1 and then substitute the result into the momentum equation to obtain v_0 . However, the momentum equation concerns $\nabla^2 W$, not v_0 , and even though one may argue that $\nabla^2 W \sim v_0/\delta^4$, one may also consider the term $\nabla^2 W$ as a separate variable, independent of the velocity amplitude v_0 . By doing so, the momentum equation does not provide the source for the poloidal flow. Instead, it produces a viscous damping of the flow shear. The main reason for doing this assumption is that simulations have shown that viscosity has only a weak influence on the flow amplitude, but a strong influence on its gradient. Thus, it may be argued that the source of the poloidal rotation does

not come from the vorticity equation. This contrasts from the derivation in [46], where the vorticity equation is explicitly used. Therefore, although the main assumptions are the same in the two models (ie. $\eta = 0$, v_{\parallel} included, perturbation of density by X-point geometry) the generation of the flow is different.

The source of the poloidal flow is found in the pressure equation. As before, one obtains the $\sin \theta$ part of this equation by applying the integral $\int_0^{2\pi} \sin \theta d\theta$, leading

$$\frac{D_{\perp} p_1}{2\delta^2} = -\frac{1}{2} p_0 v_0 + R_0 p_0 v_2. \quad (193)$$

This equation may be approximated by $v_0 = 2R_0 v_2$, since $p_1 \ll p_0$ leads to

$$\frac{D_{\perp} p_1}{2\delta^2 p_0} \ll 1. \quad (194)$$

Note that this last relation $v_0 = 2R_0 v_2$ is equivalent to incompressibility $\nabla \cdot \vec{v} = 0$, which is observed to be well satisfied in simulations. At last, the three results obtained, (188), (192) and $v_0 = 2R_0 v_2$ may be combined to obtain

$$v_0 = \pm R_0 \left(\frac{2D_{\perp} p_0}{\mu_{\parallel}} \right)^{\frac{1}{2}}. \quad (195)$$

This result reveals the essential role of \vec{v}_{\parallel} concerning the generation of a poloidal torque, which is in agreement with Strauss' theory [46]. Fig.37a shows the relation between the flow amplitude and μ_{\parallel} . Reasonable agreement is obtained. The relation to p_0 explains why, at lower pedestal pressure, this $m=0$ flow is overtaken by the usual $\sin \theta$ flow, which agrees with Aydemir's work, who considered relatively low values of toroidal β (around $5 \cdot 10^{-5}$ for single X-point plasmas, [47]). Also, simulations without an X-point have been carried out for circular plasmas (no up-down asymmetry) and an $m=0$ flow has been found, so it can be concluded that the X-point is not a necessary ingredient for $m=0$ flow. Nevertheless, in order for simulations without an X-point to reveal an $m=0$ flow, the total pressure needs to be increased to values that are not realistic for circular plasmas. This firstly confirms the role of p_0 in identity (195), but it also shows the importance of the X-point.

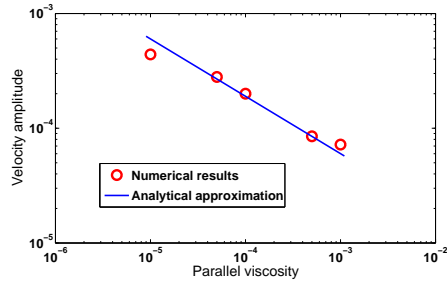
In fact, density is not constant on flux surfaces, particularly near the X-point, where a strong deviation of density from flux surfaces is observed. Simulations show that temperature is just weakly perturbed near the X-point, due to fast parallel transport that tends to even the temperature on a flux surface. In contrast, density is strongly perturbed near the X-point

and this deviation takes a $\sin \theta$ form when considering the main Fourier components of density in (ψ, θ) -coordinates. This draws the conclusion that density, rather than temperature, plays the leading role in generating the flow. It is delicate to show the dependency for D_{\perp} in equation (195) because the density gradient is strongly affected by the diffusivity, and the resulting relation is weaker than the 0.5 power predicted. It may however be verified that density is strongly perturbed near the separatrix and that this deviation is due to the X-point. The pressure deviation from flux surfaces may be split into two terms, $[\psi, p] = T[\psi, \rho] + \rho[\psi, T]$. Fig.37b shows the $\cos \theta$ component of these two terms as a function of ψ , illustrating the fact that the flow is due to the perturbation of density near the separatrix (rather than temperature). Note that the $\cos \theta$ part of these terms is equivalent to the $\sin \theta$ component of the perturbation, since $[\psi, p_1 \sin \theta] = p_1 \cos \theta$. Also, Fig.37c plots density as a function of the poloidal angle along a flux surface situated just inside the separatrix, where the flow is strongest. It demonstrates the fact that the $\sin \theta$ perturbation is due to the X-point.

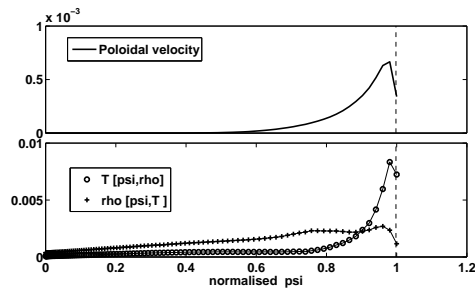
It should also be noted that no transition such as seen in the previous section has been observed in simulations including \vec{v}_{\parallel} . The paper from Strauss [46] states that simulations did exhibit a transition from very low to very strong flows as perpendicular diffusivity was varied. However, this paper does not state that time dependent transitions were obtained. This is concordant with the results shown here since, although no more transition is found, the theory given here also predicts a dependency on D_{\perp} , and the simulations show that at lower pressure no $m=0$ flow is observed. Whether clear, time-dependent transitions do not exist with this model is yet not sure. So far, they have not been observed.

At last, it should be observed that the $m=0$ flow after the transition is very similar to that found in simulations where \vec{v}_{\parallel} is considered. This similarity seems to be accidental, but it indeed gives support to the importance of pressure deviation from flux surfaces regarding poloidal flows, and thus strengthen the agreement with Strauss' work. In the first case, there was no parallel velocity, and the poloidal flow after the transition was clearly related to the deviation of density from flux surfaces. In the second case, the poloidal flow is due to presence of parallel velocity together with the deviation of density near the X-point, as shown above. Although the two mechanisms seem different, the coincidence that a density deviation from flux surfaces is required in both cases enhances its importance regarding the generation of $m=0$ poloidal flows. Furthermore, the fact that the X-point geometry be responsible for the deviation of density (and thus for the generation of the flow) is also in agreement with the theory derived by Strauss [46].

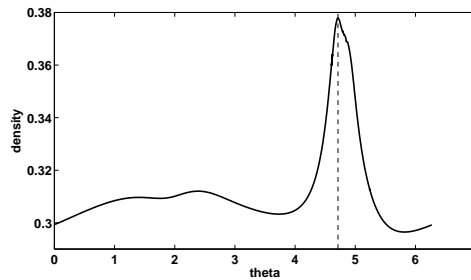
Figure 37: Validation of analytical result (195) with simulations. The relation between the flow amplitude and μ_{\parallel} is well respected (figure (a)). The pressure deviation from flux surfaces results from the deviation of temperature and density separately: $[\psi, p] = \rho[\psi, T] + T[\psi, \rho]$. Figure (b) shows the $\cos\theta$ component of these two terms (bottom) and the $m=0$ component of the poloidal velocity (top) as a function of the normalised flux ψ . The dashed line represents the separatrix. Figure (c) shows the density as a function of the poloidal angle θ , along a flux surface close to the separatrix (where the deviation is strongest). Here, the dashed line represents the position of the X-point.



(a)



(b)



(c)

3.5 Influence of the Poloidal Equilibrium flow on ELMs

3.5.1 Effect on the Linear Stability of Ballooning Modes

An important amount of work has long been addressed to the effect of toroidal rotation shear on the stability of edge-localized ballooning modes. In toka-

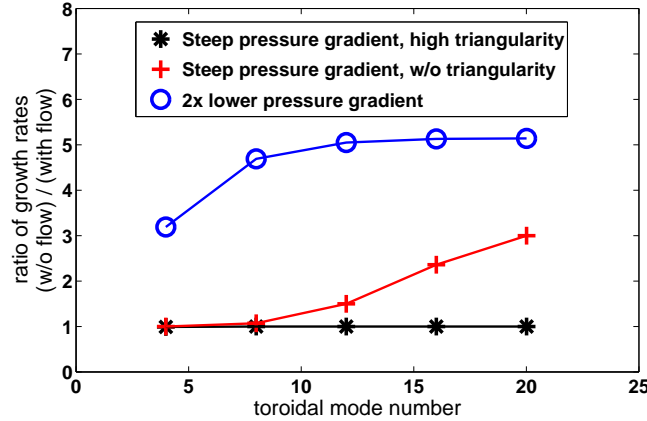
maks using the neutral beam injection (NBI) heating system, toroidal rotation is observed with significant shear at the plasma edge [55,56]. The stabilizing effect of this flow shear was first studied by Cooper [57] who introduced rotation effects to the WKB theory for high- n ideal MHD ballooning modes, initially developed by Connor *et al.* [58]. This issue has then largely been considered, both analytically and numerically [59-76]. Overall, the toroidal rotation has been found to have a stabilizing effect on ballooning modes, except for a few theories [73-76]. It should also be noted that such toroidal rotation may have a significant influence on ELMs mitigation processes [77]. However, these approaches all assume the toroidal flow to be entirely generated by an external source (experimentally, the NBI heating), and poloidal flow is either ignored, due to possible neoclassical damping, or included as an external source like the parallel flow. It has been demonstrated above that strong, self-consistent poloidal rotation may arise in plasma conditions that are experimentally reasonable. Such flows may well have an effect on the linear stability of edge-localised ballooning modes and their nonlinear evolution. Three influences will be discussed: The damping of growth rates, the constriction of filaments, and the reduction of perpendicular transport leading to ELM-like periodic crashes.

JOEKE simulations show that both the $m=1 \sin \theta$ flow (without \vec{v}_{\parallel}) and the $m=0$ flow (with \vec{v}_{\parallel}) have a stabilizing effect on ELMs. This effect increases for higher mode numbers, which agrees with Aydemir's work [47,48]. Garcia *et al.* also came to the conclusion that both $m=0$ and $m=1$ flows (sine *and* cosine separately) have a stabilizing effect on the growth rates of ballooning modes [78]. Fig.38 shows the ratio of growth rates, with and without the poloidal flow, as a function of the toroidal mode number. 'Without the flow' means that the $n=0$ component of the electric potential is artificially forced to zero at each time step. Fig.38 also shows that the stabilizing effect of the flow is limited by the ideal MHD stability of the plasma : in highly ballooning-unstable cases where the pedestal gradients are very steep, the flow has no effect at all on the linear stability of the modes. A similar result concerning JET was obtained by Saarelma *et al.*, so that only marginally unstable ballooning modes may be affected by toroidal flows [79]. Results concerning simulations of JET plasmas are presented in the next chapter, where the influence of the flow on ballooning modes in JET simulations is studied as well.

3.5.2 Effect on the Nonlinear Behaviour of Ballooning Modes

The poloidal flow also has a significant stabilizing effect on the nonlinear evolution of the modes. There is good qualitative agreement, both with Ay-

Figure 38: The ratio of growth rates $\frac{\gamma_{w/o \text{ flow}}}{\gamma_{with \text{ flow}}}$ is plotted as a function of toroidal mode numbers for different plasma conditions.



demir [47,48] and Pankin [75], concerning the effect of the poloidal flow on filaments: in the absence of a poloidal flow, density filaments reach through the separatrix and extend far into the SOL, whereas in simulations including the equilibrium flow, these filaments are stopped and remain very close to the separatrix. It was initially observed that an $m=0$ flow is nonlinearly induced during the ELM to restrain density from escaping the plasma core. It has been shown in the previous section that similar $m=0$ flows with comparable amplitudes may exist at equilibrium. In such conditions, it follows that the equilibrium flow may significantly reduce the activity of the ballooning mode in its nonlinear evolution. Fig.39a shows two poloidal cuts of filamentations of a plasma during a ballooning instability, one with, the other without equilibrium flow.

Consequently, a third effect of the flow on the nonlinear behaviour of ELMs has been observed: distinct repetitive bursts may occur at regular frequencies. Simulations with the JOEUK code have revealed that the equilibrium $m=0$ flow plays the key role concerning this multiple bursts behaviour. In fact, if the amplitude of the flow v_0 is high enough, the ballooning modes will evacuate pressure by repetitive bursts with a rather regular frequency ($\sim 3\text{kHz}$). The same simulation with a lower flow amplitude (10 times less) will exhibit a more violent nonlinear activity but no repetitive bursts. Note that two such equilibria with different flow amplitudes but similar pressure profiles may be obtained by varying the parallel viscosity parameter, as follows from result (195). Simulations with zero flow result in big pedestal collapse at once, without intermittent bursts - here zero flow means that the equilibrium part of the flow is set to zero at each time step. Neverthe-

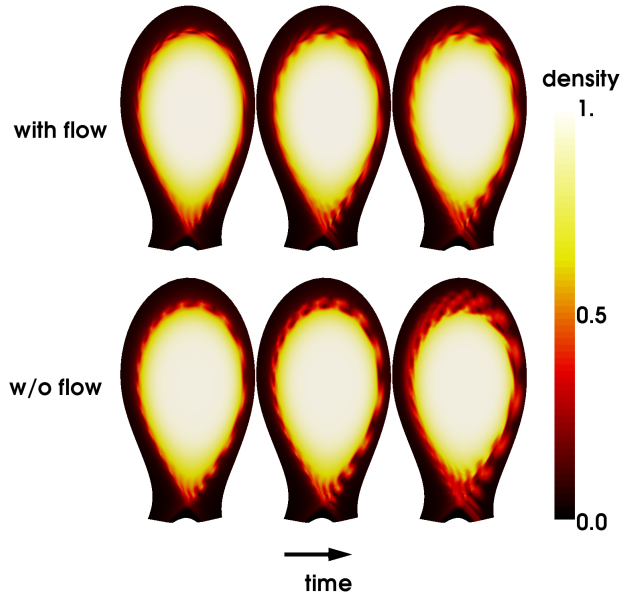
less it should be noted that, although they reveal the role of poloidal flows concerning the bursting behaviours of ballooning modes, these simulations where the equilibrium flow is artificially forced to zero are not consistent in terms of energy conservation. Also, the fact that equilibrium flows arising during ELMs simulations may limit ballooning perturbation has already been observed with the code JOEAK [80,81]. Beyer *et al.* have also been able to simulate repetitive bursts in a very similar way [82,83]: by forcing a chosen profile for the electric potential to create a strong flow shear at the pedestal, a transport barrier is created, leading to periodic relaxations of the plasma. An important aspect of these bursts is that the pedestal collapse at each crash is very small, so that the pressure gradient remains close to the linear instability boundary. These incomplete pedestal collapses show that more simulations are needed to seek for the real type-I ELMs regime. Further efforts to determine the role of the equilibrium flow in multiple ELMs simulations are under way with the JOEAK code.

3.5.3 Conclusion and Discussion

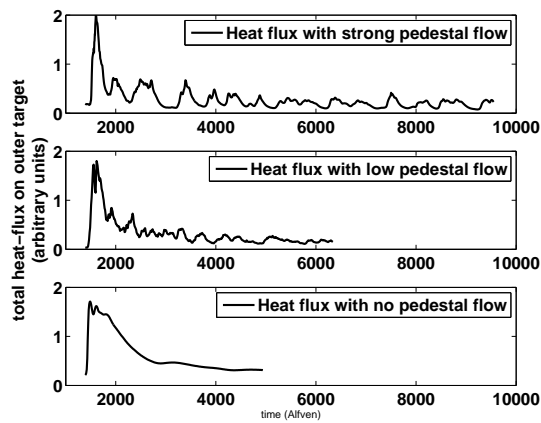
In this paper, we have investigated multiple aspects of the role of poloidal equilibrium flows in ELMs simulations. A first approach of equilibrium poloidal flows has been done assuming the parallel velocity to be zero. In circular geometry, simulations have shown that a thin flow layer forms at the plasma boundary because of the boundary conditions. In fact, the current cannot compensate for the pressure near the boundary, which perturbs the electric potential, thus inducing a poloidal flow. An analytical approach of the reduced resistive MHD equations used in simulations resulted in a formulation of the flow layer thickness as a function of the Hartmann number $\frac{1}{\sqrt{\eta\mu}}$. This result is in good agreement with simulation scans.

A poloidal flow also forms at the pressure gradient in X-point simulations, with a clear $\sin\theta$ dependency. Numerical scaling laws for the flow amplitude have been obtained, but no clear behaviour was found concerning the width of this poloidal flow. Of course, the viscosity and the pedestal width do play an important role, but where one expects to find an influence on the flow width, one finds that the whole structure of the flow is affected. Indeed, long simulations with a progressively collapsing pressure gradient have revealed sharp transitions from an $m=1$ to an $m=0$ flow structure. Parametric studies of this transition were carried out, and simulations were compared to a theory developed by H.R. Strauss that predicts such transitions between different equilibrium flow states for $m=0$ flow structures [4.5]. In particular, the transition is clearly related to the deviation of density from flux surfaces. However, some differences between Strauss' theory and our simulations led to

Figure 39: A poloidal view of the plasma filamentation is shown in figure (a) with and without the equilibrium flow (top and lower row respectively). Figure (b) shows the total heat flux on the outer divertor during a simulations where energy is evacuated periodically from the pedestal (top) and where the flow is not strong enough to produce repetitive bursts (middle row). The lowest row shows the heat flux w=if the equilibrium flow is forced to zero artificially.



(a)



(b)

the conclusion that parallel velocity may play an important role concerning the poloidal flow. This has then been verified with simulations including \vec{v}_{\parallel}

and understood with an analytical derivation : a strong $m=0$ poloidal flow is induced by the parallel velocity together with the deviation of pressure from flux surfaces due to the X-point geometry.

At last, the effects of the equilibrium poloidal flow on ELM stability have been investigated, and simulations have shown that equilibrium rotation may have a significant influence on the linear stability and nonlinear behaviour of ELMs. Linear growth rates are damped, and filamentation of the plasma is reduced. In some cases, the equilibrium flow may be strong enough to regulate the ballooning mode and enable discrete relaxations of the plasma at regular frequency. The fact that the poloidal flow contributes to the stabilization of ballooning modes gives good hope that JOREK may one day be able to produce simulations of L-H transition. But until then, some more efforts are needed.

4 Simulations of ELMs in JET and MAST

4.1 Résumé du chapitre

Le but principal de l'étude étant d'avoir une compréhension avancée de la physique des ELMs dans les tokamaks actuels, il est donc nécessaire de produire des simulations le plus proche possible des conditions expérimentales. Bien que des simulations génériques puissent apporter une connaissance approfondie sur la physique des modes de ballonnements, les conditions expérimentales sont tellement spécifique que le comportement des modes instables peut être radicalement différent dans les simulations, si ces conditions ne sont pas proprement respectées. En d'autres termes, suivant les paramètres physiques (résistivité, viscosité, etc...), la simulation de modes de ballonnement peut soit représenter un crash d'ELM, soit représenter quelque chose de très différent qui ne correspond probablement à aucun phénomène physique observé dans les tokamaks.

Pour reproduire de manière cohérente un plasma expérimental, la meilleure méthode et de simuler un plasma précis, pour une machine donnée, suivant les diagnostics expérimentaux. Les deux machines JET (Joint European Torus) et MAST, situées à Culham, près d'Oxford en Angleterre, ont été choisies comme support pour les simulations. Il y a deux avantages évidents à vouloir simuler ces deux machines. Le premier, c'est que JET est la machine la plus grande au monde à l'heure actuelle, c'est donc la machine la plus proche du futur tokamak ITER. Le deuxième avantage, c'est que MAST est un tokamak dit sphérique, qui a une configuration assez différente des tokamaks classiques comme JET, et donc une physique qui se distingue et qui pourrait apporter une compréhension plus profonde des ELMs. D'autre part, le fait que ces deux machines soient situées géographiquement dans le même centre de recherche apporte de la facilité en ce qui concerne les collaborations engagées avec les expérimentateurs.

Bien que les deux tokamaks JET et MAST soient différents, la méthode utilisée pour reconstruire l'équilibre du plasma dans les simulations est la même. Cette reconstruction est basée sur les diagnostics et des reconstructions d'équilibres qui procurent les profils de pression, le flux magnétique et le courant dans le plasma, en temps réel. Grâce à cela, l'équilibre de Grad-Shafranov est reconstruit dans JOREK, pour des plasmas choisis à des moments bien précis: juste avant les ELMs. De cette manière, il est garanti que les profils de pression seront le plus proche possible du seuil d'instabilité MHD, pour les modes de ballonnements. La stabilité (ou plutôt, l'instabilité) de ces profils est vérifiée par l'utilisation des codes linéaires HELENA et MISHKA. Une fois les équilibres obtenus, les simulations d'ELMs

sont lancées.

La première partie de l'étude concerne la comparaison des résultats de simulations avec les observations expérimentales. Tout d'abord, la filamentation du plasma est étudiée et comparée aux observations expérimentales. En particulier, la taille des filaments, leur composition et leur vitesse sont analysées. Un intérêt important est aussi apporté aux flux d'énergie sur le diverteur. Certaines prédictions poussent à penser que ces mêmes flux pourraient sérieusement endommager le diverteur en Tungstène d'ITER. Les comparaisons avec le diagnostic InfraRouge (IR) montrent que les simulations sont en bon accord avec l'expérience, car non seulement la forme des flux d'énergie est similaire, mais aussi la dynamique (car ces flux se déplacent sur le diverteur). La troisième comparaison est faite sur la taille des ELMs. Notamment, il est montré que le résultat dépend fortement de la résistivité, qui a tendance à faire augmenter l'amplitude des modes. Deux régimes sont analysés (un régime résistif et un régime idéal) et un bon accord est obtenu avec les expériences pour les faibles résistivités.

La deuxième étape concerne les simulations de MAST, qui est accompagnée de comparaisons entre les simulations de MAST avec celles de JET. Il y a un diagnostic sur MAST particulièrement impressionnant, qui peut être facilement comparé aux simulations et apporter une grande compréhension des ELMs: la caméra rapide. Dans les films obtenus, on voit très bien les filaments (dus aux modes de ballonnements) se former au bord du plasma, puis sortir pour heurter le mur du tokamak. Ce genre d'image est facilement reproductible avec les simulations, et apporte une bonne idée sur la structure des filaments. La comparaison entre les simulations de JET et MAST révèlent l'importance de la configuration magnétique, notamment concernant le nombre toroidal des modes, et la quantité de courant dans les filaments.

4.2 Introduction and Motivation

4.2.1 Comparing Simulations and Experiments to Improve the Understanding of ELMs Physics

The simulation of ELMs for specific tokamak plasmas of JET is done aiming at a first, specific goal, which is the comparison of simulation results with experimental observation. This could not only bring confidence to the veracity of the simulations, but it could also bring some further understanding of ELMs physics, both on the experimental side and the numerical side. This comparison thus needs to be focused on the main issues concerning ELMs physics. There are three distinguishable ideas of main interest, namely the

triggering of ELMs and MHD stability, the transport of energy from the pedestal towards the divertor and the vessel walls, and the size of the ELMs as a function of robust plasma characteristics such as collisionality.

The triggering of ELMs is one of the first issues in pedestal physics: although the linear MHD stability of peeling-ballooning modes is well understood, there is growing concern about whether the ELMs are triggered only because the plasma reaches the linear stability limit of peeling-ballooning modes. In fact, recent experimental studies from [Zohm-EPS-2010] have revealed that there could be something else than MHD stability that triggers the ELM, and the pedestal pressure gradient and the current density do not seem to be the only triggers. However, in order to conduct such a study with JOREK, simulations should first be able to reproduce multiple ELMs (ie. type-I ELMy H-mode). Although this is still beyond the capability of the code, there has recently been some significant advances in that field. In particular, two results that stand out. First, as seen in the previous chapter, the way towards multiple ELMs simulations is close, even if the repetitive pedestal crashes shown in that previous chapter are most probably not type-I ELMs. Secondly, as will be seen in this chapter, some simulations of ELMs in near-experimental conditions clearly feature ELM-*precursors*. These precursors are yet too recent a result to be understood, but they bring JOREK still closer to experiments, since ELM-precursors are regularly observed, both in JET and other machines. In future, simulations with ELM precursors could possibly bring further understanding of ELM-triggering, and this result gives further hope that JOREK may indeed be able to produce multiple type-I ELMs simulations, since ELM-precursors are the proof that an ideally unstable plasma may remain above the MHD stability limit without producing an ELM crash. In other words, the MHD stability limits may be crossed without producing steady-state turbulent transport (as in Fig.27 of the previous chapter).

The transport of pedestal energy to the divertor and the vessel walls is a also great concern for ITER. It is already clear, from experimental extrapolations, that ELMs in the future international reactor will set a limit to experimental performances. The main reason for this being that the tungsten divertor might suffer from the heavy heat loads due to ELMs. And there is good agreement within the plasma community that CFCs (which are more resistant than tungsten) cannot be used in a fusion reactor because of the tritium retention and the random redeposition of carbon impurities in the vacuum vessel. Hence, the understanding of heat fluxes on the divertor during ELM crashes should be understood, and the comparison of simulations with the Infra-Red diagnostics has to be undertaken. In particular, what determines the *wetted area* (the radial width of the heat flux profile

on the divertor tiles) and the time duration of the ELMs is of great interest. The understanding of those mechanisms could bring ideas that would help reduce the local power loads by widening this wetted area, or by spreading the heat flux over a longer time period. Apart from this first question stands the relation between heat flux profiles and the filamentation of the pedestal. In some machines, such as JET, the filaments are quite difficult to observe but, as will be seen below, the dynamics of divertor heat fluxes may give an idea of the filaments dynamics, their poloidal and radial speed, and their respective toroidal mode numbers.

The characterization of the ELMs size with respect to plasma collisionality ν^* has been a reference result in ELMs studies for some years now [Loarte-PPCF-2003]. The experimental fact is that the ELM size increases with decreasing collisionality. Just as the power loads on the divertor, this scaling is of great importance concerning ITER, since the future tokamak is expected to operate at even lower collisionality than JET. In fact, it is predicted that large ELMs in ITER could evacuated up 20MJ from the pedestal, which is hardly acceptable for the tungsten divertor. Hence here too, reproducing the collisionality dependence of the ELM size with simulations would not only provide a validation of JOREK, but it could also improve our understanding of some of the main aspects of ELMs physics. Furthermore, such an agreement between simulations and experimental results is a first step towards a coherent extrapolation to ITER using simulations, which can only be obtained if the simulations are validated using robust experimental facts.

4.2.2 Obtain Some General Qualitative Agreement

Now, there is also a more general way of undertaking comparisons between simulations and experiments. This approach focuses more on the global physics of ELMs, which may be seen simply as intriguing physical phenomena. In other words, this way of considering the ELMs does not have a specific aim in terms of immediate fusion needs. In fact, the tokamak, together with all its mysteries, can be considered as a very entertaining physical object. However, although this part of the work may seem entirely idle, it does have a strong purpose. That is, the qualitative validation of simulations. Even if most of these comparisons will not bring any more understanding of how a tokamak may be brought to the ultimate operational scenario, they will show that the simulation results do correspond to ELMs. This is crucial if one wants to make predictions for ITER or future reactors, so the more successful comparisons, the better.

There is in particular one subject concerning the ELMs which is sometimes qualified as *not* ITER-relevant, although many would certainly disagree

about that. This concerns the filamentation of the plasma during an ELM. This is the most basic representation of an ELM, and it should be considered very seriously. Of course compared to ELM-triggering, divertor heat fluxes and ELMs size characterization, the filaments themselves do not represent a direct threat to ITER's performances. Nevertheless, no one may yet predict how much energy the filaments will carry in a device like ITER, and whether they could consequently damage the vessel wall or not. Hence, the filaments should be studied with care, even if some would argue that they 'only look nice' but that they are not relevant for ELMs studies...

As will be seen below, much can be said about filaments from a simulation point of view. On the experimental side however, and in terms of comparisons with simulations, this is not so trivial. In particular, most devices - JET is a good example - do not have that many diagnostics that enable a robust and regular observation of filaments. This was one of the motivations for performing simulations of MAST, as will be presented at the end of the chapter. MAST is equipped with a fast camera that can provide films of the whole tokamak plasma, where filaments can clearly be observed and studied. Again, in terms of ITER-relevant features (especially because MAST is a small aspect ration tokamak, and ITER is not), there is a purpose to such a study that cannot be ignored: the validation of simulations. In fact, although simulations are not yet perfect representations of ELMs, after seeing a comparison of a MAST film with a simulation, where one can see the filament structure, it becomes clear that simulations are very close to reality.

4.2.3 Towards a Quantitative Validation of Simulations

At last, and most importantly, the simulation of real tokamak plasmas should be seen as a first step towards a quantitative validation of simulations. It is the first time that JOREK is confronted to experiments in such a way. And although the simulations achieved in this project give a reasonable qualitative agreement with JET and MAST, the final goal is to carry out such simulations for as wide a range of experimental data bases as possible. As will be seen below, present simulations are done for one specific JET pulse, and one specific MAST pulse. In near future, this needs to be extended to simulations of multiple pulses for both JET and MAST, but also for other machines such as ASDEX UPGRADE and DIII-D. Nevertheless, before undertaking such a project, the simulations of those two JET and MAST shots should be pushed as close to experimental conditions as possible, in order to obtain a robust qualitative agreement with experiments. This agreement has to bring confidence in the simulation results, so as to prove that JOREK may be used extensively for ELMs studies on present tokamaks.

Of course, in sight of performing simulations for a wide range of tokamak pulses, the ideal physical parameters, used in simulations, should first be determined. The main parameters meant here are the resistivity η , the perpendicular diffusivity D_{\perp} and perpendicular conductivity κ_{\perp} , the parallel conductivity κ_{\parallel} , the viscosity μ , and also the poloidal grid resolution. Obviously, most of these parameters may not be taken to the experimental or theoretical values, due to numerical limits in terms of grid resolution, but one should explore those parameters in order to attain plasma conditions as close to experiments as possible. This way, once the ultimate values have been found for the main simulation parameters, one can produce simulations of multiple shots with fixed numerical parameters. Clearly, running simulations for different pulses using different numerical parameters would make no sense. Thus, the present study is carried out not only to obtain a good qualitative agreement with experiments, but also to determine the main plasma parameters to be used when performing a quantitative study. In particular, this is financially essential, since such a quantitative study will certainly be very costly in terms of CPU hours.

As a first step towards this goal, collisionality scans are carried out for different values of resistivity. The reasons for choosing this specific method are the following. First of all, the collisionality scan obtained by Loarte [ref.] is the most robust experimental fact yet obtained for type-I ELMs. Hence, it gives a strong reference for the qualification of simulations performances. Furthermore, this combines the present goal with the objective detailed above, concerning the ELMs size and extrapolation to ITER... killing two birds with one stone (some could argue that birds are not ITER-relevant anyway...). In addition, it is known that resistivity is a crucial parameter in terms of MHD stability, so that before trying to optimize all other parameters, resistivity should first be taken as low as possible.

4.3 JET Simulations

4.3.1 Reconstruction of the JET Equilibrium

The Jet pulse #73569 has been chosen to produce simulations for three reasons. First of all it is a standard, regular type-I ELMy H-mode pulse, with an ELM frequency and ELMs size that stay rather constant along time. Thus the various ELM properties (ELM size, ELM-affected area, divertor heat-fluxes, time-scales etc) corresponding to that specific plasma can be averaged over the pulse, and thus well identified. Secondly, this pulse has good electron temperature and density profiles from the HRTS diagnostic (High Resolution Thomson Scattering), with enough profiles before the ELMs to be

combined in order to obtain a good pedestal resolution. Combining multiple profiles from the same shot is a technique used to obtain a better pedestal resolution [ref.Beurskens]. As explained in the previous chapter, for simulations, it is important to have a reliable pressure profile in the pedestal region, since it plays one of the main roles in ballooning stability. Fig.40a shows the density and temperature profiles from HRTS data. Also, having a good quantity of profiles along the shot ensures that enough profiles may be found right after the ELM crash, so that the ELM size and ELM-affected area are known, which is important if simulation results have to be compared to experiments. The third and last point is that pulse #73569 has the correct magnetic configuration for the InfraRed camera to have a good view over tile 5 of the outer divertor, in order to obtain comparisons of the divertor heat flux profiles. Fig.40b shows the time trace of the pulse with the D_α signal, the total NBI power and the total plasma pressure. The principal characteristics of the shot are the following,

1. Ellipticity : 1.67
2. Upper triangularity : 0.17
3. Poloidal Beta : 0.66
4. Toroidal Beta : 2.2%
5. Magnetic field : 2T
6. Total plasma current : 2.2MA
7. Total NBI injected power : 12.5MW
8. Pedestal temperature : 0.9keV
9. Pedestal density : 5.10^{19}m^{-3}
10. Edge safety factor q_{95} : 3

Reproducing a plasma equilibrium requires 3 ingredients, as inputs to the Grad-Shafranov equation: the pressure profile, the current profile, and a ψ -contour around the plasma. The pressure profile is obtained using the HRTS profiles for n_e and T_e , with a fit of the data from the function generally used in simulation for density and temperature profiles, as shown in equation (161). The resulting fit is shown in Fig.40a. Next, the global current profile is obtained from the EFIT equilibrium reconstruction, together with the additional bootstrap current, calculated from HELENA, according to the

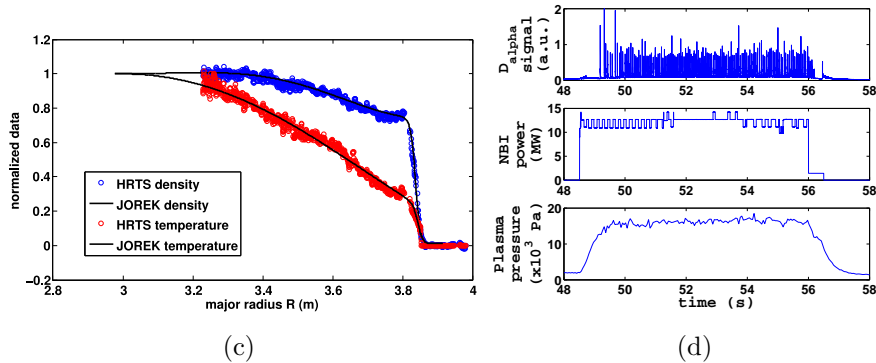


Figure 40: a). The density and temperature profiles from HRTS for the JET pulse, with the corresponding profiles reproduced for simulations. b). The time trace of the JET pulse reproduced, showing the D_{α} emission, the NBI injected power and the total plasma pressure.

corresponding HRTS pressure profiles (note that the HELENA code uses the *Sauter* method to calculate the bootstrap current [Sauter]). Finally the ψ -contour around the plasma, obtained from the EFIT reconstruction as well, is used as a boundary condition to solve the poloidal magnetic flux ψ from the Grad-Shafranov equation. This ψ -contour is taken around the plasma, just outside the vacuum vessel wall, so that the width of the SOL is in good agreement with the JET tokamak. The flux ψ resulting from the equilibrium reproduction in JOREK can be seen in Fig.41, where it is compared with the flux from EFIT.

With this reconstructed equilibrium, it is now necessary to check whether the pedestal pressure profile is linearly unstable with respect to ballooning modes. The code HELENA is run for this equilibrium, and the result is shown in Fig.42a. However, one should bear in mind what was first stated in Chapter 3, namely that some non-ideal plasma parameters (mainly η and μ) can have a strong influence on the linear stability of ballooning modes. Hence, although it is now verified that the equilibrium is linearly unstable with respect to ballooning modes, it will be seen below that some stable cases of ballooning modes can still be obtained. For example, as seen from Fig.25, if resistivity is low and viscosity high, the modes may be stabilized. Fig.42b shows the same scan with resistivity and viscosity for the ballooning mode number $n = 12$. The effect of the parameters is still seen but not as strong as in the case presented in the previous chapter, which suggests that the linear stability of the JET equilibrium is principally determined by the pressure gradient. On the other hand, this does not mean that the equilibrium is highly unstable. For example, in the resistivity scan, the mode $n = 12$ is

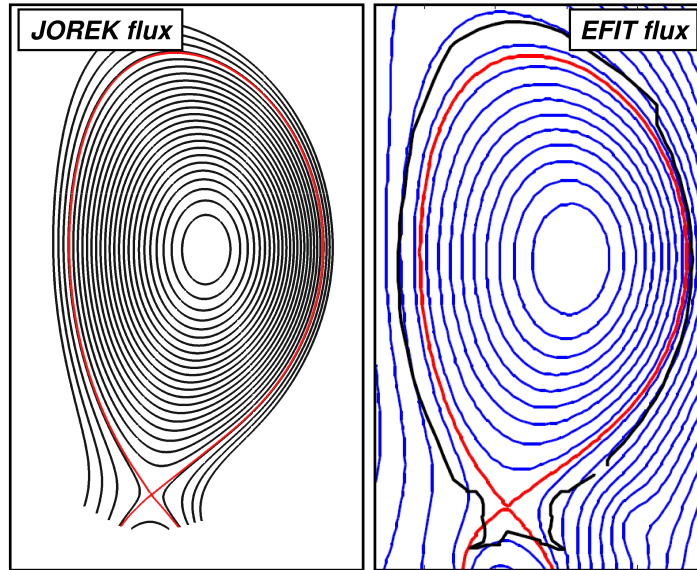
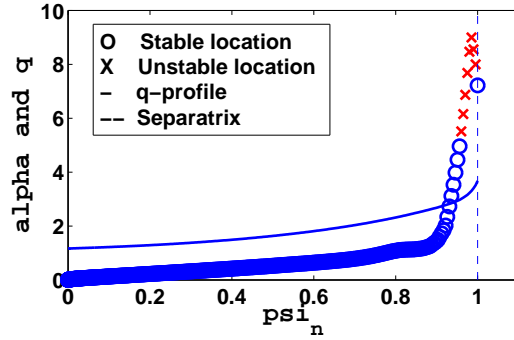


Figure 41: *The reproduction of the Grad-Shafranov equilibrium with JOREK, and the comparison with the EFIT equilibrium reconstruction.*

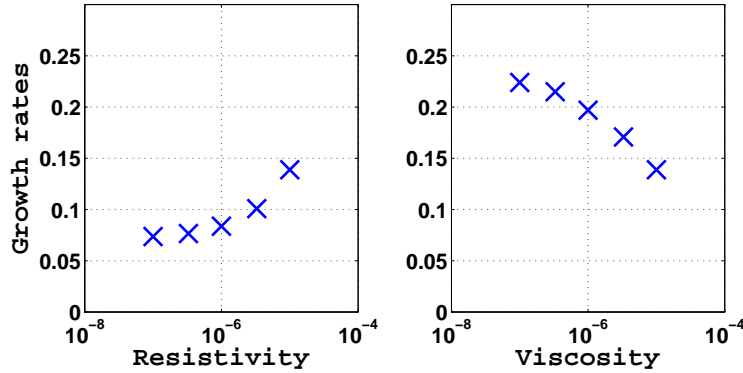
stable already at $\eta = 10^{-8}$. Although this resistivity is still higher than the theoretical Spitzer value, if viscosity is brought down to a more reasonable value, the mode becomes unstable again.

Hence, simulations of ballooning modes are balanced between numerical limits on one side, which sets bounds to the minimal values allowed for plasma parameters (in particular η and μ), and the linear stability of the modes on the other, which has to be reasonable. In fact, this balance is quite delicate, and a good example to see this is the following. Say a given simulation fails because resistivity is too low, and the grid is not refined enough to solve the fine current structures. Then, considering the grid cannot be refined further because of CPU memory, in order to avoid the problem, one needs to set η to a higher value. But by doing this, the growth rate of the ballooning mode is increased, and the resulting simulation may indeed fail even more. Likewise, the opposite situation can be encountered, if a given ballooning mode is stable: one way to make the mode more unstable, while going towards more experimental conditions, is to set viscosity or diffusivity to a lower value, but then one may reach numerical limits if the grid is not refined enough.

It also turns out that the JET equilibrium exhibits a very strong poloidal rotation. Fig.43a shows the poloidal velocity with the corresponding flow shear, and the density gradient to show that the flow is localised in the pedestal region, at the pressure gradient. The effect of this rotation on



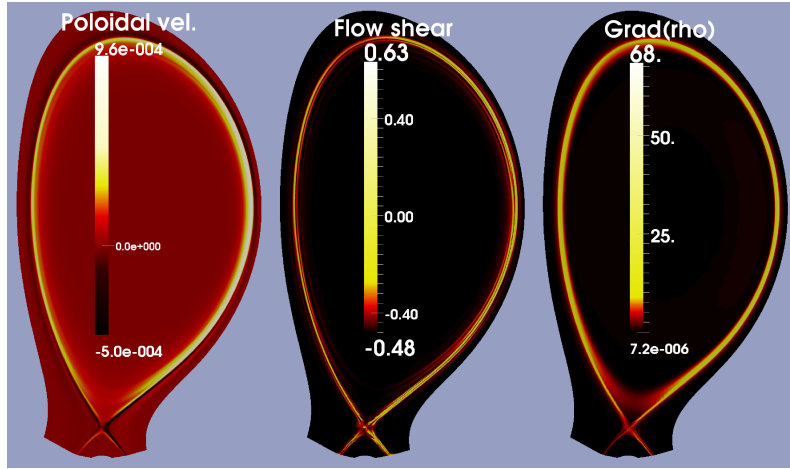
(a)



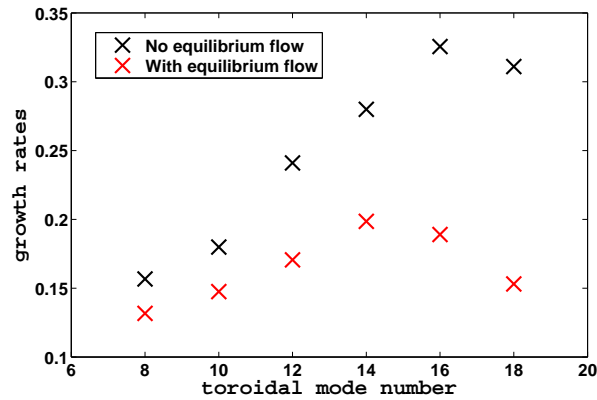
(b)

Figure 42: a). The linear stability of the reconstructed JET equilibrium with respect to ballooning modes, as calculated from HELENA. The pressure gradient parameter α is plotted as a function of ψ_n , together with the q -profile. The locations where the pressure gradient is unstable are marked by red crosses. b). The growth rates of the mode $n = 12$ as a function of resistivity and viscosity.

the linear growth rates of ballooning modes is calculated as in Chapter 3, for different mode numbers. Simulations are run normally, and then run again from the same equilibrium, but forcing the equilibrium flow to zero at each time step. The resulting growth rates are shown in Fig.43b, where the stabilizing effect of the flow is shown to increase with the mode number. It is also important at this stage to note that, referring to this scan, the most unstable mode number is $n = 14$. Hence, for the JET equilibrium, simulations will usually be run with mode numbers between $n = 8$ and $n = 20$.



(a)



(b)

Figure 43: a). The equilibrium poloidal velocity of the JET simulation, together with the corresponding flow shear, and the density gradient. b). The effect of the equilibrium poloidal flow on the growth rates of ballooning modes.

4.3.2 Filamentation of the pedestal

One of the main characteristics of ballooning modes (ELMs) is that they produce a filamentation of the pedestal pressure. At the edge of the plasma, just inside the separatrix, the mode starts to perturb the density and the temperature to form tubes aligned to the magnetic field. These filaments then cross the separatrix and this way pressure is evacuated from the plasma core into the SOL. The dynamics of filaments varies strongly from case to case, but some generic features can be classified: the radial and poloidal size of the filaments, their speed, their composition, and the role they play

concerning heat fluxes on the first vessel wall. Fig.44 shows a zoom on a filament crossing the separatrix.

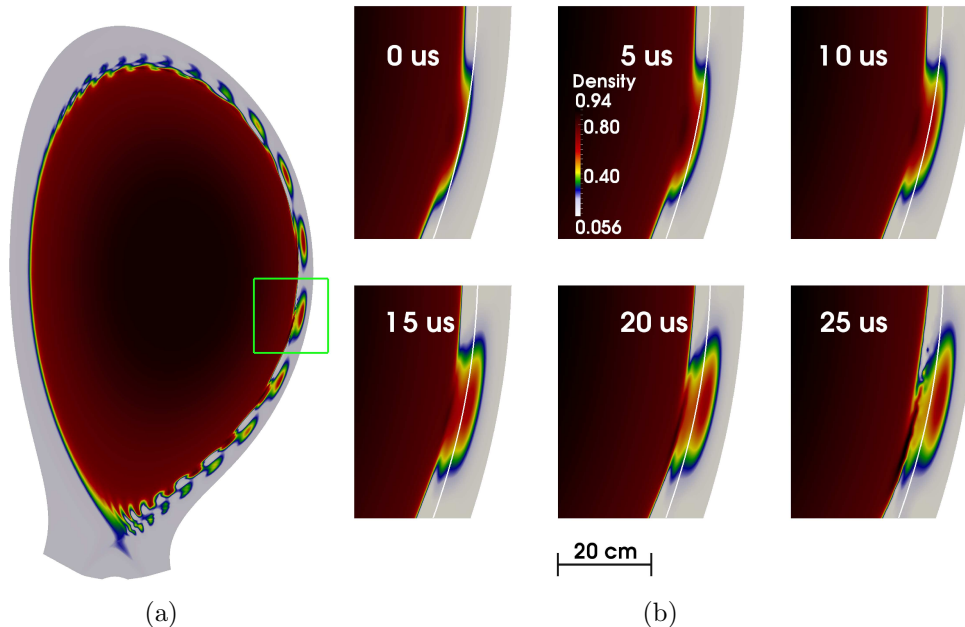


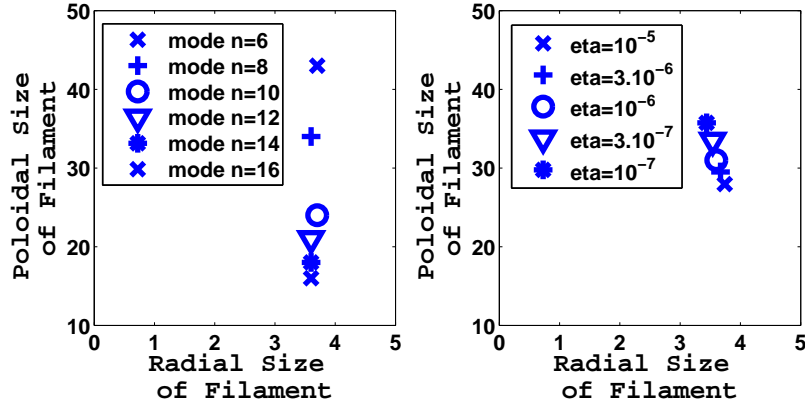
Figure 44: *A zoom on a filament at it crosses the separatrix. Filaments do not always fully cross the separatrix. If the growth rate is not high enough, filaments may remain attached to the main plasma core (see Fig.45b). Cases where filaments do cross the separatrix usually lead to a large pedestal collapse.*

The size of the filaments changes with the toroidal mode number. More precisely, the poloidal size changes, but the radial size does not. The radial size of filaments appears to be closely related to the pressure gradient. As can be seen on Fig.45a, the radial width does not change at all from one mode to the other, and corresponds exactly to the width of the pressure gradient. This has been verified with other simulations, such as the cases presented in the previous chapter, which had different geometries and different pedestal pressure gradient widths. However, one should bear in mind that the fact that filaments always have the same radial width does not mean that they result in the same energy losses. For example, filaments may or may not cross the separatrix, depending on growth rates; and also, the equilibrium flow has more influence on higher n -modes (both linearly and non-linearly). Concerning the poloidal width of filaments, due to the $1/R$ dependency of the toroidal magnetic, the ratio B_ϕ/B_θ is much lower on the low field side, so that filaments are larger on the LFS than on the HFS. Fig.45 shows the poloidal size of the biggest filament (that nearer angle $\theta = 0$) for different

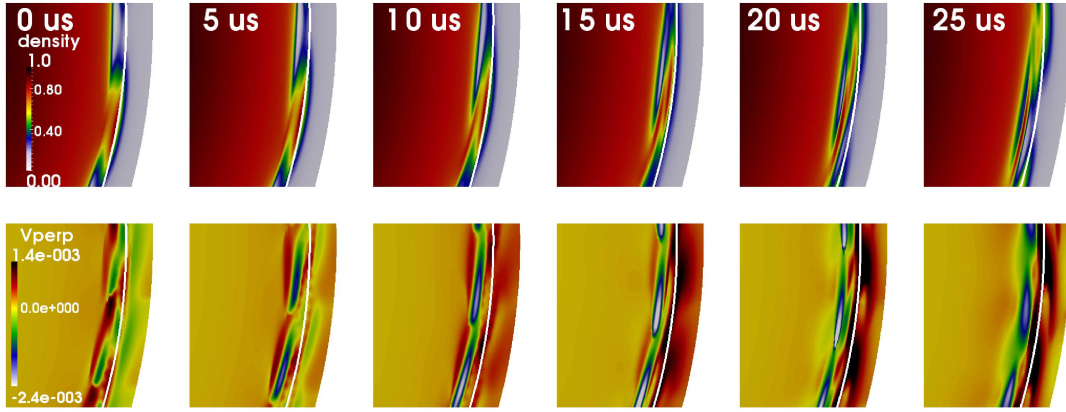
mode numbers. A scan in resistivity was done for the mode number $n = 12$. Recall that η has a strong influence on the growth rates of ballooning modes, as shown in Fig.25, which is one reason why interest is focused on the η -scan: to obtain a relation to growth rates. The resulting effect on the size of the filaments is that the amplitude of the mode (its growth rate) does not have a direct influence on either the poloidal nor the radial size of filaments. Nevertheless, and again, this does not mean that the energy evacuated by the filaments is the same for all resistivities. However, due to the strong poloidal equilibrium flow, the filaments are sheared along the poloidal direction. For a violent instability, with high a growth rate, the filaments will cross the separatrix and then their *tail* is cut by the sheared flow. This cutting can be seen on Fig.44. If the instability is not so violent however, the filament may remain closer to the separatrix, in which case the flow shears off the filament, as seen on Fig.45b. The zoom in Fig.44 is the $\eta = 10^{-5}$ case and Fig.45b is the $\eta = 10^{-7}$ case.

Thus, the equilibrium poloidal rotation may have a strong effect on filaments, as seen in the previous chapter. In fact, in most cases, filaments move not only radially, but also poloidally. There are two typical situations which may be distinguished. The first one is when filaments start moving poloidally at the same time as they cross the separatrix. An example of this poloidal rotation of filaments is shown in Fig.46a. This is in good agreement with experimental observations on ASDEX UPGRADE, with the ECEI (Electron Cyclotron Emission Imaging diagnostic) [Boom, EPS-2010], which clearly shows filaments travelling poloidally as they cross the separatrix. The second case is when filaments first start moving poloidally, before crossing the separatrix, and then stop rotating when moving into the SOL. This has also well been observed with fast cameras, mainly on MAST [Kirk, ITPA-2006]. This phenomenon usually corresponds to an ELM precursor, since only a small amount of energy is lost then, compared to the ELM crash that follows. This is observed only in simulations of ELMs at very low resistivity. Fig.46b shows the divertor heat flux for such a simulation, where the precursor can clearly be identified, lasting about $150\mu s$, which is almost as long as the ELM crash itself. Concerning the radial speed of filaments, it is rather delicate to give any detailed quantification. There is a clear relation between the growth rates of ballooning modes and the distance traveled by the filaments: violent modes have filaments that really detach from the main plasma into the SOL, while weaker modes have filaments that never entirely cross the separatrix. Despite this, there is no clear difference of speed from one case to the other. It appears that the radial speed of filaments in simulations is always close to $2\text{km} \cdot \text{s}^{-1}$.

The composition of filaments is also relatively complex to determine. As



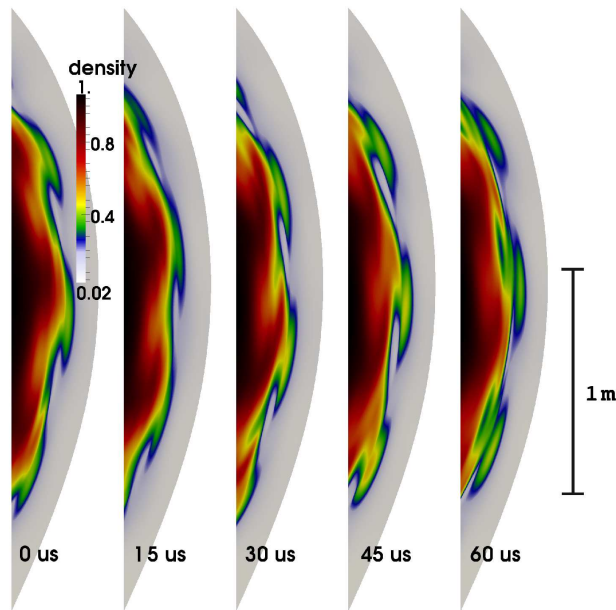
(a)



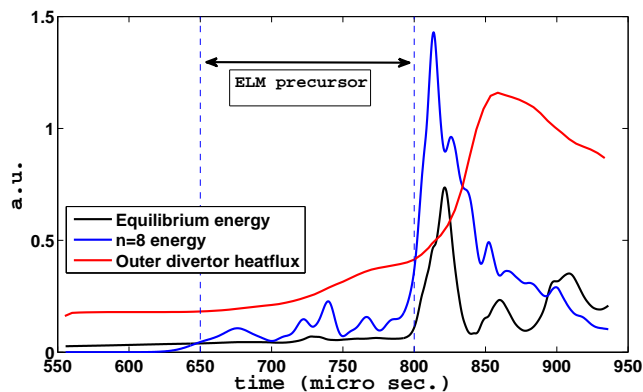
(b)

Figure 45: a). The radial and poloidal size of filaments for different mode numbers (left) and for different values of η (right) - recall that η strongly influences the growth rates of MHD modes. The units in both graphs are cm. b). A zoom on a filament that does not fully cross the separatrix (case $\eta = 10^{-7}$). Top row shows the density, and bottom row shows the poloidal flow. The filament is sheared off by the poloidal equilibrium flow, because the growth rate of the mode is too small. This shearing explains the effect of growth rates on the poloidal size of filaments, as seen from the η -scan in Fig.a

a convention here, a filament is defined by a tube of density aligned to the magnetic field, so all other compositions of the filaments will be compared to density. The most convenient way to make these comparisons is by taking radial profiles of filaments, as is done with the HRTS diagnostic. There are other ways to describe the composition of filaments, with 0D, 2D and 3D plots, but 2D and 3D descriptions are rather inconvenient (too large figures) and do not necessarily provide the radial precision that is obtained



(a)



(b)

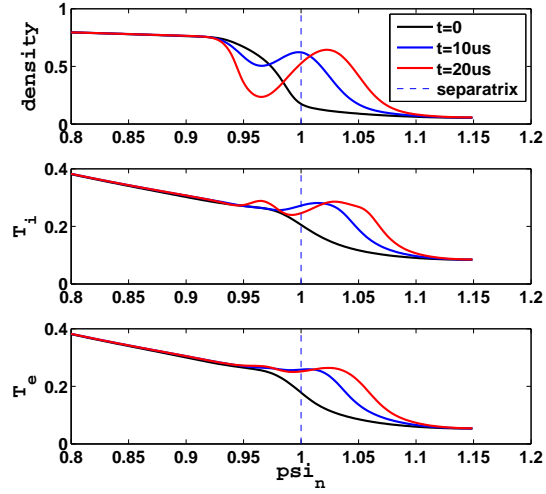
Figure 46: *a). The poloidal rotation of filaments is usually observed in simulations. This example shows time slices of density filaments on the LFS of the plasma. The rotation corresponds to about $10 \text{ km} \cdot \text{s}^{-1}$. b). In certain cases, ELM precursor are observed. Here, the precursor lasts about $150 \mu\text{s}$, before the ELM crash arrives. During all this precursor period, filaments rotate poloidally inside the separatrix. When the crash arrives, the poloidal rotation decreases and the filaments start crossing the last closed flux surface. Shown on the picture is the kinetic energy (equilibrium energy), and the energy of the ballooning mode perturbation $n = 8$, together with the total heat flux on the outer divertor. Units are arbitrary.*

with 1D profiles. On the other hand, 0D measures (like fixed probes in the plasma) do not provide enough information for a clear description. First, it should first be pointed out that the filaments are warm, in particular warm with ion temperature. The electron temperature is rapidly evacuated by parallel conduction, and the resulting profiles are less distinct for T_e than T_i . Fig.47a shows density, T_i and T_e profiles for three time slices as the filament comes out through the separatrix. It can be seen that a well of density is formed between the filament and the main plasma. This is observed in JET for n_e , with the HRTS diagnostic [Beurskens-PPCF-2009]. Also, a different behaviour is observed between the density, T_i , and T_e . In particular, the *front* (as in wave front) of the filament is cold from T_e , while the *tail* of the filament is warm. This matches the HRTS profiles, as shown in [Beurskens-2009]. On the other hand, this advancing front is much warmer with T_i , due to lower $\kappa_{\parallel,i}$. This cannot be compared to experiments yet, since only T_e profiles are available. Fig.47b shows the difference between the T_i front and the T_e front at the three time slices. Thus, the temperatures and the density are always more or less *in phase*, except for the front, which is warmer with T_i than T_e . This is not the case for current. There is rather a large amount of current escaping from the pedestal, and the current filament is always first to cross the separatrix, with its maximum at the pressure gradient of the filament, which comes from the balance $\nabla p = \mathbf{J} \times \mathbf{B}$. This is illustrated in Fig.48, where the density and current profiles are given for three levels of resistivity. It can be seen that the current filament increases as resistivity is taken towards more experimental values, even if the growth rate is weaker.

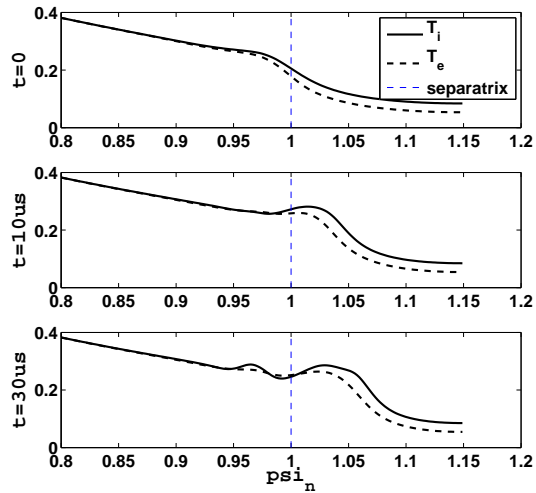
At last, it should be noted that multiple sets of filaments are ejected from the plasma during an ELM. As explained in the previous section, high resistivity usually enhances the ballooning modes, so that in those cases, filaments are formed repetitively. However, even at low resistivity, many sets of filaments are ejected. In general, the new filaments start appearing behind the separatrix as soon as the previous set has been ejected.

4.3.3 Divertor Heat Fluxes

Thus, in simulations filaments are warm with ion temperature, and they may carry a large amount of energy into the SOL, and possibly to where the first vessel wall of JET stands. However, the ballooning mode perturbation acts on the magnetic field, so that an ergodization of the separatrix occurs, and temperature is rapidly transported along the magnetic field towards the divertor, in particular T_e . This mechanism brings a consequent part of the energy losses to the divertor. This, together with the parallel convection of density and temperatures, results in large heat fluxes near the divertor strike



(a)



(b)

Figure 47: a). Radial profiles of a filament crossing the separatrix. Shown are the density, T_i and T_e for three successive time slices. This simulation is the case $\eta = 10^{-5}$ - the one with highest growth rate. b). The same radial profiles of T_i and T_e for the three time slices. The filaments are warmer with T_i than T_e , which is rapidly evacuated along the magnetic field by parallel conduction.

points. Temperature is conducted via κ_{\parallel} in such a way that mostly T_e arrives at the divertor. T_i is also conducted to the divertor, but less rapidly, and whereas fine structures are observed for T_e on the divertor, it is not the case for T_i . Fig.49 shows time slices of both temperatures near the outer divertor,

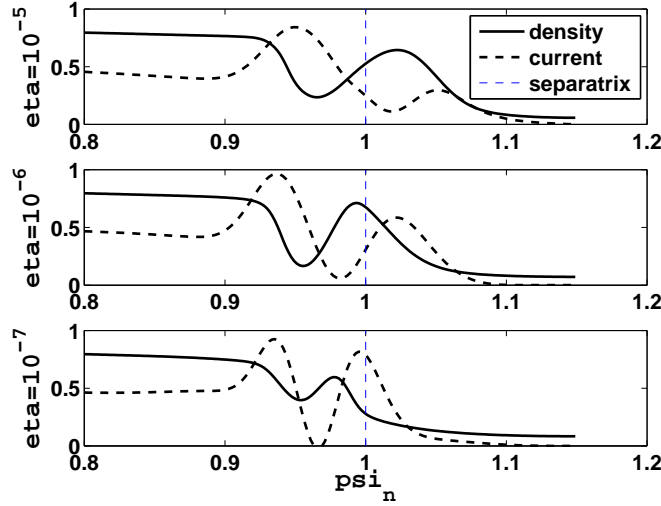


Figure 48: Radial profiles of density and current, after the filament is formed, for three different values of η . The current as its maximum at the pressure gradient.

at the beginning of an ELM crash. The same color scaling is used for both temperatures, so as to show that T_e plays the major role in divertor heat fluxes. Such structures near the strike point - let us define them as *stripes* - are also observed in JET with the Infra-Red camera, which has a view on Tile 5 of the outer divertor. Fig.50 shows the magnetic configuration of JET with the strike point on Tile 5, together with an example of heat flux stripes during an ELM. It should also be noted that it has already been verified that the heat-flux stripes on the divertor correspond to the perturbation of the magnetic field [Huysmans-EPS-2009]. In fact, due to the fast parallel conductivity of (electron) temperature, if the magnetic field is perturbed, then temperature will match this perturbation.

However, it should be pointed out that in simulations the heat flux itself does not always exhibit stripes near the strike point, even when T_e does. The heat flux on the divertor is defined by

$$\mathbf{v}_{\parallel} \rho (T_i + T_e) \cdot \mathbf{n}, \quad (196)$$

where \mathbf{n} is the normal unit to the divertor,

$$\mathbf{n} = \pm \frac{\nabla\psi \times \nabla\phi}{|\nabla\psi \times \nabla\phi|}. \quad (197)$$

The plus/minus signs are for inner/outer divertor. It follows that the total heat flux profiles partly depend on the \mathbf{v}_{\parallel} and ρ profiles. The parallel velocity

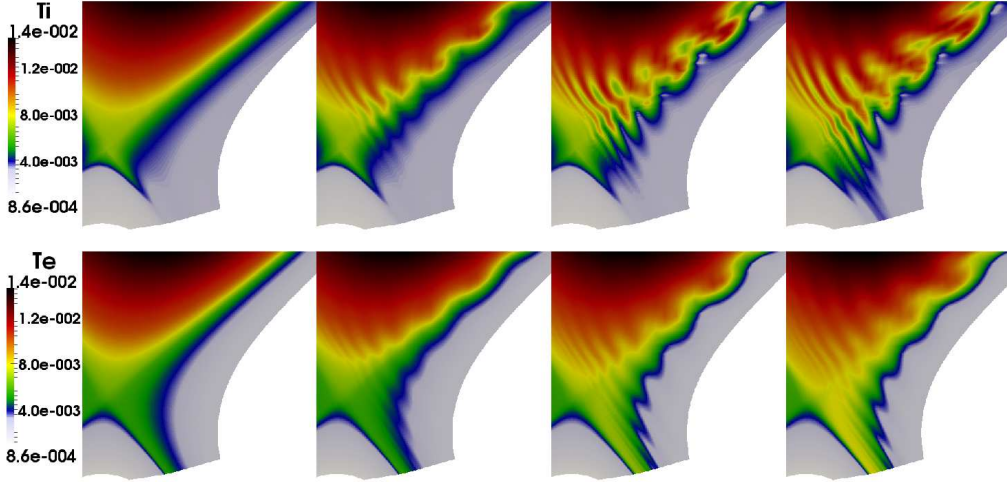


Figure 49: *The ion and electron temperatures near the divertor at the beginning of an ELM simulation. T_e arrives rapidly to the divertor, with fine structures near the strike point. With weaker parallel conductivity, T_i does not reach the divertor so quickly.*

at the target is related to $\sqrt{T_e}$ via the Bohm boundary conditions (133), so that strong stripes in T_e may provoke small stripes of v_{\parallel} on the divertor. Density however, is convected to the divertor, so that heat flux stripes may be caused by convection of energy, conduction, or both. As seen previously, by changing resistivity, one may vary the growth rates of ballooning modes, which plays a major role in the intensity of the resulting pedestal crash. The first effect of growth rates, illustrated in the previous section, was that filaments would reach further into the SOL with a high growth rate, leading to larger energy losses. Here this effect is clearly identified with the divertor heat flux. Fig.51a shows the maximum total heatflux on the outer divertor during the crash, for three values of η . The toroidal mode number for these simulations is $n = 12$. The three major effects demonstrated by this figure are that, with increasing growth rates, the total heat flux (the ELM size) increases, the wetted area increases, and the stripes become more distinct.

The toroidal mode number is another parameter that may have a significant effect on the heatflux profiles. As shown in Fig.51b, the number of stripes appearing on the divertor heatflux increases with increasing mode number. That is, if the plasma conditions are identical. This may prove useful in future, given that simulations could reproduce type-I ELMs with reasonable accuracy, since comparing simulations with Infra Red camera observations could help determine the dominant mode numbers of ELMs during experiments.

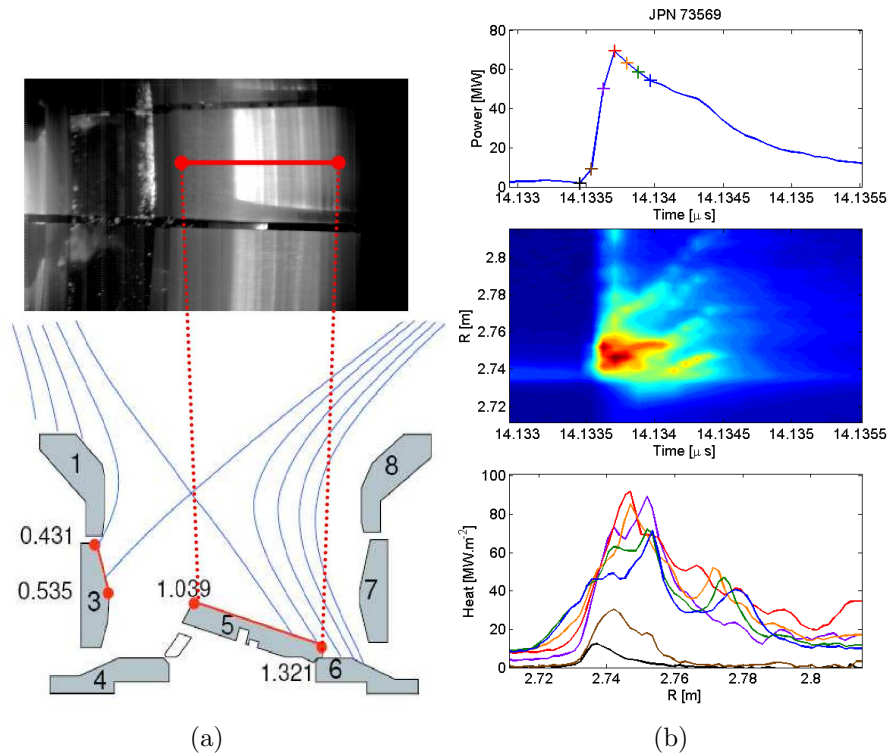


Figure 50: a). The magnetic configuration of pulse #73569 with the outer strike point on Tile 5. b). The heat flux during an ELM of pulse #73569, with stripes near the strike point. Note the time units should be seconds, not μs (thanks to the JET graphics team!).

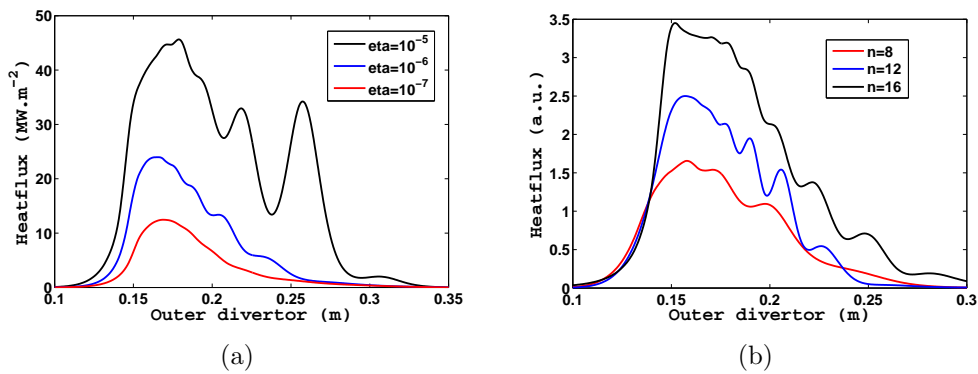


Figure 51: a). Heatflux profiles on the outer divertor target for three different values of resistivity. The toroidal mode number for these simulations is $n = 12$, and the profiles are taken at the maximum of the total heatflux. b). Heatflux profiles for different toroidal mode numbers, showing that the number of stripes on the divertor is closely related to the mode number.

Seen from a more global point of view, simulations can be compared to the heatflux observed by the wide angle Infra Red camera. For the mode n , n stripes will result on the divertor during an ELM, as seen on Fig.52a for the mode $n = 8$. The same divertor heatflux is shown in Fig.52b, stretched out to equal scales for the toroidal and radial directions, which gives a more realistic geometry of the heatflux. In experiments, both with the fast camera and the Infra Red camera, these stripes are observed to move radially, away from the strike point. This is illustrated in Fig.53a, where the heatflux profile on the outer divertor is plotted as a function of time. A similar dynamics is observed in some simulations, but although it is clearly observed for the T_e stripes, the corresponding total heatflux does not exhibit such behaviour. Fig.53b shows the total heatflux and the T_e stripes on the divertor as a function of time.

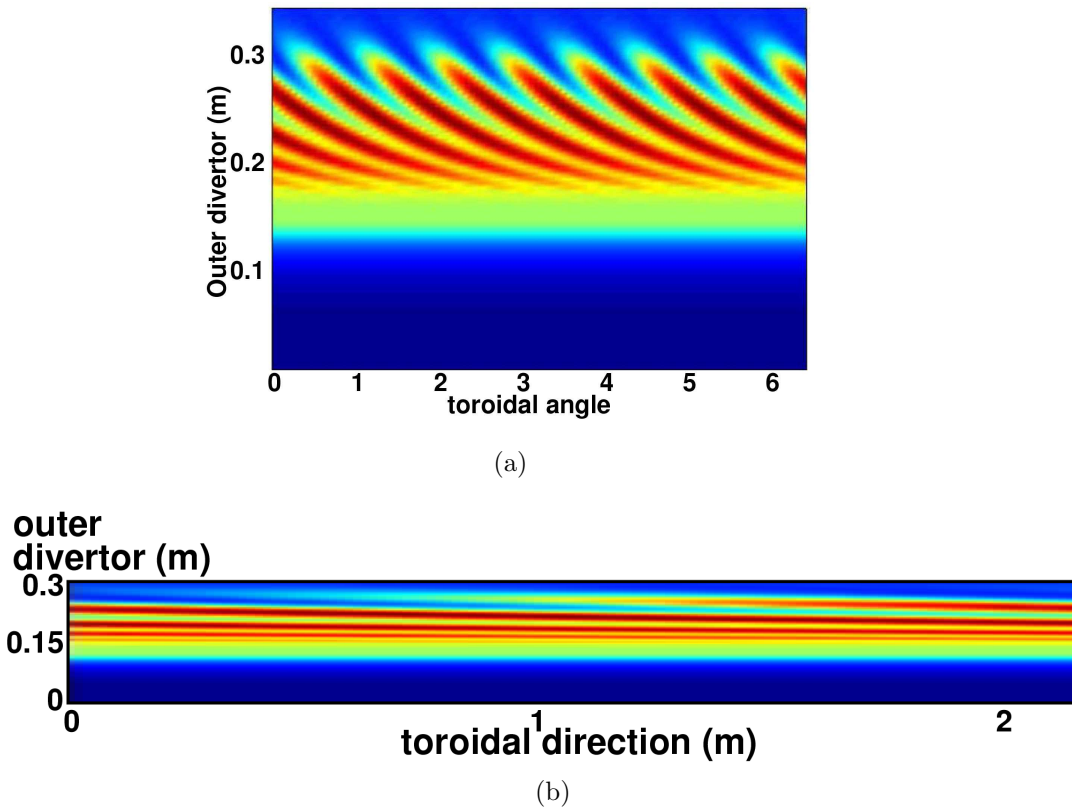
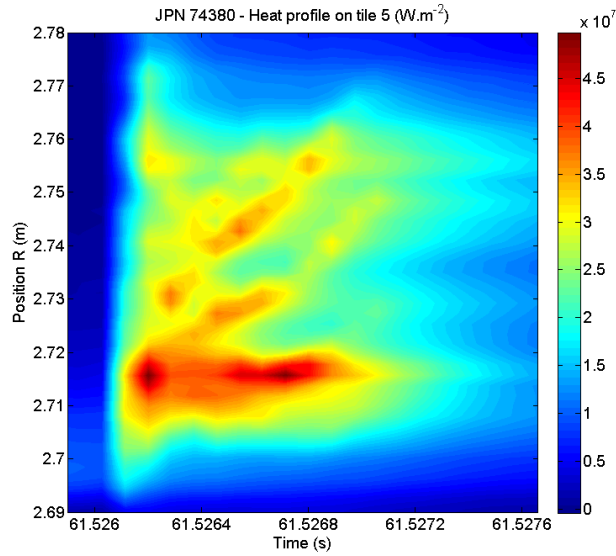
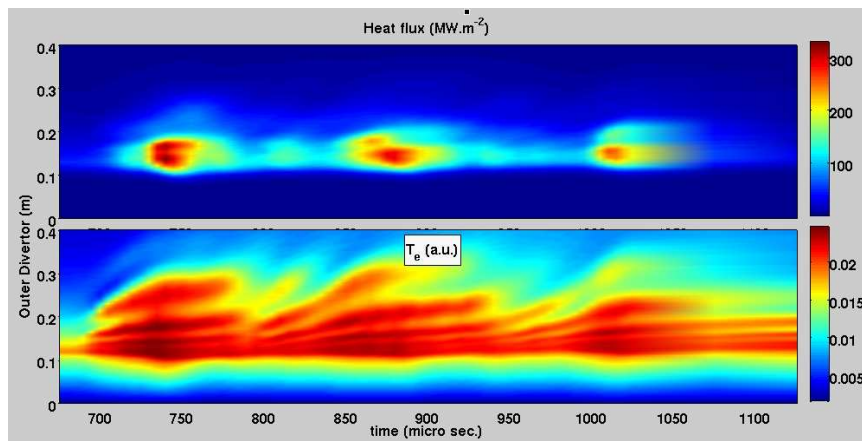


Figure 52: *a). Finger-like footprints of the heatflux on the whole divertor. For the mode $n = 8$, 8 fingers are observed on the divertor. b). Stretched out so that the toroidal and radial length-scale are equal, the divertor heatflux can be compared to observations of the wide angle Infra Red camera of JET.*

However, even if the heatflux dynamics observed in experiments is reproduced here only for T_e , there is one important feature to emphasize: the



(a)



(b)

Figure 53: *a). Heatflux stripes are often observed to move away from the strike point during ELM crashes in JET. b). In simulations, this is sometimes observed for T_e stripes in simulations, although the total heatflux itself does not exhibit the same behaviour.*

movement of heatflux stripes on the divertor is directly connected to the poloidal rotation of filaments. As seen previously in Fig.46a, filaments sometimes move poloidally. This poloidal rotation may be positive or negative (ie. the filaments can turn clockwise or anti-clockwise). As a demonstration, Fig.54 shows T_e stripes on the divertor moving in the opposite direction as in Fig.53b. One simple, convincing way of explaining the relation between the

rotation of the filaments and the heat-flux dynamics relies on Fig.52. In fact, a poloidal rotation of the filaments is equivalent to a toroidal rotation, and since the n stripes on the divertor correspond to the n filaments, if the filaments rotate toroidally, then so will the stripes. This not only shows that the heatflux dynamics is related to the poloidal (toroidal) rotation of filaments, but it also means that filaments in JET should be expected to have a strong rotation, since the divertor heat-flux dynamics is regularly observed. In addition, it has yet never been observed experimentally that heatflux stripes moved innwards, towards the strike point, which suggests that the filaments always rotate in the same direction (anti-clockwise in the poloidal plane). However, the fact that heat-flux stripes in JET are regularly observed to move away from the strike point could be a consequence of the toroidal rotation induced by NBI injection. MAST for example, which relies mainly on NBI heating, has filaments which are seen to rotate rapidly (fast camera films), and at the same time, the heatflux stripes on the outer divertor are observed to have a very active dynamics.

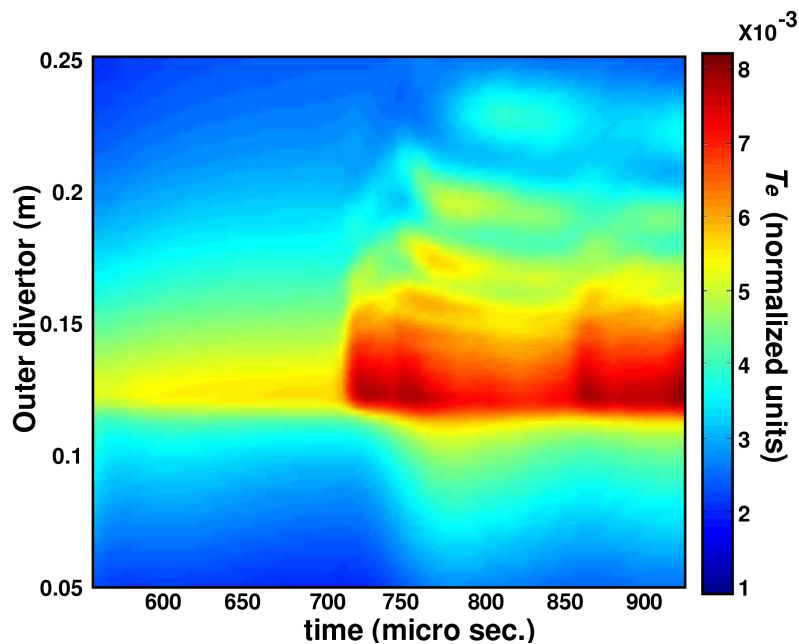
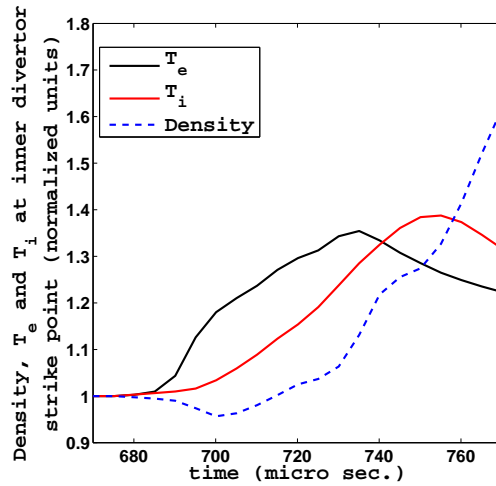


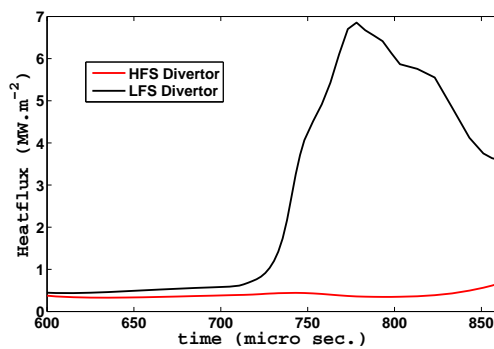
Figure 54: *The dynamics of heatflux stripes is a consequence of the poloidal (or equivalently toroidal) rotation of filaments, so that if filaments rotate clockwise in the poloidal plane, the heatflux structures are observed to move innwards, towards the strike point.*

Another aspect of simulations which may be compared to experimental observations is the delay between electron and ion energies as they arrive on the inner divertor. Experimentally, this is measured using the the D_α

emission (for ions) and the X-ray Bremsstrahlung (for electrons) diagnostics [Loarte-POP-2004]. Fig.55a shows the ion and electron temperatures at the inner strike point in a simulation where the delay can clearly be seen. However, the delay measured in simulations is much shorter than that measured in experiments, almost a factor 10. This difference is strengthened by the fact that simulations usually show that most of the energy lost during a the crash arrives on the outer divertor, whereas in experiments, energy is deposited equally on both divertors, if not more on the inner one. An extreme case of such a situation is shown in Fig.55b, where the total heatflux on the outer divertor is plotted together with the heatflux arriving on the inner divertor.



(a)



(b)

Figure 55: a). The delay between the ion energy and the electron energy arriving on the inner divertor. Both T_e and T_i are measured at the strike point to exhibit this behaviour. b). In the most extreme cases, all the energy evacuated by the ballooning mode arrives on the outer divertor.

4.3.4 ELM size

Up to now, all simulations were made with non-realistic plasma conditions. In particular, the resistivity was brought down to 10^{-7} , but not more. The grid refinement was the main reason for this, because in order to produce simulations with low η , one needs to have enough resolution to solve the thin current structures that are formed during the ELM crash. This is also true for all other parameters, in particular viscosity and mass perpendicular diffusivity, but as was seen previously, resistivity is the only parameter that has a boosting effect on ballooning growth rates - all other parameters have a damping effect. Hence, in sight of bringing simulations as close to real experimental plasma conditions, bringing resistivity as low as possible (for a given grid) was the first goal.

In order to obtain simulations with low resistivity, a grid of 22 000 nodes was used, which is about twice the size of the grid for the simulations presented previously. Simulations with such a grid would not have been possible without the starting of the HPC-FF cluster in Juelich. Even there, such simulations, with only one $n \neq 0$ toroidal mode number, a minimum of 512 processors were needed, for at least 2 days per ELM crash, and up to 5 days for difficult (highly nonlinear) simulations. Thus, about 25 000 CPU hours were needed for each simulations.

As was stated earlier, the most reliable experimental classification of ELM size is that of A. Loarte [Loarte-PPCF-2003], concerning the relation between the ELM size and collisionality ν^* . Therefore, it was decided that simulations should use the same approach and that collisionality should be varied. The simplest way of obtaining a collisionality scan in JOREK is to vary the density ρ_o . Note that by doing this, since temperature is normalized with as $T = \bar{T}/\mu_o\rho_o$, the total (real) plasma pressure remains unchanged, so that the ballooning mode stability of the plasma does not change. Varying ρ_o thus means that all normalized plasma parameters should be varied accordingly. Those parameters are the following, with their relation to ρ_o , and the corresponding relation to collisionality, assuming from the Spitzer collisionality

that $\nu^* \sim \rho/T^2$,

$$D_{\perp} \sim \rho_o^{\frac{1}{2}} \sim \nu^{*\frac{1}{6}}, \quad (198)$$

$$\mu \sim \rho_o^{-\frac{1}{2}} \sim \nu^{*-\frac{1}{6}}, \quad (199)$$

$$\mu_{\parallel} \sim \rho_o^{-\frac{1}{2}} \sim \nu^{*-\frac{1}{6}}, \quad (200)$$

$$\eta \sim \rho_o^{\frac{1}{2}} \sim \nu^{*\frac{1}{6}}, \quad (201)$$

$$\kappa_{\perp} \sim \rho_o^{-\frac{1}{2}} \sim \nu^{*-\frac{1}{6}}, \quad (202)$$

$$\kappa_{\parallel} \sim \rho_o^{-3} \sim \nu^{*-1}, \quad (203)$$

$$t \sim \rho_o^{-\frac{1}{2}} \sim \nu^{*-\frac{1}{6}}. \quad (204)$$

It should be pointed out that all parameters vary only slightly as collisionality is changed, except for the parallel thermal conductivity κ_{\parallel} , which varies linearly with ν^* . Also, η decreases with decreasing ν^* , so that the role of resistivity in the collisionality scan is negative, in the sense that with lower ν^* , resistivity diminishes, and the corresponding effect on growth rates (see Fig.42b) might lead to smaller ELMs, which is opposite to what experimental results predict. This justifies the need to focus efforts on resistivity, whose effect should be diminished as much as possible. In fact, as seen from Fig.42b, the lower the resistivity, the lower effect on growth rates, so that one may expect that at low resistivity, the effect on growth rates may not affect the collisionality scan too much.

The first of a collisionality scan was done with a resistivity varying between 10^{-7} and $5 \cdot 10^{-8}$, which is a factor 10 from the Spitzer value. The scan was done for the mode numbers $n = 12$, $n = 16$ and $n = 20$ separately. The ELM size is calculated by integrating pressure inside the separatrix, and the pedestal energy is calculated by multiplying the value of pressure at the top of the pedestal (before the crash) with the plasma volume inside the separatrix. The growth rates for each mode number, as well as the ELM size relative to pedestal energy, are plotted as a function of collisionality in Fig.56a. As may be observed, the ELM size decreases with decreasing collisionality, which is the opposite of what experiments predict. The fact that growth rates are decreasing with decreasing ν^* suggests that resistivity is still too high. In fact, although the lowest resistivity was only a factor 10 from the Spitzer value, this collisionality scan will be referred to as the *resistive regime*.

Based on this first attempt, it was clear that resistivity needed to be taken still lower. However, as was stated previously, at 10^{-8} , the mode $n = 12$ becomes stable. Hence, the pressure gradient was slightly increased, by a factor 1.5, in order to increase the linear instability of the ballooning modes. For this new scan, resistivity is varied between 10^{-8} and $5 \cdot 10^{-9}$,

which is the real Spitzer value (note that $5 \cdot 10^{-9}$ is the normalized η value). Also, the scan was performed for the mode numbers $n = 8$, $n = 12$ and $n = 16$, because numerical difficulties arose for the mode $n = 20$, due to the thin current structures at such a low resistivity. The resulting ELM size and growth rates of the scan are shown in Fig.56b. It can be seen that resistivity does not dominate the scan by its effect on growth rates, at least at low resistivity. The ELM size is now seen to increase with decreasing collisionality, as predicted by experimental results. Hence, this new scan may be referred to as the *ideal regime*.

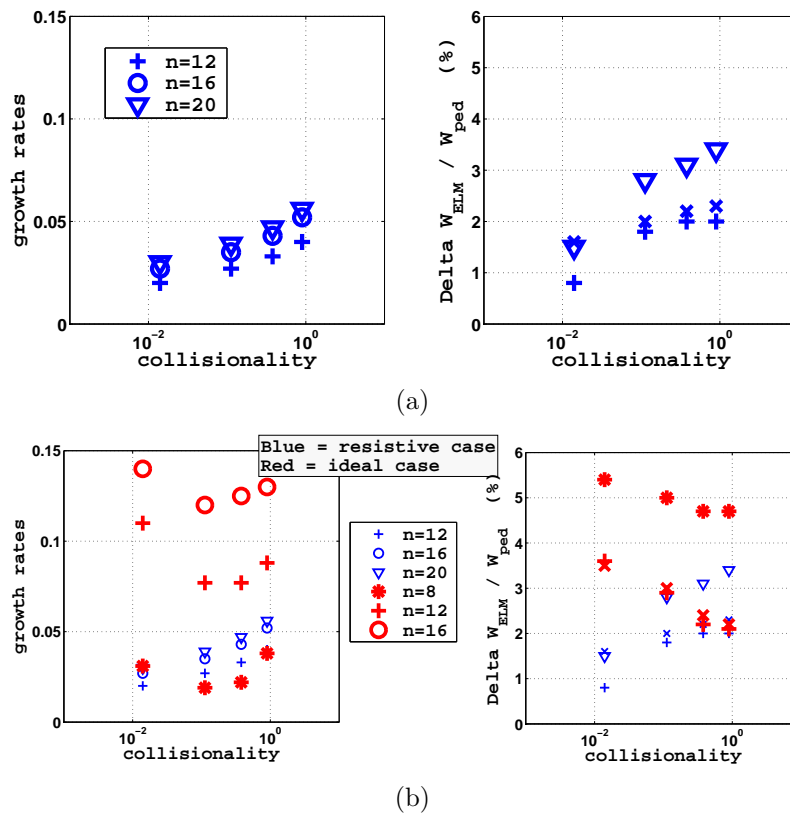


Figure 56: a). The growth rates (left) and the ELM size relative to pedestal energy $\Delta W_{ELM}/W_{ped}$ (right), plotted as a function of collisionality. This first scan was done with resistivity a factor 10 from the Spitzer value. The effect of resistivity on growth rates, as collisionality is changed, shows that this is still a resistive regime. b). In the most extreme cases, all the energy evacuated by the ballooning mode arrives on the outer divertor.

It turns out that not only the ELM size agrees with experimental results, but also the convective and conductive losses as collisionality is changed. In fact, since the growth rates do not change in the same way as in the resistive

regime, the parallel conductivity κ_{\parallel} now plays the leading role. As seen above, κ_{\parallel} varies linearly with the inverse of ν^* , so that at low collisionality, much more temperature is evacuated. This can clearly be seen in Fig.57, where the relative density losses (relative to pedestal density) is plotted together with the relative temperature losses. The density losses do not change so much as $n u^*$ is varied, but the temperature losses do. This is in good agreement with experimental results [Loarte-PPCF-2003,Beurskens-PPCF-2009] that show that the ELMs are more conductive at low collisionality.

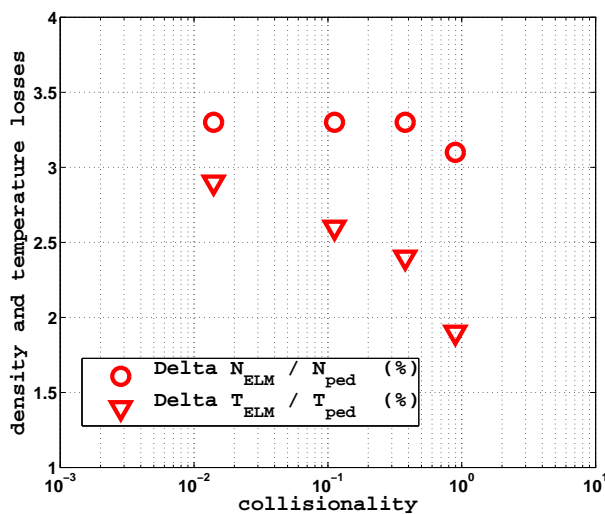


Figure 57: The relative density and temperature losses $\Delta\rho_{ELM}/\rho_{ped}$ and $\Delta T_{ELM}/T_{ped}$, as a function of collisionality. The density losses do not change with varying ν^* , unlike temperature losses: the ELMs are more conductive at low collisionality.

Also, it could be argued that this result was forced by increasing the pedestal pressure gradient. In fact, if the ideal MHD stability of the pedestal pressure gradient dominates over the effect of resistivity, then such a result should be expected, since growth rates will not change with varying ν^* , so that the dominating parameter becomes κ_{\parallel} , which evacuates more temperature at low collisionality. However, it should be verified, in future, whether a scan with the initial pedestal pressure gradient (from HRTS), but with all parameters (not just η) taken at the experimental (or theoretical) values, could reproduce the dependency of the ELM size on ν^* in agreement with experiments. In particular, since all parameters (apart from resistivity) have a damping effect on growth rates, it could be that in experimental plasma conditions, growth rates would be much higher, and thus the effect of resistivity could be expected to be negligible compared to the amplitude of the

growth rates.

The last aspect of the scan concerns the time-scales of the ELMs, as seen from the divertor heat fluxes. Fig.58 shows the heat flux on the outer divertor as a function of time, for the collisionalities $\nu^* = 0.01$, $\nu^* = 0.1$ and $\nu^* = 0.9$, with the mode $n = 8$, which produced the biggest crashes. The time is the real one (not the normalized one) and it has been shifted so that $t = 0$ corresponds to the beginning of the ELM. It is clearly seen that the ELM crash is more *compact* at lower collisionality, with a higher heat flux amplitude and a shorter duration. In addition, the ELM-affected area does not seem to change, which means that the maximum local heat flux on the divertor during an ELM really increases with decreasing collisionality.

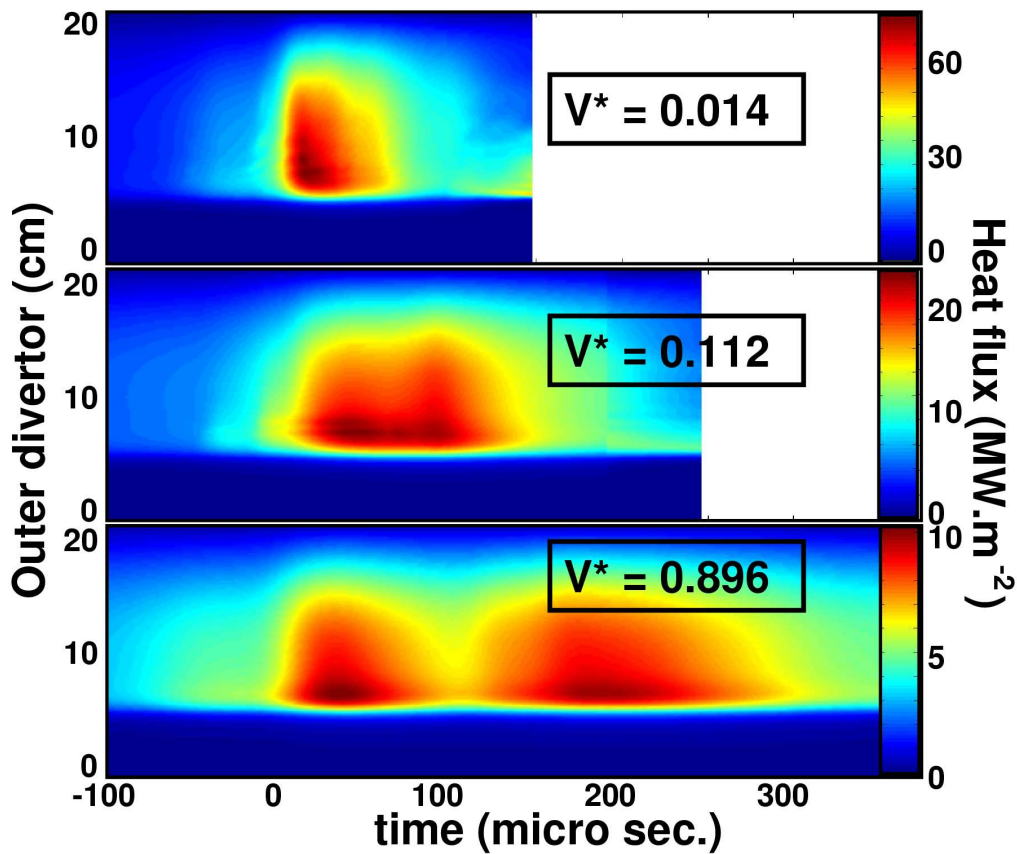


Figure 58: The heat flux on the outer divertor target as a function of time, for the collisionalities 0.014, 0.112 and 0.896, with the ballooning mode $n = 8$. The lower the collisionality, the shorter time-duration of the ELM, and the higher the heat-flux amplitude.

4.4 MAST Simulations

4.4.1 Reconstruction of the MAST Equilibrium

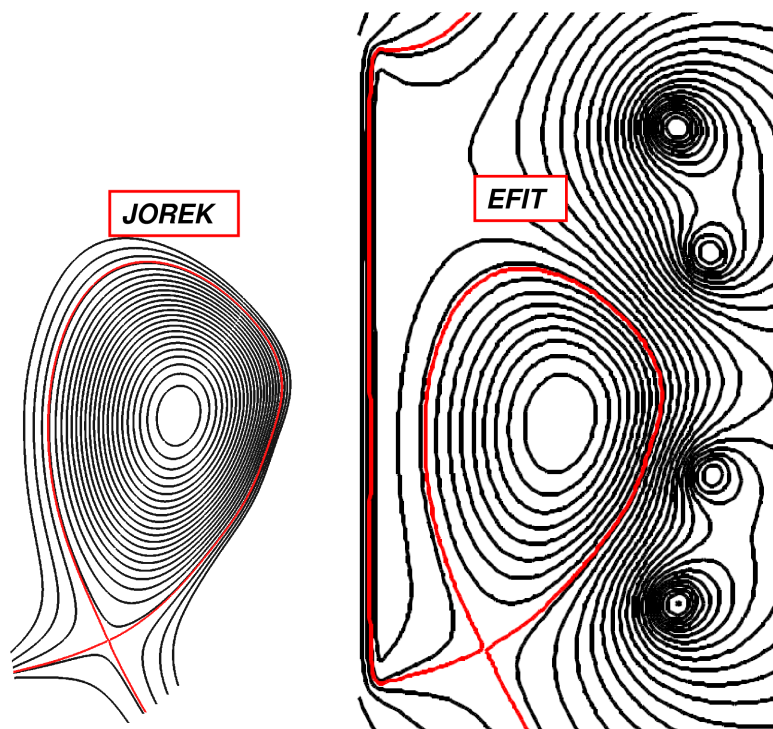
Choosing the right pulse for MAST was not so trivial, since the usual operational magnetic configuration of this spherical tokamak has two X-points, and JOREK is not yet conceived to produce simulations with more than one X-point. Since upgrading the code to run with double-null configurations would take a significant amount of work, and because the main, short term goal was to produce simulations of JET, it has been chosen to reproduce the single-null configuration of MAST. This magnetic configuration is also commonly used in the spherical tokamak and H-mode, as well as type-I ELMs, are regularly obtained with this configuration. Hence, pulse #21294 has been chosen, with pre-ELM Thomson Scattering profiles at 361ms. The electron density and temperature at the magnetic axis are respectively $3.7 \times 10^{19} \text{m}^{-3}$ and 0.85keV. It should also be pointed out that the advanced study done with JET simulations was not yet reproduced with the MAST plasma. Such a study should be carried out in future, but for now only the basic aspects of the simulations are presented, as an insight how multi-machine simulations can bring further understanding of ELMs physics.

The reconstruction of the equilibrium was done with the same method as for JET, with a pressure profile derived from the n_e and T_e Thomson Scattering profiles, the global current from EFIT with additional bootstrap calculated from HELENA, and a flux boundary taken from EFIT. Fig.59 shows the reconstruction of the equilibrium and the comparison with the EFIT equilibrium. It should be noted that due to the small aspect ratio of the tokamak, the flux gradient $\nabla\psi$ is much stronger on the LFS of the SOL. Hence, since a flux surface is needed for the SOL boundary in JOREK, the resulting SOL is very thin, because flux surfaces far from the plasma on the LFS do not go around the plasma, as can be seen from the EFIT equilibrium. This was indeed a disappointing surprise, since one the main goals in producing MAST simulations was to compare the results with the fast camera images, in order to observe how filaments behave in the SOL. Even though filaments are still ejected from the plasma in simulations, those are stopped by the boundary, so that they cannot travel as far in the SOL as in experiments.

4.4.2 Simulations of ELMs in MAST

Finding the right mode numbers for MAST simulations was the first task. Since the aspect ratio of MAST is much smaller than non-spherical tokamaks ($R/a \sim 1.1$ for MAST, compared to 3.1 for JET), the $1/R$ dependency of

Figure 59: *The MAST equilibrium reconstructed with JOREK (left), and the comparison with the EFIT equilibrium reconstruction (right).*



the toroidal magnetic field has much more importance. Thus, in MAST, the toroidal magnetic field is very strong on the HFS, and much weaker on the LFS, so that the field lines near the separatrix wind around many times when passing on the inner side of the torus (closest to the central solenoid), while they do not on the outer side of the torus (far from the central solenoid). This has a consequent impact on the dominant ballooning mode numbers during ELMs, so that in order to obtain a filamentation of the plasma which is consistent with experimental observations, one needs to consider relatively high mode numbers ($n = 20$ and above). This differs from usual (non-spherical plasmas) simulations, where the dominant mode numbers during ELMs are much lower (from $n = 6$ to $n = 16$). Fig.60 shows a comparison of a MAST simulation of $n = 20$ with the fast camera diagnostic. Unfortunately, since simulations are not able to provide a view of filaments traveling in the far SOL, this comparison is restricted to the crossing of the separatrix.

The MAST simulations find their main interest when compared to JET

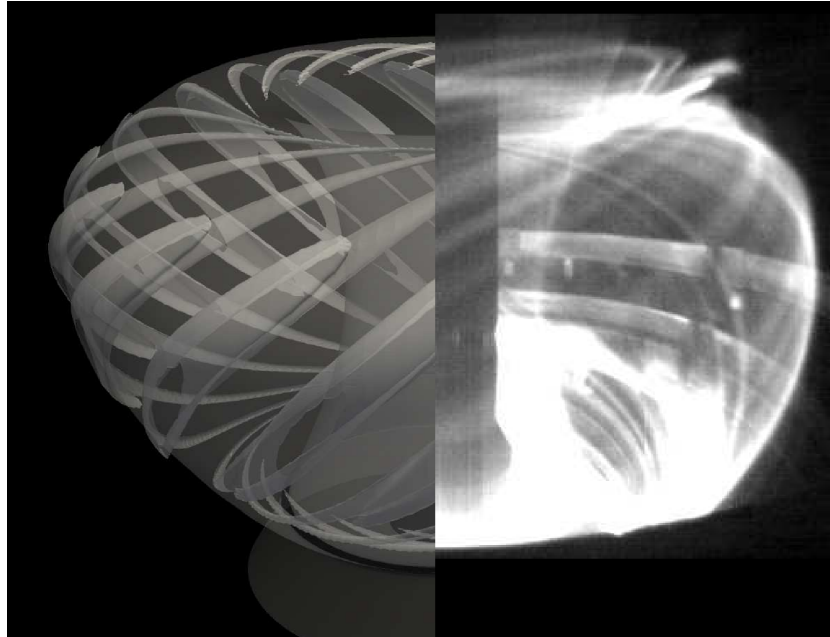


Figure 60: *Comparison of the filamentation of the plasma during an ELM. The left half features the simulation results, and the right half features a picture from the fast camera.*

simulations. Because the mode numbers of the dominant ballooning modes are different between the two machines, for the same mode number $n = 20$, the poloidal size of the filaments is equivalent in MAST and JET. This is illustrated in Fi.61 for the density. In addition, the composition of the filaments is very different. In fact, much more current is observed in the MAST filaments. As seen previously, in order to observe a consequent amount of current traveling with the filaments in JET simulations, one needs to bring the resistivity at quite a low value (at least $\eta \sim 10^{-7}$), whereas in MAST simulations, even with a high resistivity, a strong current is observed in the filaments. Furthermore, in opposition to JET simulations, the current is in phase with the density filament. It is not yet clear whether this is due to the specific magnetic configuration of MAST. Nevertheless, such a strong currents had not been observed in previous simulations of plasmas with higher aspect ratios, so that this aspect of MAST simulations particularly stood out.

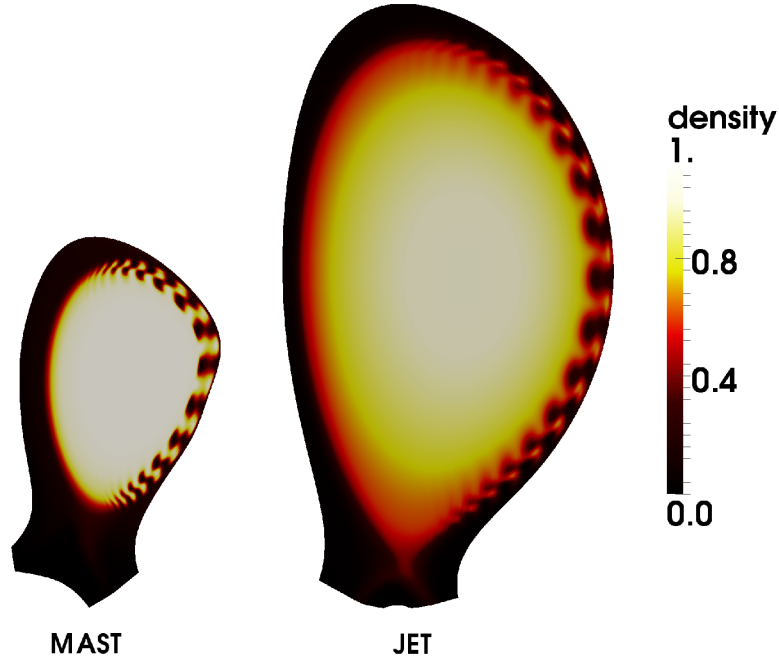


Figure 61: *The comparison of simulations of MAST and JET. For the same mode number $n = 20$, the filament size is the same in MAST and JET, even though the MAST plasma is smaller.*

4.4.3 Improving MAST Simulations

These few characteristics of ELMs simulations for MAST clearly show that multi-machine simulations could bring a further understanding of ELMs physics, or at least bring up more questions. In sight of producing more accurate comparisons between MAST and JET, some significant efforts will be needed in order to improve simulations. In particular, simulations of MAST loose a great interest if the SOL is so thin. In JET, the SOL is rather small (experimentally), in fact smaller than in simulations. Concerning filaments, this is no problem. In particular, filaments in JET simulations never reach very far out into the SOL, they cross the separatrix and remain close to it for a long time. In MAST however, it is well observed experimentally [Kirk] that the filaments have a rather constant speed and that they travel very far into the SOL. Producing simulations of MAST without being able to study this particular aspect is not very satisfying. The modifications needed in JOEUK are considerably serious, because they would require a redefinition of the grid with a new, non-flux-aligned SOL boundary. This project should

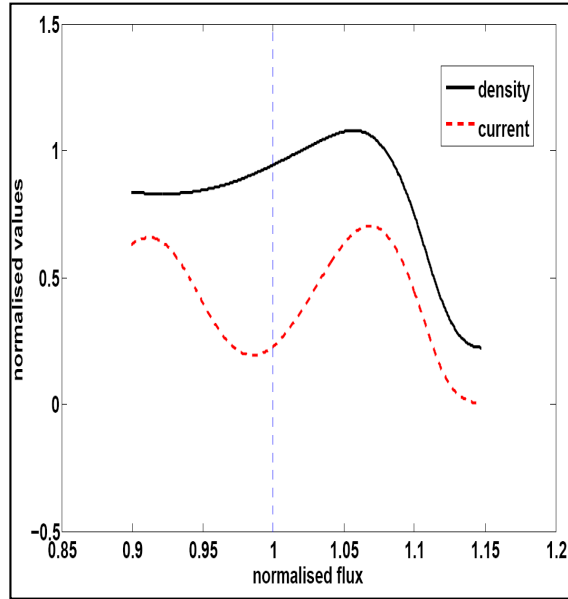


Figure 62: A large current is observed to travel in phase with the filaments during simulations of MAST. This distinguishes from JET simulations, where less current is observed in the filament, and where the current is in phase with the pressure gradient of the filament, not with its maximum pressure.

of course be combined with the implementation of a double X-point in the code. This is a large project, but it could perfectly fit a PhD student.

4.5 Conclusion

Simulations of ELMs in JET have been presented. The reconstruction of the equilibrium using HRTS profiles together with EFIT data and the HELENA code was obtained. The geometry of JET was well reproduced. The stability of the resulting plasma equilibrium is tested with HELENA for ideal MHD ballooning modes. Scans in resistivity and viscosity have shown that non-ideal (diffusive) plasma parameters may have a strong influence on the linear stability of the modes. In addition, the study carried out in Chapter 3, concerning the effect of the poloidal flow on the linear stability of ballooning modes, was carried out for the JET equilibrium. It turned out that the poloidal equilibrium flow in JET simulations have a strong stabilizing effect on ballooning modes, especially for high mode numbers.

The first aspect of ELMs simulations of JET presented in this chapter concerned the filamentation of the plasma into the SOL. The radial size of

filaments was observed to be tightly related to the pressure gradient width. Also, it was seen that resistivity has a strong effect on the dynamics of filaments, due to its influence on the growth rates of ballooning modes. Thus, if growth rates are too low, the filaments cannot manage to cross the separatrix and are destroyed by the poloidal equilibrium flow. Again, the poloidal flow is found to play a major role in simulations. In fact, when looking at the speed of filaments, it appeared that their radial speed was always about a few km/s, but that a significant poloidal velocity was often observed, both clockwise and anti-clockwise. To end the study of filaments, their composition is analyzed, exhibiting the fact that electron temperature was rapidly evacuated from the filaments by parallel conduction, and that most of the energy that would come to the first vessel wall would be due to ions. Also, the current inside the filaments is always observed to be localized at the pressure gradient of the filament, due to the $\mathbf{J} \times \mathbf{B} = \nabla p$ equilibrium.

The second aspect of simulations was that of the divertor heat fluxes. A reasonable agreement was obtained with the Infra-Red camera, both for the striped structure of heat fluxes and their dynamics. The heat flux stripes are observed to move radially on the outer divertor target, away from the strike point. It was shown that this dynamics was caused by the poloidal (toroidal) rotation of the filaments, so that a clockwise rotation of filaments in the poloidal plane results in heat flux stripes moving inward on the divertor, closer to the strike point. It should be expected that the toroidal rotation induced by the NBI injection on JET could be the cause of the dynamics of heat flux stripes on the divertor. This should be verified in near future, by implementing a toroidal momentum source in the model. Again, this aspect of simulations brings back to the same conclusion: the poloidal flow really plays a major role in ELMs physics.

The last characteristic of ELMs simulations for JET was the qualitative validation of JOREK by showing that the ELM size increases with decreasing collisionality, as is observed experimentally. In fact, two distinct MHD regimes were identified: a resistive regime and an ideal MHD regime. In the resistive regime, the collisionality scan is dominated by the effect of resistivity on the growth rates of ballooning modes, so that the ELM size decreases with decreasing collisionality. Although this is not coherent with experimental observations for type-I ELMs, such behaviour could be consistent with type-III ELMs, although this should be verified more thoroughly in future. In the more ideal regime, the stability of ballooning modes is dominated by the pressure gradient, not by the resistivity, so that the collisionality scan is governed by the parallel thermal conductivity, which increases linearly with decreasing ν^* , so that more temperature is evacuated at low collisionality. This conductive/convective aspect of the scan is also in agreement with sim-

ulations. However, the size of the ELMs in this scan is still much smaller than in experiments, which is probably due to the fact that other diffusive plasma parameters (μ , D_{\perp} and so on) have a damping effect on the growth rates of ballooning modes. Before being able to bring these parameters to near-experimental values, as was done for resistivity, still more grid resolution is needed. There is good hope that such results could be accomplished in the coming years, and that a robust, quantitative validation of JOREK could be obtained against multi-machine experimental data. Once this validation is performed, coherent extrapolations to ITER will be possible.

Finally, an insight to this multi-machine validation was given with simulations of ELMs in MAST. Since the main goal of the thesis was to obtain good agreement between simulations of JET and experiments, the MAST simulations were not pushed as hard as for JET, but some basic aspects of simulations have shown that the specific geometry and magnetic configuration of spherical tokamaks have a strong influence on ELMs. However, simulations of MAST were restricted by the numerical construction of JOREK, which is not adapted to such specific configurations. In particular, JOREK cannot simulate double X-point plasmas, and the way the SOL boundary is obtained results in a very thin SOL, which restricts comparisons of simulations with experiments, since MAST has a large SOL, where filaments are observed to travel with significant speed. Improving JOREK to produce more successful simulations of MAST would require a significant amount of work, which is yet not planned for near future, since the validation of JOREK against JET data comes first. But in terms of physical understanding of ELMs, such a project would surely produce very interesting results.

ACKNOWLEDGEMENTS This work, as part of the project ANR-CIS.2006.001, has benefited from financial support from the French 'Agence Nationale de la Recherche'. It is supported by the European Communities under the contract of Association between EURATOM and CEA, and was carried out within the framework of the European Fusion Development Agreement. The views and opinions expressed herein do not necessarily reflect those of the European Commission.

REFERENCES

1. ITER Physics Expert Groups on Confinement and Transport and Confinement Modelling and Database, ITER Physics Basis Editors and ITER EDA, *Nucl. Fusion* **39** 2175 (1999)
2. J.P. Freidberg: *Ideal Magnetohydrodynamics*, *Plenum Press* (1987)
3. S.I. Braginskii, Transport Processes in a Plasma, *Review of Plasma Physics*, Vol. 1, pp 205-311 (1965)
4. W. Horton, Drift Waves and Transport, *Rev. Mod. Phys.* **71** 735-778 (1999)
5. C. Nguyen, *Phys. Plasmas* **15** 112502 (2008)
6. D. Biskamp, Magnetic Reconnection in Plasmas, *Cambridge Monographs on Plasma Physics* **3** (2000)
7. J. Wesson, Tokamaks, 3rd ed., *Oxford Univ. Press* (2004)
8. H.R. Strauss, *Phys. Fluids* **19** 134 (1976)
9. H.R. Strauss, *J. Plasma Physics*, Vol. 57, part 1, pp 83-87 (1997)
10. H. Grad and H. Rubin, Hydromagnetic equilibria and force-free magnetic fields, *Proc. 2nd Intern. Conf. on Peaceful Uses of Atomic Energy*, Vol. 31, U.N., Geneva, Switzerland (1958)
11. V.D. Shafranov, *Sov. Phys.*, JETP26, 682 (1960)
12. O. Sauter, *Phys. Plasmas* **6** (1999)
13. H.P. Furth, J. Killeen, M.N. Rosenbluth, B. Coppi, *Plasma Phys. and Nucl. Fusion Research*, Vol. 1, IAEA, Vienna, p.103 (1965)
14. F. Wagner et al., *Phys. Rev. Lett.* **49** 1408 (1982)
15. P.H. Diamond et al., *Phys. Rev. Lett.* **72** (1994)
16. J. Kim et al., *Phys. Rev. Lett.* **72** (1994)
17. K.C. Shaing et al., *Plasma Phys. Control. Fusion* **36** (1994)
18. F.L. Hinton et al., *Phys. Plasmas* **2** (1995)
19. K.H. Burrell et al., *Plasma Phys. Control. Fusion* **38** (1996)
20. W. Suttrop, *Plasma Phys. Contr. Fusion* **42** A1-A14 (2000)
21. H. Zohm, *Plasma Phys. Contr. Fusion* **38** 105-128 (1996)
22. S. Devaux, *36th EPS Conf. on Plasma Phys.*, Sofia, 2009, ECA Vol. 33E, p-2.157 (2009)
23. T.E. Evans et al., *Nucl. Fusion* **48** 024002 (2008)
24. Y. Liang et al., *Plasma Phys. Contr. Fusion* **49** B581 (2007)
25. M. Becoulet et al., *Nucl. Fusion* **48** 024003 (2008)
26. P.T. Lang et al., *Nucl. Fusion* **47** 8, pp754-761 (2007)
27. L.R. Baylor et al. *Nucl. Fusion* **49** 085013 (2009)
28. S.P. Gerhardt et al., *Nucl. Fusion* **50** 064015 (2010)
29. F. Sartori et al., *35th EPS Conf. on Plasma Phys.*, Hersonissos, Crete, Greece (2008)
30. M. Podesta et al., *Rev. Sci. Inst.*, Vol. 79, #10 (2008)
31. M.N.A. Beurskens, *Nucl. Fusion* **49** 125006 (2009)
32. F. Poli, *Nucl. Fusion* **50** 025004 (2010)
33. A; Kirk et al., *Plasma Phys. Contr. Fusion* **49** 1259-1275 (2007)
34. C.R. Negus et al., *Rev. Sci. Inst.* **77** 10F102 (2006)
35. Y. Andrew et al., *Rev. Sci. Inst.* **77** 10E913 (2006)
36. J.W. Connor, P. Hastie, R. Taylor, *Proc. Roy. Soc. London* A365, 1 (1979)
37. P.C. Stangeby, The Plasma Boundary of Magnetic Fusion Devices, *Taylor and Francis Group* (2002)
38. P. Andrew et al., *J. Nucl. Mater.* 337-339 (2005)

39. T.C. Hender, *Nucl. Fusion* **47** 5128-5202 (2007)
40. R.J. Groebner *et al.*, *Phys. Rev. Lett.* **64** (1990)
41. K. Ida *et al.*, *Phys. Rev. Lett.* **65** (1990)
42. P. Gohil *et al.*, *Nucl. Fusion* **34** (1994)
43. K. Crombé *et al.*, *Phys. Rev. Lett.* **95** (2005)
44. Y. Andrew *et al.*, *EPL* **83** (2008)
45. E. Marmor *et al.*, *Nucl. Fusion* **49** (2009)
46. H.R. Strauss, *Phys. Plasmas* **2** (1995)
47. A.Y. Aydemir *et al.*, *Phys. Plasmas* **14** (2007)
48. A.Y. Aydemir *et al.*, *Nucl. Fusion* **49** (2009)
49. H.P. Zehrfeld *et al.*, *European Phys. Society* (2000)
50. E. Hameiri, *Phys. Fluids* **1** **26** (1983)
51. L. Guazzotto and R. Paccagnella, *Plasma Phys. Control. Fusion* **51** (2009)
52. L. Guazzotto and R. Betti, *Phys. Plasmas* **12** (2005)
53. H.R. Strauss, *J. Plasma Physics* **57** (1997)
54. P.C. Stangeby, *The Plasma Boundary of Magnetic Fusion Devices*.
55. S.D. Scott *et al.*, *Phys. Rev. Lett.* **64** (1990)
56. B. Grek *et al.*, *European Phys. Soc., Petit Lancy, Switzerland* **1**, (1987)
57. W.A. Cooper *et al.*, *Plasma Phys. Control. Fusion* **30** (1988)
58. J.W. Connor *et al.*, *Phys. Rev. Lett.* **40** (1978)
59. A. Bhattacharjee *et al.*, *Phys. Fluids B* **1** (1989)
60. X.-H. Wang and A. Bhattacharjee, *Phys. Fluids B* **2** (1990)
61. E. Hameiri and S.T. Chun, *Phys. Rev. A* **41** (1990)
62. K. Grassie and N. Krech, *Phys. Fluids B* **2** (1990)
63. F. Waelbroeck and L. Chen, *Phys. Fluids B* **3** (1991)
64. E. Hameiri *et al.*, *Phys. Plasmas* **1** (1994)
65. R.L. Miller and R. Waltz, *Phys. Plasmas* **1** (1994)
66. R.L. Miller *et al.*, *Phys. Plasmas* **2** (1995)
67. L.-J. Zheng and M. Tessarotto, *Phys. Plasmas* **4** (1997)
68. M. Furukawa *et al.*, *Nucl. Fusion* **43** (2003)
69. M. Furukawa *et al.*, *Plasma Phys. Control. Fusion* **46** (2004)
70. M. Furukawa *et al.*, *Nucl. Fusion* **45** (2005)
71. P. Snyder *et al.*, *Nucl. Fusion* **47** (2007)
72. S. Saarelma *et al.*, *Plasma Phys. Control. Fusion* **49** (2007)
73. A.J. Webster *et al.*, *Phys. Plasmas* **11** (2004)
74. J.W. Connor *et al.*, *Phys. Plasmas* **14** (2007)
75. A.Y. Pankin *et al.*, *Plasma Phys. Control. Fusion* **49** (2007)
76. N. Aiba *et al.*, *Nucl. Fusion* **49** (2009)
77. M. Becoulet *et al.*, *Nucl. Fusion* **49** (2009)
78. L. Garcia *et al.*, *Phys. Plasmas* **6** (1999)
79. S. Saarelma *et al.*, *Plasma Phys. Control. Fusion* **51** (2009)
80. G.T.A. Huysmans and O. Czarny, *Nucl. Fusion* **47** (2007)
81. G.T.A. Huysmans *et al.*, *Plasma Phys. Control. Fusion* **51** (2009)
82. P. Beyer *et al.*, *Phys. Rev. Lett.* **94** (2005)
83. G. Fuhr-Chaudier, P. Beyer, S. Benkadda, X. Garbet *et al.*, *Phys. Rev. Lett.* **101** (2008)

4.6 Appendix A

Reduction of the Maxwell Equations

At first, using the assumption above that the toroidal magnetic field is constant, one may express the total magnetic field as

$$\begin{aligned}
 \mathbf{B} &= \mathbf{B}_\phi + \mathbf{B}_p \\
 &= B_\phi \mathbf{e}_\phi + \frac{1}{R} \nabla \psi \times \mathbf{e}_\phi \\
 &= \frac{F_0}{R} \mathbf{e}_\phi + \frac{1}{R} \nabla \psi \times \mathbf{e}_\phi \\
 &= F_0 \nabla \phi + \nabla \psi \times \nabla \phi.
 \end{aligned} \tag{205}$$

Note that this assumption implies that equation (121) is automatically satisfied, and that one may rewrite equations (119) and (120) as

$$\nabla \times \mathbf{E} = -\frac{\partial \mathbf{B}_p}{\partial t}, \tag{206}$$

$$\nabla \times \mathbf{B}_p = \mu_0 \mathbf{J}, \tag{207}$$

Concerning Ohm's law (118), resistivity has to be taken into account, but first the current needs to be properly defined. Developing equation (207), one obtains

$$\begin{aligned}
 \mathbf{J} &= \frac{1}{\mu_0} \nabla \times (\nabla \psi \times \nabla \phi) \\
 &= \frac{1}{\mu_0} \left[-\nabla \phi (\Delta^* \psi) + \frac{1}{R^2} \nabla_\perp \left(\frac{\partial \psi}{\partial \phi} \right) \right],
 \end{aligned} \tag{208}$$

where the Grad-Shafranov operator has been defined in Chapter 2.2. Now, the approximation that the toroidal magnetic field dominates the perpendicular field may be interpreted in the sense that parallel length scales dominate perpendicular length scales, so that $\mathbf{e}_\phi \cdot \nabla \psi \ll \|\nabla_\perp \psi\|$. In other words, the total current may be assumed to be mainly toroidal, with

$$\begin{aligned}
 \mathbf{J} &= -j \nabla \phi, \\
 j &= \frac{1}{\mu_0} \Delta^* \psi.
 \end{aligned} \tag{209}$$

With this new definition of the current \mathbf{J} , resistivity may be introduced into Ohm's law (118) as follows,

$$\mathbf{E} + \mathbf{v} \times \mathbf{B} = \eta \mathbf{J}, \tag{210}$$

Now, one may write the perpendicular magnetic field as $\mathbf{B}_p = \nabla \psi \times \nabla \phi = \nabla \times (\psi \nabla \phi)$. Substituting into equation (206), one obtains that $\nabla \times [\partial_t (\psi \nabla \phi) + \mathbf{E}] = 0$. Hence, the expression inside brackets may be expressed as the gradient of a scalar potential u , defined as the electric potential, so that $\partial_t (\psi \nabla \phi) = -\mathbf{E} - F_0 \nabla u$. Note that the F_0 coefficient has been added to simplify the final formulation of \mathbf{v}_\perp . Substituting for equation (210), one obtains

$$\frac{\partial (\psi \nabla \phi)}{\partial t} = \mathbf{v} \times \mathbf{B} + \eta j \nabla \phi - F_0 \nabla u. \tag{211}$$

Next, one separates the parallel and perpendicular velocities as $\mathbf{v} = \mathbf{v}_\perp + \mathbf{v}_\parallel$ with the parallel velocity $\mathbf{v}_\parallel = v_\parallel \mathbf{B}$. Substituting into equation (211), one obtains that

$$\frac{\partial(\psi \nabla \phi)}{\partial t} = \mathbf{v}_\perp \times \mathbf{B} + \eta j \nabla \phi - F_0 \nabla u. \quad (212)$$

Now, taking the curl of this last equation with $\nabla \phi$ gives $\nabla \phi \times (\mathbf{v}_\perp \times \mathbf{B}) = F_0 \nabla \phi \times \nabla u$, which can be developed to obtain $\frac{F_0}{R^2} \mathbf{v}_\perp - (\nabla \phi \cdot \mathbf{v}_\perp) \mathbf{B} = F_0 \nabla \phi \times \nabla u$. Again, the approximation that parallel length scales dominate perpendicular length scales implies that $\mathbf{e}_\phi \cdot \mathbf{v}_\perp \ll \|\mathbf{v}_\perp\|$. Hence, the perpendicular velocity may be approximated to $\mathbf{v}_\perp = R^2 \nabla \phi \times \nabla u$. This gives the definition of the plasma velocity,

$$\mathbf{v} = \mathbf{v}_\perp + \mathbf{v}_\parallel, \quad (213)$$

$$\mathbf{v}_\perp = R^2 \nabla \phi \times \nabla u, \quad (214)$$

$$\mathbf{v}_\parallel = v_\parallel \mathbf{B}. \quad (215)$$

Finally, taking the dot product of equation (212) with $\nabla \phi$ gives

$$\begin{aligned} \frac{1}{R^2} \frac{\partial \psi}{\partial t} &= F_0 \nabla \phi \cdot (\mathbf{v}_\perp \times \nabla \phi) + \nabla \phi \cdot [\mathbf{v}_\perp \times (\nabla \psi \times \nabla \phi)] + \frac{1}{R^2} \eta j - F_0 \nabla \phi \cdot \nabla u \\ &= \nabla \phi \cdot (\mathbf{v}_\perp \times \nabla \psi) - (\mathbf{v}_\perp \cdot \nabla \psi) \nabla \phi + \frac{1}{R^2} \eta j - F_0 \nabla \phi \cdot \nabla u \\ &= -(\nabla \phi \times \nabla u) \cdot \nabla \psi - F_0 \nabla \phi \cdot \nabla u \\ &= \frac{1}{R} [\psi, u] + \frac{1}{R^2} \eta j - F_0 \frac{1}{R^2} \frac{\partial u}{\partial \phi}, \end{aligned} \quad (216)$$

where the Poisson brackets are defined by $[A, B] = \mathbf{e}_\phi \cdot (\nabla A \times \nabla B)$. Hence, one obtains the reduction of Maxwell's equations,

$$\frac{\partial \psi}{\partial t} = R [\psi, u] + \eta (j - j_A) - F_0 \frac{\partial u}{\partial \phi}, \quad (217)$$

$$\mathbf{B} = F_0 \nabla \phi + \nabla \psi \times \nabla \phi, \quad (218)$$

$$\mathbf{v} = R^2 \nabla \phi \times \nabla u + v_\parallel \mathbf{B}, \quad (219)$$

$$\mathbf{J} = -j \nabla \phi = -\frac{1}{\mu_0} \Delta^* \psi \nabla \phi, \quad (220)$$

where j_A represents the applied current.

Reduction of the Energy Equation

One may also reduce the energy equation to a single fluid temperature equation. First, notice that the continuity equation (115) may be rewritten as

$$\frac{d\rho}{dt} = -\rho \nabla \cdot \mathbf{v} + S_\rho, \quad (221)$$

where the convective derivative is given by $d/dt = \partial/\partial t + \mathbf{v} \cdot \nabla$, and S_ρ represents the particle source. Also, a particular definition of pressure is used, which differs from the usual definition $p = nT$, where n is the number of plasma particles, and T the plasma temperature. Instead, we adopt the definition

$$p = \rho T. \quad (222)$$

Thus, the energy equation may be written as

$$\begin{aligned}
&\Rightarrow \frac{d}{dt} \left(\frac{T}{\rho^{\gamma-1}} \right) = 0, \\
&\Rightarrow \frac{1}{\rho^{\gamma-1}} \frac{dT}{dt} - (\gamma-1) \frac{T}{\rho^\gamma} \frac{d\rho}{dt} = 0, \\
&\Rightarrow \frac{dT}{dt} + (\gamma-1)T \nabla \cdot \mathbf{v} - (\gamma-1)pS_\rho = 0.
\end{aligned} \tag{223}$$

Hence, adding the parallel and perpendicular conductivities and heating, one obtains the temperature equation

$$\rho \frac{\partial T}{\partial t} = -\rho \mathbf{v} \cdot \nabla T - (\gamma-1)p \nabla \cdot \mathbf{v} + \nabla \cdot (\kappa_{\parallel} \nabla_{\parallel} T + \kappa_{\perp} \nabla_{\perp} T) + S_T + (\gamma-1)\rho p S_\rho = 0. \tag{224}$$

Note that the source term coming from the continuity equation can be ignored, unless strong density sources are involved (eg. pellets). This source term can also be introduced into the momentum equation as follows.

Reduction of the Momentum Equation to the Vorticity Equation

Before considering the momentum equation, it should be recalled that equation (116) is not the original momentum equation, since it has already been reduced using the continuity equation. The original momentum equation reads

$$\begin{aligned}
&\Rightarrow \frac{\partial}{\partial t} (\rho \mathbf{v}) + \nabla \cdot (\rho \mathbf{v} \mathbf{v}) = \mathbf{J} \times \mathbf{B} - \nabla p, \\
&\Rightarrow \rho \frac{\partial \mathbf{v}}{\partial t} + \mathbf{v} \left[\frac{\partial \rho}{\partial t} + \nabla \cdot (\rho \mathbf{v}) \right] + \rho \mathbf{v} \cdot \nabla \mathbf{v} = \mathbf{J} \times \mathbf{B} - \nabla p, \\
&\Rightarrow \rho \frac{\partial \mathbf{v}}{\partial t} + \mathbf{v} S_\rho + \rho \mathbf{v} \cdot \nabla \mathbf{v} = \mathbf{J} \times \mathbf{B} - \nabla p,
\end{aligned} \tag{225}$$

The toroidal vorticity W is defined as

$$\begin{aligned}
\mathbf{w} &= \nabla \times \mathbf{v}_{\perp}, \\
W &= \nabla \phi \cdot \mathbf{w} = \nabla_{\perp}^2 u.
\end{aligned} \tag{226}$$

Thus, in order to obtain an equation for the toroidal vorticity, one applies the operator $\nabla \phi \cdot \nabla \times (R^2 \dots)$ to the momentum equation (225). Note that the factor R^2 stands for a specific reason, which is to simplify the final formulation of the term $\mathbf{J} \times \mathbf{B}$. Proceeding term by term, and using the notation $\hat{\rho} = R^2 \rho$, we have

$$\begin{aligned}
\nabla \phi \cdot \nabla \left(R^2 \rho \frac{\partial \mathbf{v}}{\partial t} \right) &= \nabla \phi \cdot \nabla \left(\hat{\rho} R^2 \nabla \phi \times \nabla \left(\frac{\partial u}{\partial t} \right) \right) \\
&= \nabla \cdot (\hat{\rho} R^2 [\nabla \phi \times \nabla u_t] \times \nabla \phi) \\
&= \nabla \cdot \{ \hat{\rho} R^2 [(\nabla \phi \cdot \nabla \phi) \nabla u_t - (\nabla \phi \cdot \nabla u_t) \nabla \phi] \} \\
&= \nabla \cdot [\hat{\rho} (\nabla u_t - \nabla_{\parallel} u_t)] \\
&= \nabla \cdot (\hat{\rho} \nabla_{\perp} u_t).
\end{aligned}$$

The convection term (which is the most complex one) gives

$$\begin{aligned}
\nabla\phi \cdot \nabla \times [R^2 \rho (\mathbf{v} \cdot \nabla) \mathbf{v}] &= \nabla\phi \cdot \nabla \times [\hat{\rho} (\mathbf{v} \cdot \nabla) \mathbf{v}] \\
&= \nabla\phi \cdot [\nabla\hat{\rho} \times (\mathbf{v} \cdot \nabla \mathbf{v}) + \hat{\rho} \nabla \times (\mathbf{v} \cdot \nabla \mathbf{v})] \\
&= \nabla\phi \cdot \left[\frac{1}{2} \nabla\hat{\rho} \times \nabla \mathbf{v}^2 - \nabla\hat{\rho} \times [\mathbf{v} \times (\nabla \times \mathbf{v})] \right] \\
&\quad + \nabla\phi \cdot \left[\frac{1}{2} \hat{\rho} \nabla \times \nabla \mathbf{v}^2 - \hat{\rho} \nabla \times [\mathbf{v} \times (\nabla \times \mathbf{v})] \right] \\
&= \frac{1}{2R} [\hat{\rho}, \mathbf{v}^2] + \nabla\phi \cdot [\nabla\hat{\rho} \times (\mathbf{w} \times \mathbf{v})] \\
&\quad + \hat{\rho} \nabla\phi \cdot \nabla \times (\mathbf{w} \times \mathbf{v}) \\
&= \frac{1}{2R} [\hat{\rho}, R^4 |\nabla_{\perp} u|^2] + \nabla\hat{\rho} \cdot [(\mathbf{w} \times \mathbf{v}) \times \nabla\phi] \\
&\quad + \hat{\rho} \nabla \cdot [(\mathbf{w} \times \mathbf{v}) \times \nabla\phi] \\
&= \frac{1}{2R} [\hat{\rho}, R^4 |\nabla_{\perp} u|^2] + \nabla\hat{\rho} \cdot [(\nabla\phi \cdot \mathbf{w}) \mathbf{v} - \cancel{(\nabla\phi \cdot \mathbf{v}) \mathbf{w}}] \\
&\quad + \hat{\rho} \nabla \cdot [(\nabla\phi \cdot \mathbf{w}) \mathbf{v} - \cancel{(\nabla\phi \cdot \mathbf{v}) \mathbf{w}}] \\
&= \frac{1}{2R} [\hat{\rho}, R^4 |\nabla_{\perp} u|^2] + R^2 \nabla\hat{\rho} \cdot (W \nabla\phi \times \nabla u) \\
&\quad + \hat{\rho} \nabla \cdot (WR^2 \nabla\phi \times \nabla u) \\
&= \frac{1}{2R} [\hat{\rho}, R^4 |\nabla_{\perp} u|^2] + WR^2 \nabla\phi \cdot (\nabla u \times \nabla\hat{\rho}) \\
&\quad - \hat{\rho} \nabla\phi \cdot \nabla \times (WR^2 \nabla u) \\
&= \frac{1}{2R} [\hat{\rho}, R^4 |\nabla_{\perp} u|^2] - \frac{1}{R} WR^2 [\hat{\rho}, u] \\
&\quad - \hat{\rho} \nabla\phi \cdot [\nabla (WR^2) \times \nabla u + WR^2 \cancel{\nabla \times \nabla u}] \\
&= \frac{1}{2R} [\hat{\rho}, R^4 |\nabla_{\perp} u|^2] - \frac{1}{R} WR^2 [\hat{\rho}, u] - \frac{1}{R} \hat{\rho} [WR^2, u] \\
&= \frac{1}{2R} [\hat{\rho}, R^4 |\nabla_{\perp} u|^2] - \frac{1}{R} [\hat{\rho} WR^2, u].
\end{aligned}$$

The pressure term, less complex,

$$\begin{aligned}
\nabla\phi \cdot \nabla \times [R^2 \nabla p] &= \nabla\phi \cdot \nabla \times [R^2 \nabla p] \\
&= \nabla\phi \cdot [\nabla (R^2) \times \nabla p + R^2 \cancel{\nabla \times \nabla p}] \\
&= \frac{1}{R} [R^2, p].
\end{aligned}$$

The current term,

$$\begin{aligned}
\nabla\phi \cdot \nabla \times [R^2 \mathbf{J} \times \mathbf{B}] &= \nabla \cdot [R^2 (\mathbf{J} \times \mathbf{B} \times \nabla\phi)] \\
&= \nabla \cdot \{R^2 [(\mathbf{J} \cdot \nabla\phi) \mathbf{B} - (\mathbf{B} \cdot \nabla\phi) \mathbf{J}]\} \\
&= \nabla \cdot [-j \mathbf{B} - R^2 (\mathbf{B} \cdot \nabla\phi) \mathbf{J}] \\
&= \nabla \cdot [-j \mathbf{B} - F_0 \mathbf{J}] \\
&= -\mathbf{B} \cdot \nabla j - j \nabla \cdot \mathbf{B} - F_0 \nabla \cdot \mathbf{J} \\
&= -F_0 \nabla j \cdot \nabla\phi - \nabla j \cdot (\nabla\psi \times \nabla\phi) \\
&= -\frac{F_0}{R^2} \frac{\partial j}{\partial \phi} + \nabla\phi \cdot (\nabla\psi \times \nabla j) \\
&= \frac{1}{R} [\psi, j] - \frac{F_0}{R^2} \frac{\partial j}{\partial \phi}.
\end{aligned}$$

And the continuity source term

$$\begin{aligned}
\nabla\phi \cdot \nabla \times (R^2 \mathbf{v} S_\rho) &= S_\rho \nabla \cdot (R^2 \mathbf{v} \times \nabla\phi) \\
&= S_\rho \nabla \cdot [R^4 (\nabla\phi \times \nabla u) \times \nabla\phi] \\
&= S_\rho \nabla \cdot (R^2 \nabla_\perp u).
\end{aligned} \tag{227}$$

Thus, adding up and introducing viscosity, one obtains

$$\begin{aligned}
R \nabla \cdot \left[R^2 \rho \nabla_\perp \left(\frac{\partial u}{\partial t} \right) \right] &= [R^4 \rho W, u] - \frac{1}{2} [R^2 \rho, R^4 |\nabla_\perp u|^2] \\
&\quad - [R^2, p] + [\psi, j] - \frac{F_0}{R} \frac{\partial j}{\partial \phi} + \mu R \nabla^2 W,
\end{aligned} \tag{228}$$

where the source term coming from induction is ignored, since the current thesis does not involve any pellet injection or any other kind of strong, localized density sources.

Reduction of the Momentum Equation to the Parallel Velocity Equation

Similarly, one obtains the parallel momentum equation by taking the dot product of equation (225) with \mathbf{B} . The result is

$$\begin{aligned}
\frac{\rho F_0}{R^2} \frac{dv_\parallel}{dt} &= \mathbf{B} \cdot \nabla p, \\
\Rightarrow \rho F_0^2 \frac{dv_\parallel}{dt} &= F_0 \frac{\partial p}{\partial \phi} - R [\psi, p],
\end{aligned} \tag{229}$$

where it has been assumed that $B^2 \approx (F_0/R)^2$, and the source term from continuity has been ignored. Introducing parallel viscosity, one obtains

$$\rho F_0^2 \frac{dv_\parallel}{dt} = F_0 \frac{\partial p}{\partial \phi} - R [\psi, p] + \mu_\parallel \nabla^2 v_\parallel. \tag{230}$$